Vortex-induced vibrations of a pivoted circular cylinder and their control using a tuned-mass damper

by

Sina Kheirkhah

A thesis
presented to the University of Waterloo
in fulfillment of the
thesis requirement for the degree of
Master of Applied Science
in
Mechanical Engineering

Waterloo, Ontario, Canada, 2011

Author's declaration

I hereby declare that I am the sole author of this thesis. This is a true copy of the thesis, including any required final revisions, as accepted by my examiners.

I understand that my thesis may be made electronically available to the public.

Abstract

Vortex-induced vibrations of a pivoted circular cylinder and control of these vibrations were investigated experimentally. A novel experimental setup was employed to reproduce orbiting response observed in some engineering applications. An adaptive pendulum tuned-mass damper (TMD) was integrated with the cylindrical structure in order to control the vortex-induced vibrations. All experiments were performed at a constant Reynolds number of 2100 for a range of reduced velocities from 3.4 to 11.3 and damping ratios from 0.004 to 0.018. For the experiments involving TMD, the TMD mass ratio was 0.087 and the TMD damping ratios investigated were 0 and 0.24.

The results of the experiments performed without the TMD show that, in the synchronization region, the frequencies of transverse and streamwise vibrations lock onto the natural frequency of the structure. The cylinder is observed to trace elliptic trajectories. A mathematical model is introduced to investigate the mechanism responsible for the occurrence of the observed elliptic trajectories and figure-8 type trajectories reported in previous laboratory investigations. The results show that the occurrence of either elliptic trajectories or figure-8 type trajectories is governed primarily by structural coupling between vibrations in streamwise and transverse directions. Four types of elliptic trajectories were identified. The results show that the occurrence of the different types of elliptic trajectories is linked to phase angle between the streamwise and transverse vibrations of the structure, which depends on structural coupling.

The results of the experiments performed to investigate effectiveness of the TMD in controlling vortex-induced vibrations show that tuning the TMD natural frequency to the natural frequency of the structure decreases significantly the amplitudes of transverse and streamwise vibrations of the structure. Specifically, the transverse amplitudes of vibrations are decreased by a factor of ten and streamwise amplitudes of vibrations are decreased by a factor of three. The results show that, depending on the value of the TMD damping ratio, the frequency of transverse vibrations is either characterized by the natural frequency or by two frequencies: one higher and the other lower than the natural frequency of the structure, referred to as fundamental frequencies. Independent of TMD damping and tuning frequency ratios, the frequency of streamwise vibrations matches that of the transverse vibrations in the synchronization region, and the cylinder traces elliptic trajectories. The phase angle between the streamwise and transverse vibrations is nearly constant when the pendulum is restrained. However, with the TMD engaged and tuned to the natural frequency, the phase angle fluctuates significantly with time. A mathematical model was utilized to gain insight into the frequency response of the structure. The results of the modeling show that the frequency of transverse vibrations is characterized by the fundamental frequency or frequencies of the structure and the frequency of streamwise vibrations is characterized by the fundamental frequency or frequencies as well as the first harmonic of the fundamental frequency or frequencies of the structure.

Acknowledgements

First, I would like to express my deepest sense of gratitude to my supervisor, Professor Serhiy Yarusevych. I believe his great level of knowledge and insightful sense of criticism have gifted me a style of research from which I will benefit for the rest of my career. I am thankful to both Serhiy and Angela, his wife, for welcoming myself with open arms during research group gatherings at their place.

I would like to thank my co-supervisor, Professor Sriram Narasimhan, for his invaluable insights and encouragements during the completion of the project.

I am thankful to student shop advisers, Kwai Chan and John Potzold, for their assistance in development of my experimental setup.

I want to thank my fellow graduate student, Richard Lourenco, for his efforts in developing the tuned-mass damper setup.

I am thankful to my fellow graduate student, Chris Morton. Specifically, I want to thank him for sharing his experience in performing flow visualization experiments.

Special thanks go to my fellow graduate students, Ryan Gerakopulos and Mike Bishop. Thank you for all the good moments we had together.

I want to thank my dear friend, Mike Boutilier. His generosity in sharing codes, equations, and fruitful discussions is gratefully acknowledged.

I would like to thank my dear friends and home-mates, Reza and Mohammad, who made my stay in Waterloo more enjoyable.

Finally, I am grateful to the University of Waterloo, Natural Sciences and Engineering Research Council of Canada (NSERC), Ontario Centers of Excellence (OCE), Greater Toronto Airports Authority (GTAA), and Rowan Williams Davies and Irwin (RWDI) for support and funding this work.

Dedication

To my parents,

Without their continued encouragements and support this never would have been possible.

Table of Contents

List of Figures

List of Tables

Nomenclature

$a_1 - a_4$	non-dimensional coefficients in Eqs. 4.5 and 4.6, defined in Table 4.2
a^*, b^*	non-dimensional forcing coefficients in Eqs. E.1 and E.2
A, B	non-dimensional coefficients in Eqs. 4.5 and 4.6, defined in Table 4.2
AR	cylinder aspect ratio, L/D
A_x	streamwise amplitudes of vibrations
A_x^*	normalized streamwise amplitude of vibrations, A_x / D
A_y	transverse amplitude of vibrations, [m]
A_y^*	normalized transverse amplitude of vibrations, A_y / D
b	distance between the spring and the pivot point, [m]
Bi	bias error
C	damping coefficient, introduced in Eqs. 3.1 and 3.2, [N.s/m]
C_A	added mass coefficient
C_D	amplitude of drag coefficient fluctuations of a two DOF circular cylinder
C_L	amplitude of lift coefficient fluctuations of a two DOF circular cylinder
$C_x(z)$	local amplitude of drag coefficient fluctuations of a two DOF pivoted circular cylinder
$C_y(z)$	local amplitude of lift coefficient fluctuations of a two DOF pivoted circular cylinder
dB	decibel, $10 \times \log_{10}$
D	cylinder diameter, [m]
f_1	frequency of vibrations of a structure equipped with TMD [Hz], $f_1 < f_n$
f_2	frequency of vibrations of a structure equipped with TMD [Hz], $f_2 > f_n$

f_1^*	normalized frequency f_1, f_1/f_n
f_2^*	normalized frequency f_2, f_2/f_n
f_a	in-air natural frequency of the structure, [Hz]
f_c	coupling frequency, [Hz]
f_{com}	common frequency or lock-in frequency
f_e	frequency of excitation, [Hz]
$f_{e.x}$	frequency of excitation in the streamwise direction, [Hz]
$f_{e,y}$	frequency of excitation in the transverse direction, [Hz]
f_e^*	normalized frequency of excitation, f_e/f_n
$f_{e,x}^*$	normalized frequency of excitation in the streamwise direction, $f_{e,x}/f_n$
$f_{e,y}^*$	normalized frequency of excitation in the transverse direction, $f_{e,y}/f_n$
f_n	in-still-water natural frequency of the structure, [Hz]
f_r	non-dimensional coefficient in Eqs. 4.3 and 4.4, $(f_a/f_n)I^*/(I^*+C_A)$
$f_{r,TMD}$	non-dimensional coefficient in Eqs. 5.8 and 5.9, $(f_a/f_n)[(I+mL_p^2)\big/(I+mL_p^2+I_A)]$
f_r^*	normalized TMD natural frequency, f_{TMD}/f_n
f_{TMD}	TMD natural frequency, [Hz]
f_x	frequency of streamwise vibrations, [Hz]
f_x^*	normalized frequency of streamwise vibrations, f_x/f_n
f_y	frequency of transverse vibrations, [Hz]
f_y^*	normalized frequency of transverse vibrations, f_y/f_n

f_s	vortex shedding frequency of a stationary circular cylinder, [Hz]
F_x	fluid force per unit length of the cylinder in the streamwise direction, [N/m]
F_y	fluid force per unit length of the cylinder in the transverse direction, [N/m]
Fr	Froude number, $U/\sqrt{gL}$
g	acceleration due to gravity, [m/s^2]
$h(t)$	function utilized to obtain phase angle of a single, introduced in Eq. 3.2
$H(x)$	the Hilbert transform of x
I	moment of inertia of structure about the pivot point, [kg.m^2]
I_A	added moment of inertia, [kg.m^2]
I_d	moment of inertia of the displaced fluid about the pivot point, [kg.m^2]
I_s	non-dimensional coefficients in Eqs. 5.11 and 5.12
I^*	moment of inertia ratio, I/I_d
I_s^*	non-dimensional coefficient in Eqs. 5.8 and 5.9, $(mL_p l_p)\big/[(I+mL_p^2+I_A)]$
$I^*\zeta$	moment of inertia-damping parameter
K	stiffness of the spring, [N/m]
K_e	effective stiffness of the spring, [N/m]
K_c	cross-stiffness, [N/m]
l_p	pendulum length, [m]
l^*	non-dimensional coefficient in Eqs. 5.10 and 5.11, $l^* = L_p/l_p$
L	length of the cylinder, [m]
L_0	wetted length of the cylinder, [m]

L_P	distance between the pivot point and location of the tuning platform, [m]
m	mass of the structure, [kg]
m_d	mass of displaced fluid, [kg]
m^*	mass ratio, m / m_d
$m^*\zeta$	mass-damping parameter
M_x	fluid moment in the streamwise direction, [N.m]
M_y	fluid moment in the transverse direction, [N.m]
N	number of data points (Eq. B.2)
N_x, N_y, N_z	reaction forces in the streamwise, transverse and spanwise directions
n	number of data points utilized in FFT technique (Eq. B.3)
o_1	cylinder pivot point
o_2	pendulum supporting point
PSD	normalized power spectrum density, [dB]
r	non-dimensional variable in Eq. D.3, $x / D - y / D$
r_1, r_2	non-dimensional coefficients in Eqs. E.9 and E.10
R_x	ratio of the amplitudes of streamwise vibrations associated with f_n and $2f_n$
R_y	ratio of the amplitudes of transverse vibrations associated with f_n and $2f_n$
Re	Reynolds number, UD / ν
s	dummy variable in Eq. 3.1
S	precision error
t	time, [s]
t_s	Student's multiplier

t^*	normalized time for in-air vibrations, $t \times f_a$
t_m^*	normalized time at which maximum amplitude of free vibrations in the x direction occurs
t^{**}	normalized time for in-still water vibrations, $t \times f_n$
U	free-stream velocity, [m/s]
U_r	non-dimensional coefficient in Eqs. 4.3 and 4.4, $(U^* / U_c^*)^2 I^* /(I^* + C_A)$
$U_{r,TMD}$	non-dimensional coefficient in Eqs. 5.8 and 5.9, $U_{r,TMD} = (U^* / U_c^*)^2 / [1 + I_A /(I + mL_p^2)]$
U^*	reduced velocity, $U / f_n D$
U_c^*	coupling-frequency based reduced velocity, $U / f_c D$
V_0	sensors voltage output, [v]
x, y, z	streamwise, transverse, and spanwise directions, respectively
x_h, x_p	homogenous and particular solutions for x (Appendix D), [m]
x_M	displacement of the main mass in Eqs. 2.3 and 2.4, [m]
x_{ss}	steady state cylinder tip displacement in the streamwise direction (Appendix E), [m]
x_{TMD}	displacement of the TMD mass in Eqs. 2.3 and 2.4, [m]
y_0	initial transverse displacement of the cylinder tip in the free vibrations tests, [m]
y_h, y_p	homogenous and particular solutions for y (Appendix D), [m]
y_{ss}	steady state cylinder tip displacement in the transverse direction (Appendix E), [m]

Greek symbols

β	non-dimensional coefficient in Eq. D.4, $\sqrt{1 - (f_c / f_a)^2 - \zeta^2}$
β_r	non-dimensional coefficient in Eq. E.6, $\sqrt{1 - U_r - \zeta^2 f_r^2}$

γ	angular displacement of the pendulum in the transverse direction, [rad]
δ	maximum deflection angle of the structure, [rad]
Δ^*	non-dimensional coefficient in Eq. 5.24, $2U^{*2}C_DD\big/[\pi(I^*+C_A)L_0\sqrt{(1-\Lambda)^2+(\Lambda)^2}]$
ϕ	angular displacement of the structure in the transverse direction, [rad]
ε	angular displacement of the structure in the streamwise direction, [rad]
ζ	damping ratio of the structure
ζ_{TMD}	TMD damping ratio
η	non-dimensional coefficient in Eqs. D.6 and D.7, $\sqrt{1+(f_c/f_a)^2-\zeta^2}$
θ	phase angle between the transverse and streamwise vibrations of the structure, [rad]
$\kappa_1-\kappa_4$	non-dimensional coefficients in Eq. E.13
λ^*	normalized wave length, $U/(f_yD)$
Λ	weighting factor
μ	TMD mass ratio
ν	kinematic viscosity of water, [m^2/s]
ρ	water density, [kg/m^3]
$\sigma_1-\sigma_4$	non-dimensional coefficients in Eq. E.9
χ	angular displacement of the pendulum in the streamwise direction, [rad]
ψ	phase angle between the fluid forcing in the streamwise and transverse directions, [rad]
ω_n	angular natural frequency of the structure, $2\pi f_n$ [rad/s]

1 Introduction

Vortex shedding from flexible cylindrical structures placed in uniform flow can excite the structures to undergo vibrations if the vortex shedding frequency is close to the natural frequency of the structure, e.g., Parkinson (1971) and Skop & Griffin (1973). Such vortex-induced vibrations (VIV) commonly occur in many engineering applications, e.g., offshore and civil engineering structures. Amplitudes of VIV can reach several cylinder diameters, which may impede system operation and, in extreme cases may lead to system failure, e.g., Dailey et al. (1987) and Huse et al. (1998). In the past several decades, laboratory studies have been performed to explore VIV of cylindrical structures, see, for example, review papers by Bearman (1984) and Williamson & Govardhan (2004). Also, a number of methods have been proposed to mitigate VIV, e.g., Kareem (1983).

Most of the previous studies of VIV were performed on cylinders free to vibrate in either transverse direction to the flow, e.g., Feng (1968) or both transverse as well as streamwise directions, e.g., Blevins & Coughran (2009). In most of the previous studies in which models were free to vibrate in both directions, experimental setups were designed to produce uniform amplitudes of vibrations along the cylinder span, e.g., Jauvtis & Williamson (2004) and Sanchis et al. (2008). However, in order to create a more realistic physical model of VIV of circular cylinders, a few studies have been conducted to investigate VIV of pivoted rigid circular cylinders, in which the transverse and streamwise amplitudes of vibrations vary linearly along the cylinder span, e.g., Flemming & Williamson (2005) and Leong & Wei (2008). These studies indicate that cylinders undergoing VIV trace figure-8 type trajectories. Although this finding agrees with field observations in many engineering applications, field measurements of VIV in civil structures, e.g., Ishizaki (1967) and Gamble (2009), and offshore structures, e.g., Vandiver et al. (2005), indicate that cylindrical structures may also trace elliptic trajectories. The occurrence of elliptic response in VIV of cylindrical structures is yet to be investigated in laboratory settings.

Several investigations have been performed to devise efficient methods for mitigating vortex-induced vibrations. These methods can be classified into two categories: (i) fluid dynamics methods, which are based on disrupting the vortex shedding process (Zdravkovich, 1981), and (ii) structural methods, which are based on modifying the dynamics of structures by adding vibration absorbers (Kareem et al., 1999). Implementation of helical strakes, perforated shrouds, surface bumps, and splitter plates are examples of fluid dynamics methods widely used for mitigating vortex-induced vibrations. The tuned-liquid damper (TLD) and tuned-mass damper (TMD) are examples of structural methods used to mitigate vortex-induced vibrations. TMD is a mass attached to a structure via a spring and a damper. The mechanical energy of the structure is dissipated by the damper. TMDs have been widely used for vibration absorption in different applications, e.g., in automotive, aircraft, and ship engines. Over the past few decades, these devices have been implemented to control VIV of tall buildings, e.g., Kareem et al. (1999). A limited number of laboratory investigations, e.g., Xu et al. (1992) and Tanaka & Mak (1983), have been performed to study the effectiveness of one degree-of-freedom (DOF) TMDs for the mitigation of VIV of one DOF structures. Although these studies provide invaluable insight into the effectiveness of TMDs, to the best of author's knowledge, no experimental study has been performed to investigate the effect of tuned-mass dampers on VIV of two DOF structures.

The present study is motivated by the need for uncovering the mechanism that causes the occurrence of elliptic response of two DOF cylindrical structures, and the need for the mitigation of VIV of two DOF structures. The main objectives of the study are as follows:

(i) Recreate elliptic response of cylindrical structures in laboratory environment.

(ii) Investigate the mechanism behind the elliptic response of two DOF cylindrical structures.

(iii) Evaluate the effectiveness of a novel adaptive pendulum TMD in mitigating VIV of a two DOF structure.

The thesis is divided into seven chapters including this introduction. Chapter 2 provides a review of previous studies concerned with vortex-induced vibrations of circular cylinders, as well as methods for the mitigation of these vibrations. In Chapter 3, the experimental setup employed in the present investigation is characterized using experimental measurements and a mathematical model. The results of the investigations are presented in Chapters 4 and 5. In Chapter 4, VIV of the cylinder are analyzed. In Chapter 5, first, a mathematical model is used to provide a baseline for the response of one DOF structures equipped with one DOF TMDs. Then, experimental results illustrating the effect of a two DOF TMD on two DOF VIV are presented. Finally, Chapters 6 and 7 contain main conclusions and recommendations, respectively.

2 Literature review

2.1 Flow over a stationary circular cylinder

Numerous studies have been performed to investigate flow over a stationary circular cylinder, see, for example, reviews by Roshko (1954), Berger & Wille (1972), Lin & Pao (1979), Bearman (1984), Oertel (1990), Williamson (1996), and Choi et al. (2008). Different flow regimes were identified based on the Reynolds number (Re) (Williamson, 1996). For Re ≈ 50, a global instability in the wake of the cylinder leads to periodic shedding of vortices known as vortex shedding phenomenon (Provansal et a1., 1987). For $50 \lesssim \text{Re} \lesssim 200$, the vortex shedding in the wake of the cylinder is laminar and the associated regime is called laminar vortex shedding regime (Williamson, 1996). For $200 \lesssim \text{Re} \lesssim 400$, transition to turbulence occurs in the wake of the cylinder, and this flow regime is related to as wake transition regime (Zdravkovich, 1997). For $400 \lesssim \text{Re} \lesssim 200{,}000$, transition to turbulence occurs in the separated shear layers developing on both sides of the cylinder. This regime is known as shear layer transition regime (Norberg, 1994). For $\text{Re} \gtrsim 200{,}000$, transition to turbulence occurs in the boundary layers developing on both sides of the cylinder (Zdravkovich, 1997). The present study is concerned with the shear layer transition regime, which is common to many industrial applications (Williamson, 1996).

2.2 One DOF uniform amplitude VIV

Due to periodic nature of the vortices shed from cylindrical structures, the fluid forces exerted on the structures have an oscillatory nature (Bishop & Hassan, 1963) and may cause vortex-induced vibrations. Vortex-induced vibrations occur mainly in the direction transverse to the flow (Skop & Griffin, 1975). Thus, early laboratory studies of VIV of circular cylinders have been performed primarily on the cylindrical structures with one degree of freedom (DOF) transverse to the flow (e.g., Feng, 1968;

Bearman, 1984; Khalak & Williamson, 1999). These studies were focused on the structural response as well as its relation to the vortex shedding patterns.

2.2.1 Amplitude response and vortex shedding patterns

The amplitude of response is commonly defined as half the peak-to-peak amplitude of steady state vibrations of the structure. Following the dimensional analysis discussed by Sarpkaya (2004), it can be shown that, for one DOF structures, the normalized amplitude of response depends primarily on the following four dimensionless parameters:

(i) Reduced velocity ($U^* = U/f_nD$, where U is the free-stream velocity, f_n is the natural frequency of the structure, and D is the cylinder diameter).

(ii) Mass ratio ($m^* = m/m_d$, where m is the mass of the structure and m_d is the mass of the displaced fluid).

(iii) Damping ratio (ζ, ratio of the damping coefficient of the structure to the critical damping coefficient). Damping ratio can be estimated using free vibration tests.

(iv) Reynolds number ($Re = UD/\upsilon$, where υ is the kinematic viscosity)

Feng (1968) studied the effect of reduced velocity on the normalized amplitude of vibrations for a high mass ratio ($m^* = 320$) and high mass-damping parameter ($m^*\zeta \sim 1$) cylinder. A plot that shows the variation of the normalized transverse amplitude of vibrations with reduced velocity is classically referred to as amplitude response plot. Feng's amplitude response plot is shown in Fig. 2.1 (diamonds). His results show that significant amplitudes of vibrations occur for $5 < U^* < 8$. The plot features two distinct branches, namely, initial and lower branches, with a hysteretic transition between the branches. Khalak & Williamson (1999) investigated the effect of U^* on the normalized amplitude of vibrations for relatively low ($m^* = 2.4$) and moderate mass ratios ($m^* = 10.3$ and 20.6) cylinders with low mass-damping parameter ($m^*\zeta \sim 0.01$). Their results are reproduced in Fig 2.1 for three mass ratios. The results of

Khalak & Williamson (1999) show that the range of reduced velocities for which significant amplitudes of vibrations occur narrows with increasing the mass ratio. Specifically, increasing the mass ratio from 2.4 to 10.3, and 20.6, decreases the range of reduced velocities associated with significant amplitudes of vibrations from about $2.5 < U^* < 13$, to $3.5 < U^* < 12$, and $4 < U^* < 10.5$, respectively.

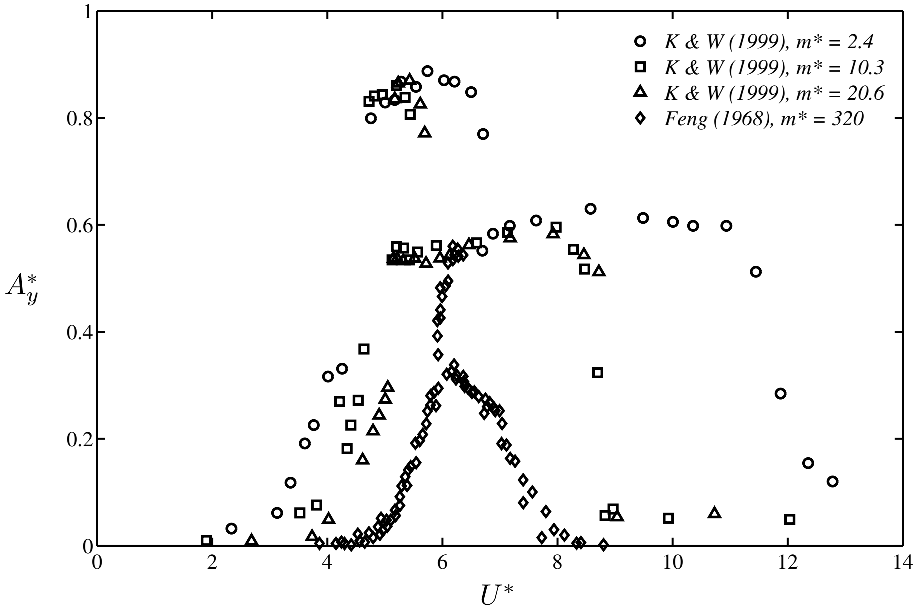

Figure 2.1 Amplitude response plot: ◊, results of Feng (1968) and ○, □, and Δ, results of Khalak & Williamson (1999).

Khalak & Williamson (1999) indicate that, in comparison with high mass ratio and high mass-damping parameter cylinders, the amplitude response plot for low and moderate mass ratios and low mass-damping parameter cylinders (Fig. 2.1) features three branches of response, namely, initial, lower, and upper branches, where the upper branch of response is associated with relatively high amplitude of vibrations ($A_y^* \sim 1$). Khalak & Williamson (1999) show that transition between the initial and upper branch is hysteretic, however, the transition between the upper and lower branches is intermittent.

Khalak & Williamson (1999) performed flow visualization to study the relation between vortex shedding patterns and the branches of response in the amplitude response plot. Their flow visualization results indicate that the transition between the initial and lower branches of response is attributed to a change in the vortex shedding pattern in the wake of the cylinder. They showed that the initial branch of response is associated with the shedding of two counter rotating vortices in the wake per cycle of cylinder vibrations, referred to as 2S vortex shedding pattern. The 2S pattern is similar to the von Karman type vortex shedding in the wake of a stationary circular cylinder. The upper branch of response is linked to the formation of two pairs of counter rotating vortices per cycle of oscillations, referred to as 2P vortex shedding pattern. The transition between the 2S and 2P patterns is associated with the transition between the initial and upper branches of response. In contrast, the transition between the upper and lower branches is not associated with a change in vortex shedding pattern. The lower branch is associated with either the 2P vortex shedding pattern or a "non-synchronized" pattern of shedding. Other possible vortex shedding patterns associated with the vortex-induced vibrations of the uniform one DOF cylinders have been investigated using controlled oscillations, e.g., Williamson & Roshko (1988), with the results compiled into a well-known Williamson-Roshko map. The updated map based on subsequent studies, Morse & Williamson (2009), is shown in updated map Fig. 2.2.

2.2.2 Frequency response

Results of Khalak & Williamson (1999) and Govardhan & Williamson (2000) show that both the mass ratio and the reduced velocity can significantly affect the frequency response. Results of Govardhan & Williamson (2000) indicate that there exists a critical mass ratio of $m^* = 0.54$ below and above which frequency response plots are distinctly different. For $m^* < 0.54$, the frequency of transverse vibrations (f_y) increases linearly with increasing the reduced velocity. For $m^* > 0.54$, two different regions in the frequency response can be identified, namely, synchronization and non-synchronized regions. For a range of reduced velocities corresponding to the synchronization region, the frequency of transverse vibrations

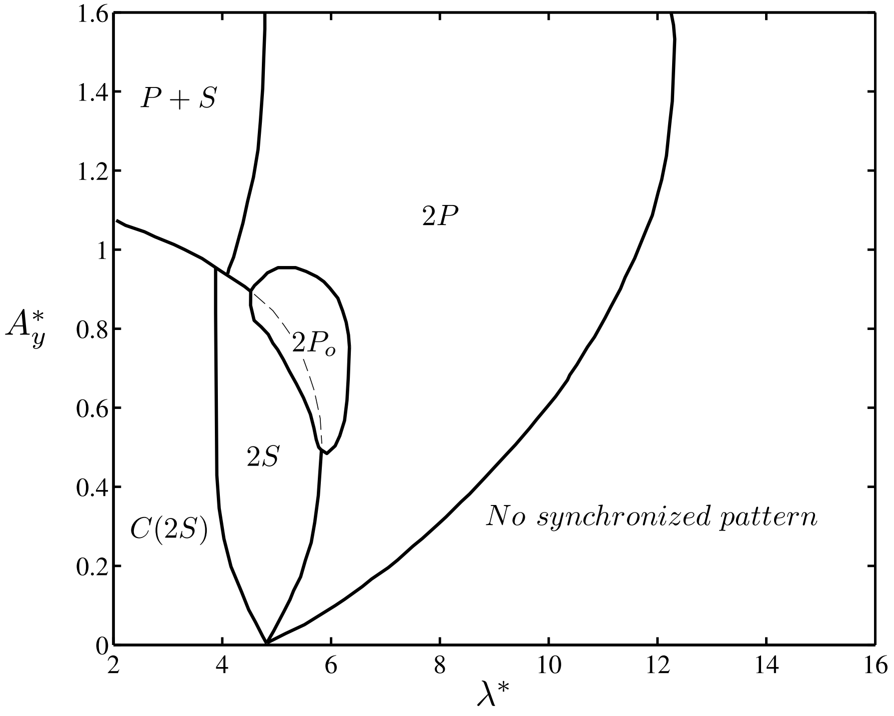

Figure 2.2 Map of vortex shedding regimes reproduced based on Morse & Williamson (2009).

locks onto a constant frequency (f_{com}) more than or equal to the cylinder model natural frequency, e.g., Govardhan & Williamson (2000) and Sarpkaya (2004). Results of Govardhan & Williamson (2000) indicate that increasing the mass ratio narrows the synchronization region. For example, for $m^* = 2.4$, 10.3, and 320, the synchronization region is within $7 < U^* < 12.5$, $5 < U^* < 9$, and $5 < U^* < 8.5$, respectively. Govardhan & Williamson (2000) proposed the following relation for f_{com},

$$f_{com} = f_n \sqrt{\frac{m^* + C_A}{m^* - 0.54}} \tag{2.1}$$

where C_A is the added mass coefficient ($C_A = 1$ for circular cylinders; Leonard & Roshko, 2001). Equation 2.1 shows that f_{com}/ f_n approaches unity with increasing the mass ratio.

Outside of the synchronization region, i.e., in the non-synchronized region, the frequency of vibrations depends on the reduced velocity (Feng, 1968; Khalak & Williamson, 1999). For reduced velocities lower than those within the synchronization region, the frequency response is characterized by f_n and the vortex shedding frequency of a stationary circular cylinder (f_s). For reduced velocities higher than those within the synchronization region, the frequency response is characterized by f_{com} and f_s.

2.3 Two DOF uniform amplitude VIV

Although one DOF freedom studies provide invaluable insight into the vortex-induced vibrations of circular cylinders, in most engineering applications, structures can respond in streamwise as well as transverse directions to the flow. Several investigations have been performed to study the effect of adding the streamwise degree of freedom on VIV of circular cylinders, e.g., Jauvtis & Williamson (2004), Blevins & Coughran (2009), Gharib (1999), Jeon & Gharib (2001), Sarpkaya (1995), and Sanchis et al. (2008). In this section, literature related to the two DOF uniform amplitude VIV of circular cylinders is reviewed.

2.3.1 Amplitude response and vortex shedding patterns

Jauvtis & Williamson (2004) investigated the effect of both mass ratio and reduced velocity on two DOF VIV of circular cylinders. Their results show that, for $m^* > 6$, the freedom of the cylinders to vibrate streamwise as well as transverse to the flow does not significantly change the transverse amplitude of vibrations. Thus, they concluded that the transverse amplitudes of response obtained for one DOF VIV can be used to estimate the transverse amplitude of response for two DOF cylinders with $m^* > 6$. A comparison of the results of Jauvtis & Williamson (2004) for $m^* = 7$ and those of Blevins & Coughran (2009) for $m^* = 17.1$ shows that, similar to one DOF studies, the range of reduced velocities associated with significant amplitudes of vibrations narrows with increasing the mass ratio. Specifically, increasing the mass ratio from 7 to 17.1 narrows the range from about $4 < U^* < 11$ to $5 < U^* < 8.5$, respectively.

For $m^* < 6$, the results of Jauvtis & Williamson (2004) and Blevins & Coughran (2009) show that the addition of the streamwise degree of freedom can significantly affect the transverse amplitude of vibrations. Their results indicate that the amplitude response plot for a two DOF cylinder contains three branches of response, namely, initial, lower, and supper-upper branches, with a hysteretic transition between the supper-upper and lower branches. The supper-upper branch is associated with relatively high transverse and streamwise amplitudes of vibrations, i.e., $A_y^* \approx 1.5$ and $A_x^* \approx 0.3$, respectively. Jauvtis & Williamson (2004) argue that the occurrence of high amplitudes of vibrations in the supper-upper branch is associated with a distinct wake vortex pattern, named 2T, where two triplets of vortices form in each cycle of oscillations of the cylinder. The vortex shedding patterns observed by Jauvtis & Williamson (2004) for the initial and lower branches of response were similar to the patterns observed for these branches for one DOF low mass-damping ratio cylinders (e.g., Khalak & Williamson, 1999), i.e., 2S for the initial branch, and 2P and non-synchronized patterns for the lower branch

2.3.2 Frequency and trajectory of response

Results of Jauvtis & Williamson (2004), Sanchis et al. (2008), and Blevins & Coughran (2009) indicate that both the reduced velocity and the mass ratio significantly affect the frequency response of two DOF cylinders. Their results show that, within the synchronization region, the frequency response of two DOF cylinders is similar to that of one DOF cylinders. However, in the non-synchronized region, the frequency response is different from that of one DOF studies. In the synchronization region, Jauvtis & Williamson (2004) proposed the following correlation for f_{com}.

$$f_{com} = f_n \sqrt{\frac{m^* + C_A}{m^* - 0.52}} \tag{2.2}$$

Similar to Eq. 2.1, Eq. 2.2 shows that f_{com}/f_n approaches unity with increasing the mass ratio. In the non-synchronized region, the results of Jauvtis & Williamson (2004) indicate that, for $m^* > 6$ and for reduced velocities higher than those within the synchronization region, the frequency response is similar to that of one DOF studies. However, for reduced velocities lower than those characterizing the synchronization region, the frequency of transverse vibrations matches f_s (cf., frequency response of one DOF cylinders for which the frequency of transverse vibrations is characterized by f_s and f_n, Khalak & Williamson, 1999). For $m^* < 6$ and reduced velocities higher than those within the synchronization region, the results of Jauvtis & Williamson (2004) show that the frequency of transverse vibrations is higher than f_{com} (cf., frequency of transverse vibrations of one DOF cylinders that locks onto both f_s and f_{com}). However, for $m^* < 6$ and reduced velocities lower than those characterizing the synchronization region, the results of Jauvtis & Wiliamson (2004) and Blevins & Coughran (2009) indicate that the frequency of transverse vibrations only is lower than f_s (cf., frequency of transverse vibrations of one DOF cylinders which is characterized by f_s and f_n).

Previous laboratory investigations of two DOF VIV of circular cylinders, e.g., Jauvtis & Williamson (2004), Blevins & Coughran (2009), Gharib (1999), Jeon & Gharib (2001), Sarpkaya (1995), and Sanchis et al. (2008), indicate that the frequency of streamwise vibrations is almost twice that of the transverse vibrations for the range of mass ratios and reduced velocities investigated; therefore, the cylinders were observed to trace figure-8 type trajectories.

2.4 One DOF linear amplitude VIV

Allowing the uniform circular cylinders to vibrate streamwise as well as transverse to the flow serves to create a more realistic model of VIV occurring in practical engineering applications. However, in most engineering applications, the amplitudes of vibrations vary along the span of the structure, e.g., Brika & Laneville (1993) and Huera-Huarte & Bearman (2009). As the first step of simulating VIVs in which amplitude varies along the cylinder span, some investigations were performed for one DOF cylinders with linear variation of amplitude along the cylinder span, e.g., experimental studies of Fujarra et al. (2001)

and Voorhees et al. (2008) as well as analytical investigations of Skop & Griffin (1975). A comparison of the results presented in Fujarra et al. (2001) and Voorhees et al. (2008) with those for one DOF uniform amplitude VIV, e.g., Govardhan & Williamson (2000) shows significant differences in the amplitude response plots at similar mass ratios and damping ratios. Specifically, the results of Fujarra et al. (2001) show that the upper branch of response is absent in the amplitude response plot, with only initial and lower branches being present. In addition, for $12 < U^* < 21$, Fujarra et al. (2001) observed that increasing the reduced velocity increases the amplitude of vibrations; whereas, in the case of uniform amplitude vibrations, Govardhan & Williamson (2000) observed that the amplitudes of vibrations decreases with increasing the reduced velocity in this range of U^*.

The frequency response plots presented in Fujarra et al. (2001) and Voorhees et al. (2008) are similar to that presented in Khalak & Williamson (1999) within the synchronization region and for reduced velocities higher than those within the synchronization region. However, for reduced velocities lower than those characterizing the synchronization region, the frequency of transverse vibrations of the one DOF cylinder with linear amplitude variation locks onto f_s (Fujarra et al., 2001); whereas, the frequency of transverse vibrations is characterized by both f_s and f_n in the case of uniform amplitude VIV (e.g., Khalak & Williamson, 1999).

2.5 TWO DOF linear amplitude VIV

Adding the streamwise degree of freedom to pivoted circular cylinders can significantly affect the response of the structure. Flemming & Williamson (2005) and Leong & Wei (2008) investigated vortex-induced vibrations of a pivoted circular cylinder free to vibrate in streamwise and transverse directions. In this section, these two studies are discussed.

2.5.1 Amplitude response and vortex shedding patterns

The results of Flemming & Williamson (2005) indicate that the mass ratio and the inertia-damping parameter ($I^{*}\zeta$) can significantly affect the amplitude response. Their results show that, similar to the case of one and two DOF uniform amplitude VIV of circular cylinders, the range of reduced velocities for which significant amplitude of transverse vibrations occur narrows with increasing mass ratio. Specifically, for $m^{*} = 1.03$, 2.68, and 7.69 tested by Flemming & Williamson (2005), the ranges were $2.6 < U^{*} < 19.6$, $3.5 < U^{*} < 14$, and $3.5 < U^{*} < 11.5$, respectively. Their results show that the amplitude response plot features initial and lower branches of response for moderate values of the inertia-damping parameter ($I^{*}\zeta \sim 0.1$). For low values of this parameter ($I^{*}\zeta \sim 0.001$), the plot features initial, lower, and upper branches of response. The results of Flemming and Williamson (2005) also show a hysteretic transition between the initial and upper and an intermittent switching between the upper and lower branches of response for low-inertia damping parameter cylinders.

The flow visualization results of Flemming & Williamson (2005) indicate that, for moderate and low values of inertia-damping parameter, vortex shedding patterns at a given spanwise location agree with those expected from Williamson-Roshko map (Fig. 2.2) based on local transverse amplitude of vibrations for initial and lower branches of response. However, for the upper branch of response, their results do not agree with the Williamson-Roshko map. Flemming and Williamson (2005) show that the upper branch of response is associated with the formation of two co-rotating vortices along the span of the cylinder, named 2C vortex shedding pattern.

Leong & Wei (2008) investigated two DOF VIV of a pivoted circular cylinder with very low mass ratio ($m^{*} = 0.45$) and moderate moment of inertia-damping parameter ($I^{*}\zeta = 0.08$). Their results show two branches of response, initial and upper branches. Leong & Wei (2008) performed flow visualization studies at mid span of their pivoted cylinder. They observed vortex shedding patterns similar to those predicted from Williamson-Roshko map based on transverse amplitude of vibrations measured at the mid span of the cylinder for $U^* < 6.2$. Specifically, they observed 2S and 2P vortex shedding patterns for $1.1 < U^* < 2.6$ and $2.6 < U^* < 6.2$, respectively. However, for $U^* > 6.2$, they observed formation of a pair of vortices and a single vortex per cycle of oscillation, known as P+S pattern; whereas the non-synchronized pattern is to be expected from the Williamson-Roshko map.

2.5.2 Frequency and trajectory of response

Flemming & Williamson (2005) investigated the effect of reduced velocity on the frequency response of a pivoted circular cylinder with $m^* = 1.03$. Their results show that, for $U^* < 8.2$, the frequency response is similar to that for two DOF uniform amplitude VIV of low mass ratio cylinders. Their results indicate that, for $U^* < 5.5$, f_y locks onto the vortex shedding frequency of a stationary circular cylinder and, for $5.5 < U^* < 8.2$, f_y varies between $0.8f_n$ and $1.1f_n$. However, for $U^* > 8.2$, the frequency response is different to that observed for two DOF uniform amplitude VIV. For $8.2 < U^* < 21$, the results of Flemming & Williamson (2005) show that f_y increases from $1.4f_n$ to $2f_n$ with increasing reduced velocity; whereas for a matching mass ratio, f_y locks onto $1.4f_n$ in the case of uniform amplitude VIV (Jauvtis and Williamson, 2004).

Leong & Wei (2008) investigated the effect of reduced velocity on the frequency response for a very low mass ratio cylinder ($m^* = 0.45$). Their results show that f_y increases linearly with increasing reduced velocity, similar to the results presented in Govardhan & Williamson (2000) for very low mass ratio cylinders undergoing uniform amplitude VIV. Specifically, the results of Leong & Wei (2008) indicate that increasing U^* from 1.1 to 8.3 increases f_y from $0.4f_n$ to $1.4f_n$, respectively.

Flemming & Williamson (2005) and Leong & Wei (2008) show that the frequency of streamwise vibrations is approximately twice that of the transverse vibrations. Consequently, figure-8 type cylinder tip trajectories were observed in both studies, similar to the results for two DOF uniform amplitude VIV of circular cylinders, e.g., Jauvtis and Williamson (2004), Blevins and Coughran (2009), and Sanchis et al. (2008).

2.6 Mitigation of vortex-induced vibrations

Vortex-induced vibrations of cylindrical structures are usually undesirable in engineering applications. Amplitudes of these vibrations can be as high as several peak-to-peak cylinder diameters and may result in fatigue and, consequently, failure of structures (Every et al., 1982 and Dailey et al., 1987). A number of methods have been proposed for suppression of vortex-induced vibrations, e.g., Zdravkovich (1981); Every et al. (1982); and Modi et al. (1995). Modi (1981) classifies these methods into two categories: (i) fluid dynamics methods and (ii) structural methods.

2.6.1 Suppression of vortex-induced vibrations using fluid dynamics methods

The fluid dynamics methods for mitigating VIV rely on disrupting wake vortex shedding of circular cylinders (Zdravkovich, 1981; and Every et al, 1982). This is usually performed either by modifying the surface of the cylinders, known as surface protrusion methods, or by implementing devices in the near wake of the cylinders in order to stabilize the wake, known as near wake stabilizers (Zdravkovich, 1981 and Every et al., 1982).

Several studies have been performed to investigate the effectiveness of surface protrusion devices in suppressing vortex-induced vibrations. These devices perform based on creating streamwise disturbances in the flow and, as a result, reducing the regularity of spanwise vortex shedding in the wake of the cylinder (Zdravkovich, 1981). Figure 2.3 shows three examples of surface protrusion devices, namely, helical strakes, perforated shrouds, and surface bumps. Vickery & Watkins (1964), Price & Thompson (1956), and Owen et al. (2001) investigated the use of helical strakes, perforated shrouds, and surface bumps, respectively, for suppression of VIV of circular cylinders. All of these devices were shown to be effective in suppressing VIV.

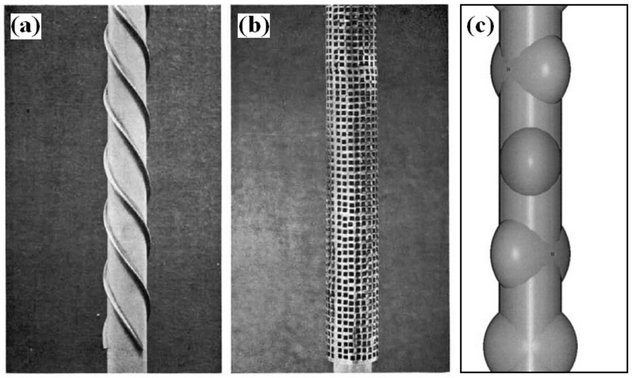

Figure 2.3 Surface protrusion devices: (a) helical strakes (Every et al, 1982); (b) perforated shrouds (Price & Thompson, 1956); and (c) surface bumps (Owen et al., 2001).

Near wake stabilisers, such as splitter plates, have also been shown to be effective in suppressing VIV of circular cylinders, e.g., Sallet (1970), Fischer (1979), and Assi (2009). These devices prevent interaction between the shear layers developing on both sides of the cylinder and, as a result, suppress the alternate vortex shedding in the wake of the cylinder (Zdravkovich, 1981). Fixed, free to rotate, and flexible splitter plates have been shown to suppress vortex-induced vibrations. Sallet (1970) showed that fixed splitter plates with a length of about three cylinder diameters can successfully suppress VIV of circular cylinders. Similarly, Assi (2009) showed that free to rotate splitter plates with length of one cylinder diameter suppress VIV. Fischer et al. (1979) showed that flexible splitter plates can be used to reduce amplitude of vortex-induced vibrations to about 5% of that for a plain cylinder.

2.6.2 Suppression of vortex-induced vibrations using structural methods

The structural methods involve adding an auxiliary vibration absorber device to the main structure (Modi et al., 1995). Tuned-liquid dampers (TLD) and tuned-mass dampers (TMD) are examples of structural methods widely used for the mitigation of vortex-induced vibrations of towers, masts, and chimneys. TLDs are internally partitioned tanks, filled with liquid, usually water, and positioned on top of buildings

(Kareem et al., 1999). The mechanical energy of the buildings equipped with TLDs is dissipated by the movement of the liquid through the partitions inside the tank (Chang & Gu, 1999). The effectiveness of TLDs for the mitigation of vortex-induced vibrations is discussed in detail in Modi et al. (1995), Modi & Seto (1997), and Chang & Gu (1999). In this section, previous studies involving TMDs are discussed due to their relevance to the present investigation.

A tuned-mass damper was invented by Frahm (1911) as a vibration absorber device (Sun et al., 1995). Figure 2.4 shows a schematic of a one DOF TMD attached to a one DOF main structure. As the main structure undergoes vibrations, a phase shift develops between the vibrations of the main structure and the TMD (Kwok & Samali, 1995). The resulting relative motion between the TMD and the main structure allows for the energy of the main structure to be dissipated in the damper installed between the TMD and the main structure (Fig. 2.4).

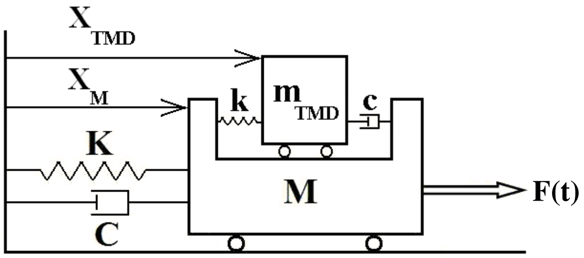

Figure 2.4 Schematic of a one DOF main structure equipped with a one DOF TMD.

The equations of motion of the main structure and the TMD, shown in Fig. 2.4, are given by Eqs. 2.3 and 2.4.

$$M\ddot{X}_M(t) + C\dot{X}_M(t) - c[\dot{X}_{TMD}(t) - \dot{X}_M(t)] + KX_M(t) - k[X_{TMD}(t) - X_M(t)] = F(t) \tag{2.3}$$

$$m_{TMD}\ddot{X}_{TMD}(t) + c[\dot{X}_{TMD}(t) - \dot{X}_M(t)] + k[X_{TMD}(t) - X_M(t)] = 0 \tag{2.4}$$

Tanaka & Mak (1983) showed that the vibrations of the main structure depend on the following six governing parameters:

(i) Forcing frequency band width (B), which can vary from infinity, i.e., white noise excitation, to zero, i.e., single harmonic excitation.

(ii) Normalized dominant forcing frequency ratio ($f_e^* = f_e / f_n$, where f_e is the peak frequency of the power spectral density function of the forcing and f_n is the natural frequency of the main structure equipped when the TMD is restrained to vibrate).

(iii) TMD mass ratio ($\mu = m_{TMD}/M$), where m_{TMD} is the mass of the TMD, and M is the mass of the main structure.

(iv) Tuning frequency ratio ($f_r^* = f_{TMD} / f_n$, where f_{TMD} is the TMD natural frequency).

(v) Main structure damping ratio (ζ).

(vi) TMD damping ratio (ζ_{TMD}).

Tanaka & Mak (1983) investigated the influence of the governing parameters on the main structure vibrations for $\zeta = 0.01$ and $f_e^* = 1$. Their results show that the vibrations of the main structure are minimized for optimal values of tuning frequency, TMD mass ratio, and TMD damping ratio. Tanaka & Mak (1983) made the following conclusions:

(i) The optimal value of tuning frequency ratio, for white noise excitations, i.e., $B = \infty$, does not depend on μ and ζ_{TMD} and occurs at $f_r^* \approx 1$.

(ii) Under tuned condition, i.e., $f_r^* = 1$, the amplitude of vibrations decrease with increasing the TMD mass ratio.

(iii) The optimal value of TMD damping ratio, at $f_r^* = 1$, depends on both B and μ. For $B > 0.1$, the optimal ζ_{TMD} increases with increasing μ. For example, at $B = \infty$, increasing μ from 0 to 0.12 increases the optimal ζ_{TMD} from 0 to 0.16. For $B < 0.1$, increasing μ first increases and then decreases optimal values of ζ_{TMD}. For example, at B = 0.05, increasing μ from 0 to 0.02 increases optimal value of ζ_{TMD} from 0 to 0.03; however, further increase of μ from 0.02 to 0.12 decreases optimal value of ζ_{TMD} from 0.03 to 0.

Tuned-mass dampers have long been used in different industries, e.g., in automotive and aircraft engines for vibration absorption (Xu et al., 1992). During the past few decades, TMDs have been deployed in tall buildings to mitigate seismic as well as vortex-induced vibrations, e.g., Kareem et al. (1999), Sadek et al. (1997), Lin et al. (1999), and Gerges & Vickery (2005). The effectiveness of TMDs for the mitigation of vortex-induced vibrations of one DOF structures has been investigated in several experimental studies, e.g., Tanaka & Mak (1983), Xu et al. (1992), and Kim et al. (2008) have been performed to investigate.

Xu et al. (1992) performed wind tunnel studies to investigate the effect of reduced velocity on VIV of a 1/400 rectangular model equipped with three different TMDs. Their model was free to respond only in streamwise or transverse directions to the flow. Experiments were conducted for two building orientations, with the incident wind normal to the narrow face of the model and to the wide face of the model. The reduced velocity, $U^* = \overline{U}/(f_n b_1)$, was varied between 4 and 18, corresponding to $19\times10^3 < Re_{b_1} < 86\times10^3$, where b_1 is the width of the narrow face of the model and $\overline{U}$ is the mean wind velocity measured at the top of the model. The model aspect ratios, L/b_1 and L/b_2, were 4.1 and 6.2, where L and b_2 are the height of the model and the width of the wide face of the model, respectively. The model had the structural mass ratio (m^*) of 180 and damping ratio (ζ) of 0.01. Three different TMDs with μ = 0.024, ζ_{TMD} = 0.032; μ = 0.033, ζ_{TMD} = 0.04; and μ = 0.044%, ζ_{TMD} = 0.042 were investigated. The tuning frequency ratios of all three TMDs were set to unity, i.e., $f_r^* = 1$. The main results of Xu et al. (1992) can be summarized in as follows.

(i) The time averaged vibrations of the structure in the streamwise direction was not reduced using any of the three TMDs when the wind was either normal to the wide face of the model or to the narrow face.

(ii) For all the cases investigated, the maximum reduction of vibrations was observed for the third TMD, which had the highest mass and damping ratios. Xu et al. (1992) indicate that none of the TMD damping ratios tested was a match to the theoretically obtained optimal values of ζ_{TMD} presented in Tanaka & Mak (1983).

(iii) The rms streamwise vibrations of the main structure were reduced by up to 40% for both model orientations investigated.

(iv) With the incident wind normal to the wide face of the model, the rms transverse vibrations were reduced by up to 30% for $U^* < 10$. For $U^* \geq 10$, the maximum reduction was about 50%.

(v) With the incident wind normal to the narrow face of the model, the rms transverse vibrations were reduced by up to 30%.

3 Experimental methodology

3.1 Water flume facility

All of the experiments were conducted in a water flume facility at the University of Waterloo. The test section of the flume is 2.4 m long and has a 120 cm × 120 cm cross section. Throughout the experiments, the water level was maintained at 80 cm, resulting in a uniform free-stream velocity of 87 ± 1.5 mm/s, with an attendant free-stream turbulence intensity of less than 1%. Further details on the facility and flow characteristics can be found in Morton (2010).

3.2 Vibration measurements

Two Hoskin CP24MHT80 laser-based displacement sensors were used to measure the streamwise and transverse vibrations of the cylinder (Fig. 3.1). The sensors have a 120-mm working range corresponding to ± 2.36 cylinder diameters. Each sensor was calibrated using a high precision milling machine, with details provided in Appendix A. Experimental uncertainties associated with displacement measurements in the streamwise and transverse directions are estimated to be ±0.02D and ±0.015D, respectively, with details provided in Appendix B. Analog signals from the displacement sensors were acquired using NI 6323 PCIe board at a sampling frequency of 600 Hz. This sampling frequency is sufficient to adequately resolve temporal variations in cylinder displacement observed in the present study and is recommended by the sensor manufacturer because it results in optimum linearity of the sensor.

3.3 Frequency and phase angle analyses

Spectral analysis of displacement signals was performed to determine characteristic frequency/frequencies of vibrations. Each displacement signal was discretized into eight segments, with

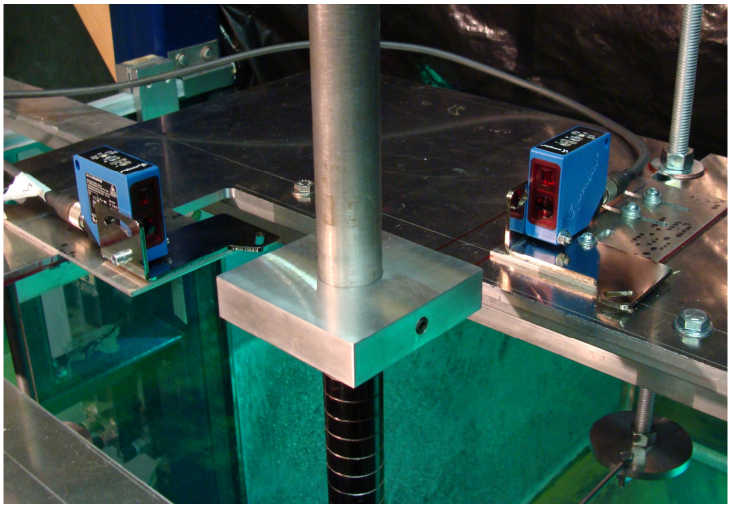

Figure 3.1 Laser sensors.

each segment containing 108,000 data points. Power spectral density (PSD) function of each segment was obtained using the fast Fourier transform (FFT) algorithm and the average PSD was then computed.

To investigate temporal variations in the frequency of vibrations, spectrograms of vibrations were computed using the short-time fast Fourier transform (SFFT) algorithm. A spectrogram presents variation of PSD of a signal in a frequency-time domain. In this study, the width of a time window utilized in the SFFT technique was approximately ten cycles of cylinder oscillations. The overlap between the time windows was approximately one cycle of oscillations. The time window and the overlap between the time windows were selected to resolve expected variations in the frequency of vibrations.

To estimate the phase angle between the streamwise and the transverse vibrations of the structure, the Hilbert transform was utilized. The Hilbert transform of a signal x(t) is given by Eqs. 3.1 and 3.2. The phase of a signal x(t) is equal to the phase of a complex function h(t) given by Eq. 3.2. Further details on the Hilbert transform can be found in Khalak & Williamson (1999).

$$H(x) = \frac{1}{\pi}\int_{-\infty}^{\infty}\frac{x(t)}{t-s}\,dt \qquad (3.1)$$

$$h(t) = x(t) - iH[x(t)] \tag{3.2}$$

3.4 Experimental setup

A steel circular cylinder was placed in the water flume as an inverted pendulum (Fig. 3.2). One end of the cylinder was tapered in order to create a low-friction pivot point at the bottom of the flume. The cylinder was supported with two pairs of springs (Fig. 3.2), one pair aligned parallel and the other orthogonal to the flow direction. The cylinder had a diameter (D) of 25.4 mm and a length (L) of 1.64 m. The total mass (m) and the moment of inertia (I) of the cylinder were 6.42 kg and 5.8 $\text{kg} \times \text{m}^2$, respectively. A technical assembly drawing of the cylinder setup is provided in Appendix C.

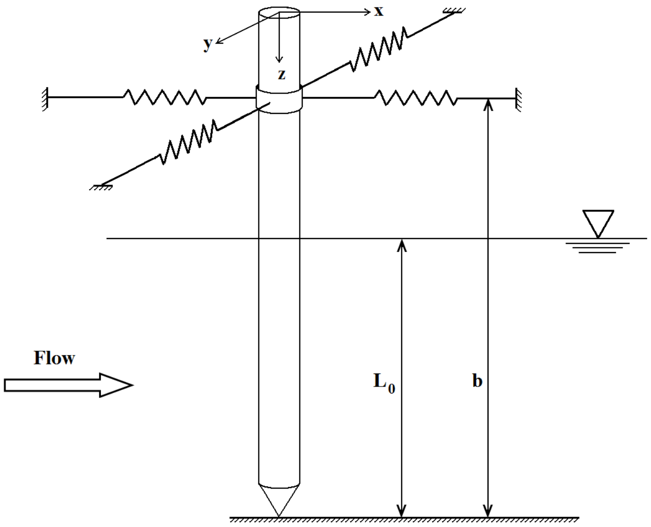

Figure 3.2 Model setup.

To eliminate any Reynolds number effects, the free-stream velocity was maintained constant, corresponding to Re = 2100. The reduced velocity (U^*) was adjusted by varying the natural frequency of the structure (f_n). The natural frequency was determined via spectral analysis of free vibrations of the structure in quiescent water. For all of the cases examined, the natural frequency of the structure in the streamwise direction was equal to that in the transverse direction. Figure 3.3 shows spectra of transverse and streamwise free vibrations in quiescent water, illustrating that the natural frequency is the same in both directions.

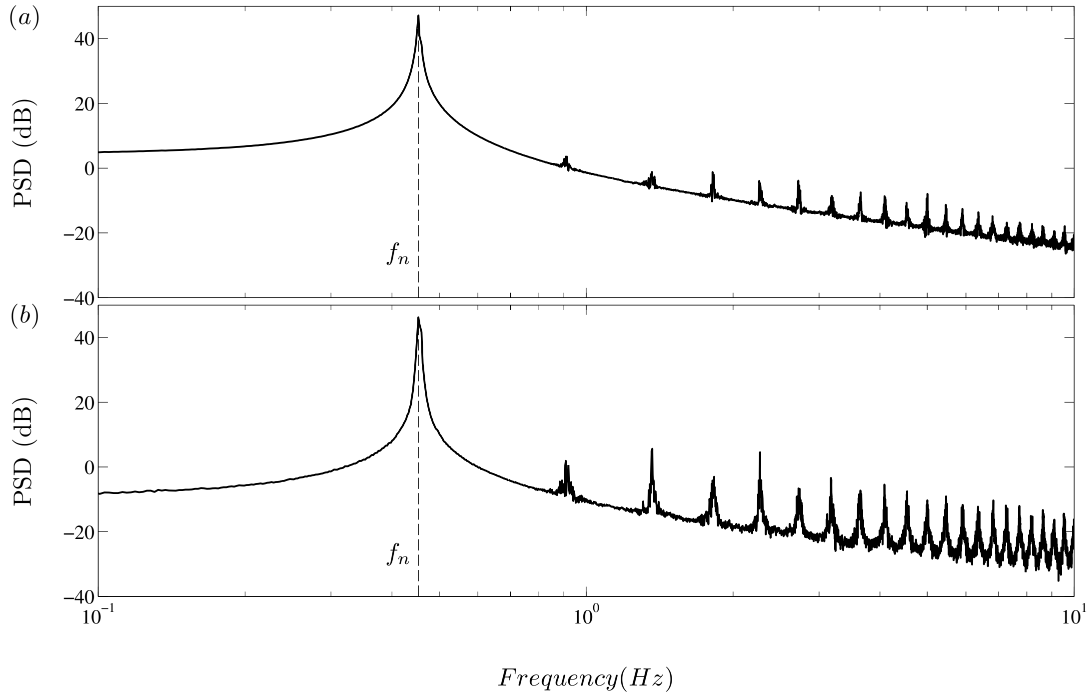

Figure 3.3 Spectra of free vibrations: (a) in the transverse, and (b) streamwise directions.

Three different springs (24.5, 35, and 79.9 N/m) were used throughout the experiments. By changing the stiffness and/or the distance between the springs and the pivot point (b), the natural frequency was varied between 0.31 and 1 Hz, corresponding to $3.4 \leq U^* \leq 11.3$. Figure 3.4 shows the variation of f_n with b for the three different springs utilized in the study.

3.5 Free vibrations

In order to estimate the structural characteristics of the experimental setup, free vibrations in air were considered. Figures 3.5a and b show experimentally measured free vibrations of the cylinder released

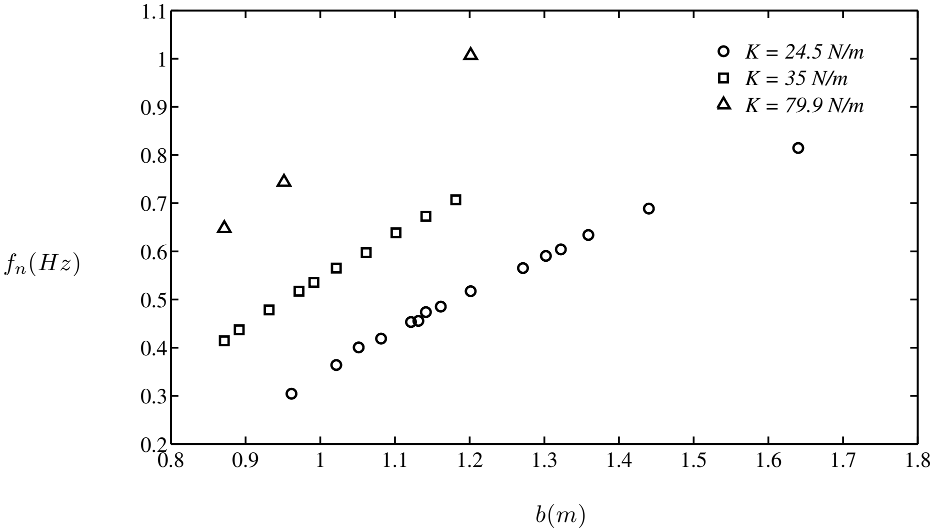

Figure 3.4 Natural frequency and locations of the springs.

from rest at y/D = 1 and x/D = 0. The observed oscillatory and damped response suggests the existence of moderate damping in both directions. Also, since the structure was initially excited in the transverse direction, the presence of vibrations in the streamwise direction indicates structural coupling. To quantify structural damping and coupling from the experimental measurements, a mathematical model of free vibrations was introduced. The model is based on the Newton's second law of motion of the structure (Eqs. 3.3 and 3.4), with the free-body-diagram shown in Fig 3.6.

$$I\frac{d^2}{dt^2}(x/L) + Cb^2\frac{d}{dt}(x/L) + (K_e b^2 - mg\,L/2)(x/L) + K_c b^2(y/L) = 0 \tag{3.3}$$

$$I\frac{d^2}{dt^2}(y/L) + Cb^2\frac{d}{dt}(y/L) + (K_e b^2 - mg\,L/2)(y/L) + K_c b^2(x/L) = 0 \tag{3.4}$$

For both the streamwise and transverse directions (x and y, respectively), the structural stiffness is modeled using a linear spring at z = L-b*,* with an effective stiffness of K_e, and the structural damping is modeled using a linear viscous damper at z = L-b, with a damping coefficient of C. The effect of

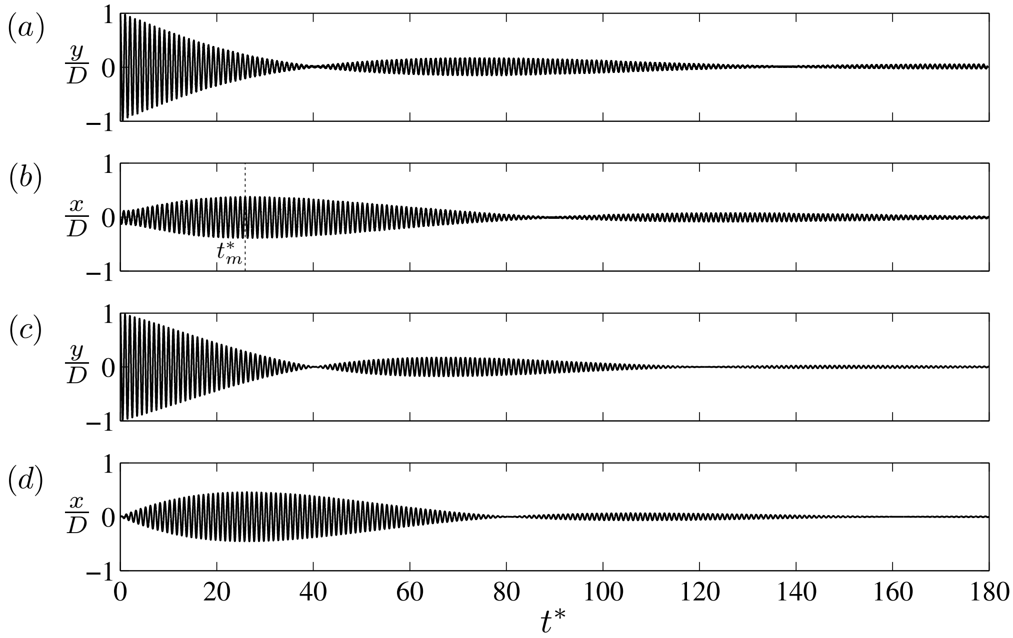

Figure 3.5 Free vibrations of the structure in quiescent air: (a) and (b) experimental data, (c) and (d) corresponding predictions from Eqs. 3.3 and 3.4 with $\zeta = 0.004 \pm 0.0014$ and $f_c / f_a = 0.110 \pm 0.014$.

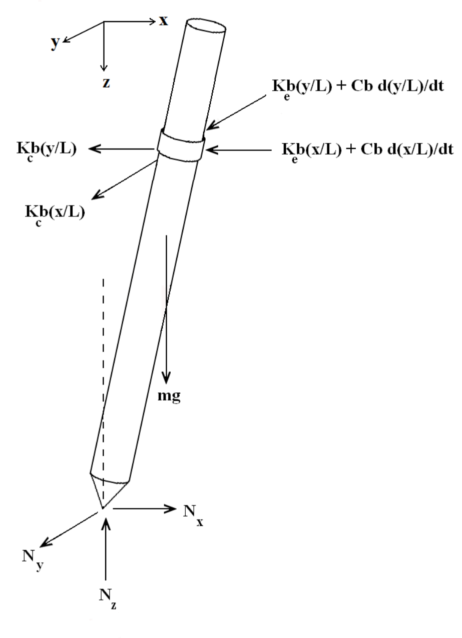

Figure 3.6 Free-body-diagram of the cylinder model in free-vibrations.

aerodynamic forces is neglected. The coupling between vibrations in the x and y directions is modeled using the cross-stiffness term (K_c), similar to the approach proposed in Wardlaw et al. (1975). Introducing the in-air natural frequency, $f_a = [1/(2\pi)]\sqrt{(K_e b^2 - mgL/2)/I}$, structural damping ratio, $\zeta = Cb^2/[2\sqrt{I(K_e b^2 - mgL/2)}]$, and coupling frequency, $f_c = [b/(2\pi)]\sqrt{K_c/I}$, Eq. 3.3 and 3.4 can be reduced to the following non-dimensional form:

$$\ddot{x}/D + 4\pi\zeta\,\dot{x}/D + 4\pi^2\,x/D + 4\pi^2(f_c/f_a)^2\,y/D = 0 \qquad (3.5)$$

$$\ddot{x}/D + 4\pi\zeta\,\dot{x}/D + 4\pi^2\,x/D + 4\pi^2(f_c/f_a)^2\,y/D = 0 \qquad (3.6)$$

where $\dot{(\cdot)}$ denotes differentiation with respect to the normalized time t^* ($t^* = t \times f_a$). For $f_c/f_a < 1$ and $\zeta^2 << 1$, verified to be the case in the present study, these equations can be solved analytically. With the initial conditions ($x/D = 0$, $y/D = y_0/D$), the solution is given by:

$$x(t^*)/D = -(y_0/D)e^{-2\pi\zeta t^*}\sin[\pi(f_c/f_a)^2 t^*]\sin(2\pi t^*) \qquad (3.7)$$

$$y(t^*)/D = (y_0/D)e^{-2\pi\zeta t^*}\cos[\pi(f_c/f_a)^2 t^*]\cos(2\pi t^*) \qquad (3.8)$$

Details of the analytical derivation of Eqs. 3.7 and 3.8 are provided in Appendix D. The natural frequency of the structure in air was determined via spectral analysis of the free vibrations of the structure in quiescent air, with the uncertainty estimated to be less than about 2%. Details of the uncertainty analysis are provided in Appendix B. Similar to the free vibration tests in water the natural frequency in the streamwise direction was equal to that in the transverse direction for all the cases examined. The damping ratio and the coupling frequency were determined using Eqs. 3.7 and 3.8 and experimental data. Specifically, it can be inferred from Eq. 3.8 that the classical logarithmic decay of the amplitude occurs at the onset of free vibrations in the y direction ($t^* \to 0$). Thus, the damping ratio can be estimated as:

$$\zeta = \frac{1}{2\pi}\ln\left[\left(\frac{y_0}{D}\right) \Big/ \left(\frac{y(t^* = 1)}{D}\right) \right] \tag{3.9}$$

For a given f_a and ζ, the coupling frequency can be estimated from Eqs. 3.7 and 3.8 using experimental free-vibrations data. To minimize the uncertainty, the following approach is employed. Based on the experimental data, the normalized time (t_m^*) at which the amplitude of streamwise vibrations attains its maximum value is determined (Fig. 3.5b). From Eq. 3.7, the two conditions that must be satisfied at t_m^* are given by Eqs. 3.10 and 3.11.

$$\frac{d}{dt^*}\left\{ -e^{-2\pi\zeta t^*} \sin[\pi(f_c/f_a)^2 t^*] \right\}_{t^*=t_m^*} = 0 \tag{3.10}$$

$$\frac{d^2}{dt^{*2}}\left\{ -e^{-2\pi\zeta t^*} \sin[\pi(f_c/f_a)^2 t^*] \right\}_{t^*=t_m^*} < 0 \tag{3.11}$$

The derivatives in Eqs. 3.10 and 3.11 can be readily evaluated, and then the coupling frequency (f_c) can be determined numerically for the known f_a, ζ, and t_m^*.

Figures 3.5c and d depict the results obtained using Eqs. 3.5 and 3.6 to model free vibrations of the structure shown in Figs. 3.5a and b. The analytical and experimental results are in close agreement, suggesting that Eqs. 3.5 and 3.6 provide a reasonable dynamic model for the structure under investigation.

3.6 Flow visualization

A Laser-Induced-Fluorescence (LIF) technique was used to visualize the wake vortex shedding patterns at two different planes perpendicular to cylinder axis (Fig. 3.7). The planes were located inside the uniform region of the incoming flow at z/L = 0.65, and 0.84. A 2.5 mm diameter probe (Fig. 3.8) was used to inject dye into the flow. Two types of dye were used, namely, a 1000 ppm solution of Rhodamine 6G and a 24 ppm solution of Fluorescein Sodium salt. The probe was positioned about one diameter upstream of the cylinder. The Reynolds number based on the probe diameter was such that vortex shedding occurred in the wake of the probe. Thus, to minimize any adverse effect on the flow a bent probe was utilized (Fig. 3.8).

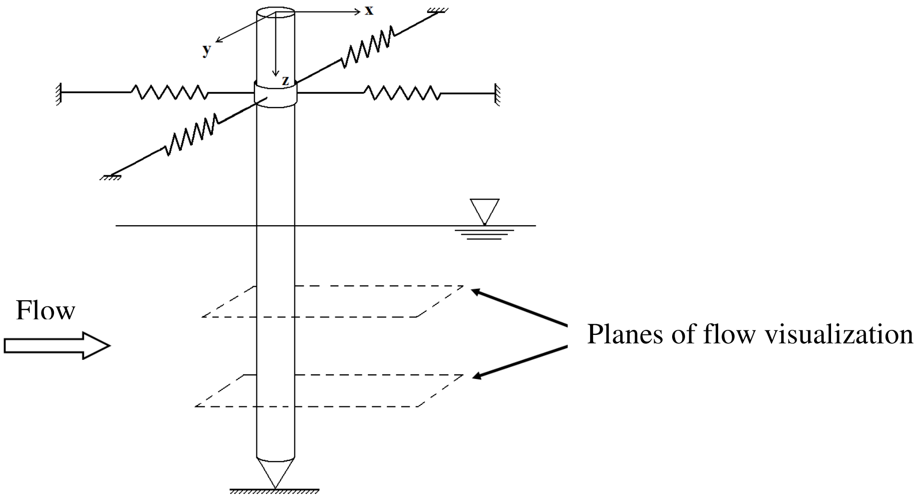

Figure 3.7 Planes of flow visualization.

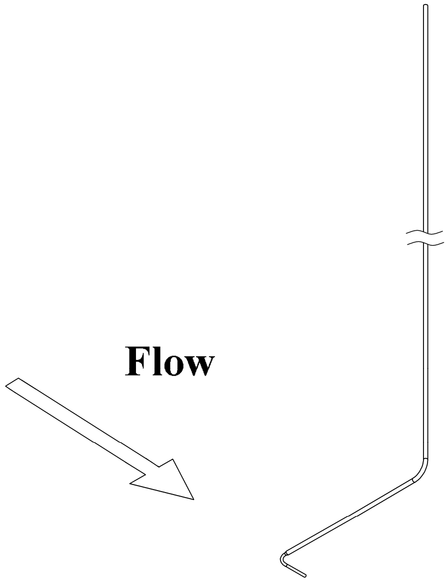

Figure 3.8 Dye injection probe.

The flow was illuminated with a laser sheet. A laser beam with a wavelength of 570 nm was produced using a continuous wave Ion-Argon laser (Spectra-Physics stabilite 2017). The beam was passed through a concave lens to generate the laser sheet used to illuminate the injected dye in the wake of the cylinder. The spanwise location of the sheet was adjusted using a manual traversing system.

Flow visualization images were acquired using a Nikon D300 camera, at an average rate of 6 frames per second. Also, video recordings were made to allow a more detailed analysis of the vortex shedding patterns.

3.7 Tuned mass damper setup

A novel adaptive pendulum tuned-mass damper used in this study is shown in Fig. 3.9. The TMD was built by Mr. Richard Lourenco based on a larger scale model developed for suppressing forced vibrations (Lourenco, 2011). The TMD was integrated with the cylindrical structure in order to investigate the capabilities of this novel design for mitigating vortex-induced vibrations. The technical drawing of the cylindrical structure equipped with the TMD is provided in Appendix C.

The investigated pendulum tuned-mass damper can autonomously adjust its natural frequency as shown in Fig. 3.9. The TMD setup consists of a supporting frame, a pendulum, two dampers, and tuning components. The supporting frame is mounted on top of the cylinder model. The frame consists of two base supports, two guiding rails, and a top supporting plate.

The pendulum consists of a 0.7 kg mass suspended on a 1-m-long steel cable. The length of the pendulum can be adjusted so as to control TMD natural frequency (f_{TMD}). This is done by varying the position of a tuning platform sliding on the guide rails, thereby varying the effective length of the pendulum. A Portescap 42M048C1B-Z36 bipolar stepper motor is used to position the tuning platform along the guide rails. A Micro-Epsilon WPS-150-MK30-P25 string potentiometer was utilized to acquire position of the tuning platform.

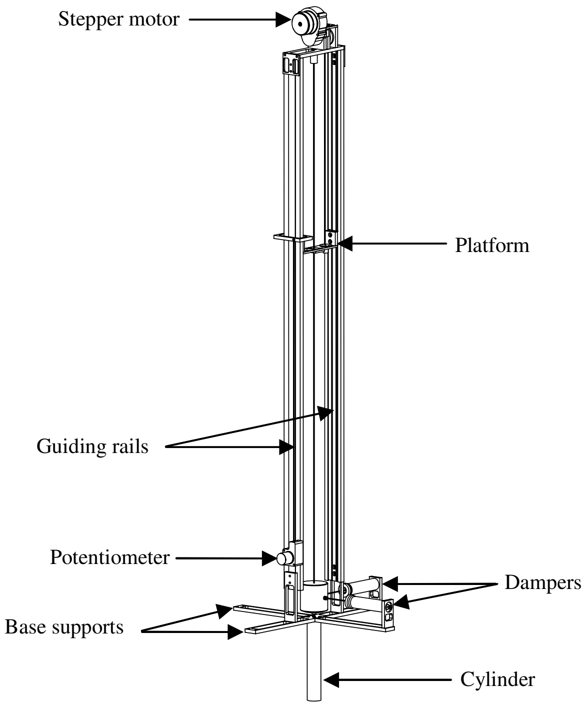

Figure 3.9 Tuned-Mass Damper.

Two Airpot 2K160 dashpot dampers were utilized in order to absorb vibrations of the cylindrical structure. One damper is aligned parallel and the other orthogonal to the flow direction (Fig. 3.9). One end of each damper is connected to the suspended mass using a ball joint. The other end of each damper is attached to the base supports. Each damper is equipped with a control valve. Calibration experiments presented in Lourenco (2011) indicated that the damping coefficient of each damper (C_{TMD}) depends on: (i) position of the control valve, and (ii) suspended mass vibration frequency. All of the experiments were performed with the control valves fully opened. As will be shown later, at the lock-in condition, the pendulum mass vibration frequency is equal to the natural frequency of the structure. Thus, for a given position of the control valves, the damping coefficient of the dampers depends only on the natural frequency at the lock-in condition. From the calibration results presented in Lourenco (2011), it can be inferred that $C_{TMD} = 2.128f_n$. Thus, $\zeta_{TMD} = \frac{C_{TMD}}{4\pi m_{TMD} f_n} = 0.24$.

The adaptive TMD was controlled using a dSPACE 1104 board. Also, the board was used to simultaneously acquire data from laser displacement sensors and the string potentiometer. The detailed description of the TMD control algorithm is provided in Lourenco (2011).

4 Vortex-induced vibrations of a pivoted circular cylinder

This chapter presents results characterizing VIV of the model without a TMD. For the experimental setup utilized in the present investigation (Fig. 3.2), dimensional analysis was employed to show that the vortex-induced vibrations depend on the Reynolds number (Re), moment of inertia ratio (I^*), mass ratio (m^*), aspect ratio (AR), reduced velocity (U^*), damping ratio (ζ), and coupling-frequency-based reduced velocity, ($U_c^* = U/(f_c D)$). The values of the governing parameters investigated in the present study are tabulated in Table 4.1.

4.1 Amplitude of response

The amplitude response is defined as half peak-to-peak amplitude of cylinder tip undergoing steady state oscillations. Figure 4.1 shows the variation of the normalized transverse amplitude of vibrations (A_y^*) with reduced velocity. The results are presented for the three different spring sets utilized to support the cylinder. Figure 4.1 shows that the extent of the region with relatively high amplitudes of vibrations does not change significantly by changing the spring stiffness. However, within this range, the amplitude of transverse vibrations can vary substantially with varying spring stiffness for a given reduced velocity. For example, at $U^* = 6.6$, increasing the spring stiffness from 25.4 to 35 N/m decreases A_y^* by about 33%. It should be noted that, no hysteresis in the amplitude of response was observed in the present study. As discussed in Khalak and Williamson (1999), the hysteresis occurs when U^* is varied by adjusting the free-stream velocity; whereas, in the present investigation, the free-stream velocity was kept constant throughout all of the experiments.

Figure 4.2 shows the variations of deflection angle (δ) with the reduced velocity for the present investigation as well as the studies of Flemming & Williamson (2005) and Leong & Wei (2008). The deflection angle is defined as the maximum angle that the projection of cylinder axis on the z-y plane

Table 4.1 Governing non-dimensional parameters.

Parameter	Description	Value
Re	Reynolds number, UD/υ	2100
I^*	Moment of inertia ratio, I/I_d	66.8
m^*	Mass ratio, m/m_t	15.9
AR	Aspect ratio, L/D	64.6
U^*	Reduced velocity, $U/(f_nD)$	3.4 – 11.3
ζ	Damping ratio, $C/(4\pi m f_n)$	0.004 – 0.011
U_c^*	Coupling-frequency-based reduced velocity, $U/(f_cD)$	13.8 – 47.7

makes with the z axis, which is given by $\delta = \tan^{-1}(A_y/L)$. Since A_y/L is very small ($A_y/L \sim 10^{-2}$), the deflection angle can be estimated as: $\delta = A_y^*/AR$. It should be noted that the results from the three investigations, shown in Fig. 4.2, were obtained for different Re, I^*, m^*, ζ, and AR. Thus, the differences between the three data sets are attributed to the differences in the governing experimental parameters. The

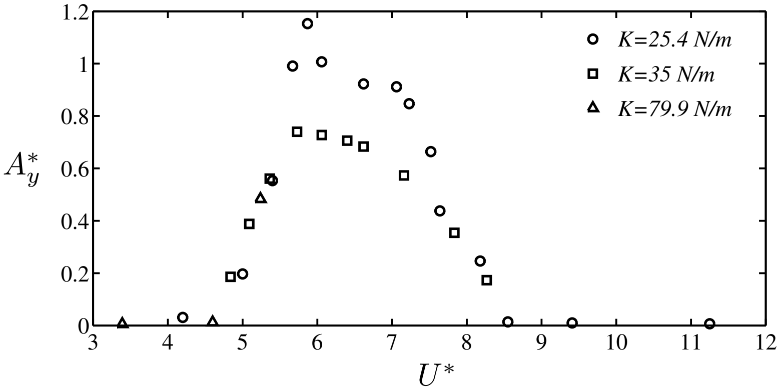

Figure 4.1 Transverse amplitude of response. The uncertainty is accommodated by the size of the data legends.

results of the present investigation show that the region with relatively high amplitudes of vibrations extends over $5 \leq U^* \leq 8.2$. However, the results of Flemming & Williamson (2005) show that substantial amplitudes of vibrations are observed over a wider range, i.e., $4.6 \leq U^* \leq 10.9$. This is speculated to be due to the mass ratio in the present investigation being higher than that of Flemming & Williamson (2005). In contrast to the trends observed in the present investigation and that of Flemming & Williamson (2005), the results of Leong & Wei (2008), presented in Fig. 4.2, indicate that the deflection angle increases with increasing the reduced velocity beyond $U^* \approx 5$. The results of Leong & Wei (2008) pertain to $m^* = 0.45$, which is lower than the critical mass ratio. The trend observed in the results of Leong & Wei (2008) is similar to that reported for one DOF very low mass ratio cylinders by Govardhan and Williamson (2000).

The results presented in Fig. 4.1 show that distinctly different normalized transverse amplitudes of response can occur for the different springs utilized in the study. Since the Reynolds number, moment of inertia ratio, mass ratio, and aspect ratio were kept constant throughout the experiments, the differences observed between the amplitudes of response pertaining to different springs in Fig. 4.1 are attributed to the effect of ζ and/or U_c^*. The effect of damping ratio, which is of particular practical importance, is

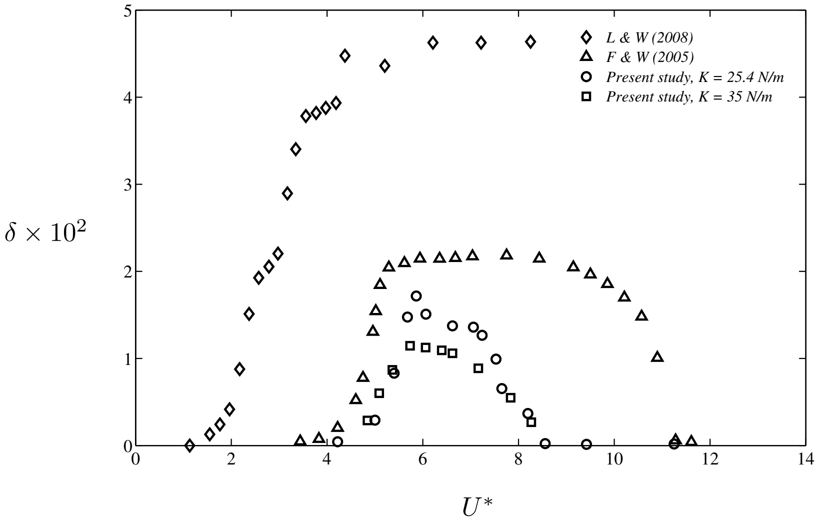

Figure 4.2 Variation of the transverse deflection angle with the reduced velocity. Data labeled L & W (2008) and F & W (2005) correspond to studies of Leong & Wei (2008) and Flemming & Williamson (2005), respectively.

illustrated in Fig. 4.3, where the normalized amplitudes of response pertaining to $U_c^* = 35.7 \pm 1.3$ are presented. Agreeing with Sarpkaya (1995) and Blevins and Coughran (2009), the results show that the damping ratio can influence significantly the transverse amplitude of vibrations. For example, comparing the transverse amplitude of response at $U^* = 7.6$ shows that increasing the damping ratio by about 50% reduces the transverse amplitude of vibrations by about 25%. The results in Fig. 4.3 also show that the amplitude of streamwise vibrations is relatively low ($A_x^* < 0.2$) compared to the transverse vibrations and does not exhibit a well defined maximum.

4.2 Frequency of response

Figure 4.4 shows the variation of the normalized frequency of transverse vibrations ($f_y^* = f_y / f_n$) with the reduced velocity. The frequency values shown were obtained via spectral analysis of transverse oscillations, with representative spectra depicted in Fig. 4.5. Distinct regions of frequency response can be

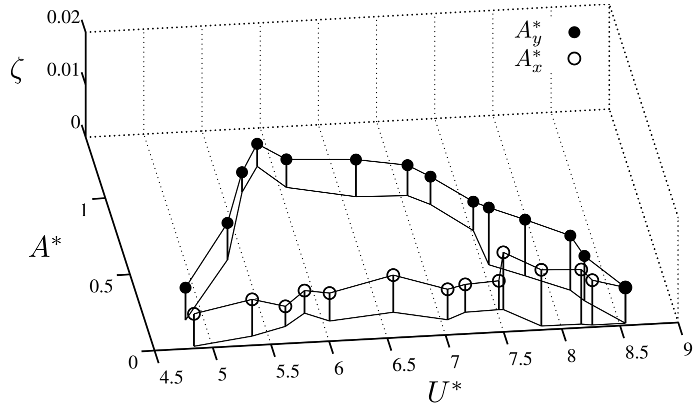

Figure 4.3 Transverse and streamwise amplitudes of response at $U_c^* = 35.7 \pm 1.3$.

identified in Fig. 4.4. For $4.9 < U^* < 8.6$, spectra of transverse vibrations, depicted in Fig. 4.5a, display a single dominant peak centered at the natural frequency, similar to the results for uniform amplitude VIV of one and two DOF cylinders with moderate to high mass ratios ($m^* > 6$), e.g., Jauvtis & Williamson (2004) and Blevins & Coughran (2009). A comparative analysis of the present results and those of Flemming & Williamson (2005) and Leong & Wei (2008) indicates that, in the synchronization region, decreasing the mass ratio causes the frequency of transverse vibrations to deviate from the natural frequency, with more significant deviations occurring at lower mass ratios. Outside of the synchronization region, i.e., for $3.4 < U^* < 4.9$ and $8.6 < U^* < 11.3$, spectra of transverse vibrations, depicted in Figs. 4.5b and c, feature several peaks centered at the vortex shedding frequency of a stationary circular cylinder (f_s), the natural frequency, and the harmonics of the natural frequency.

Figures 4.6a-c show the spectrograms of transverse vibrations at $U^* = 6.6$, 3.4, and 11.25, corresponding to the results presented in Figs. 4.5a-c. The results show that, in the synchronization region (Fig. 4.6a), the energy content associated with the dominant frequency of vibrations (f_n) does not vary with time. In contrast, in the non-synchronized region (Figs. 4.6b and c), noticeable temporal fluctuations are observed in the energy content of the two dominant frequencies, i.e., f_n and f_s.

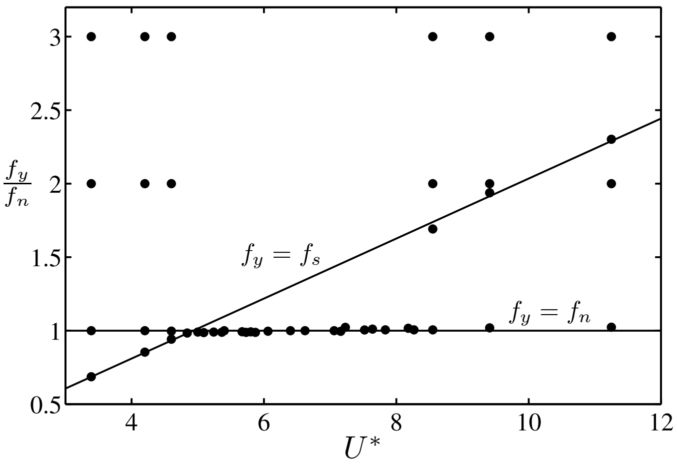

Figure 4.4 Frequencies of transverse vibrations.

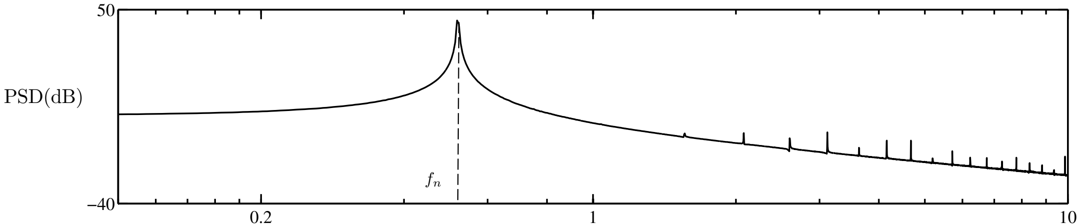

(a) $U^* = 6.6$

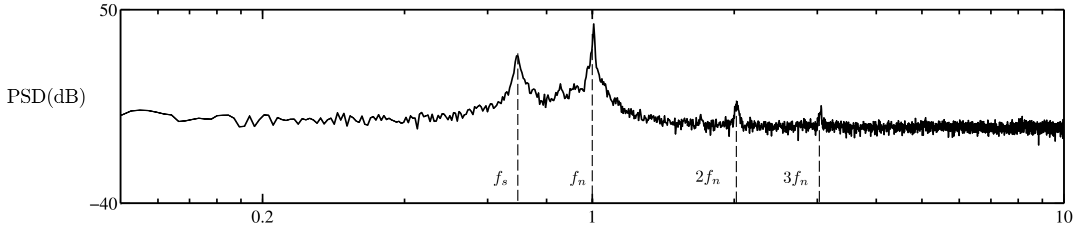

(b) $U^* = 3.4$

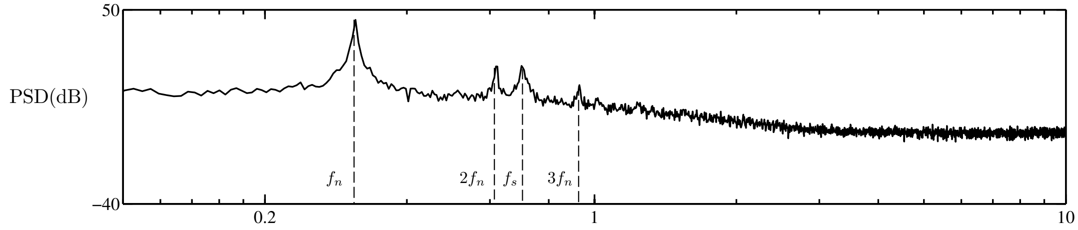

(c) $U^* = 11.25$

Figure 4.5 Spectra of transverse vibrations.

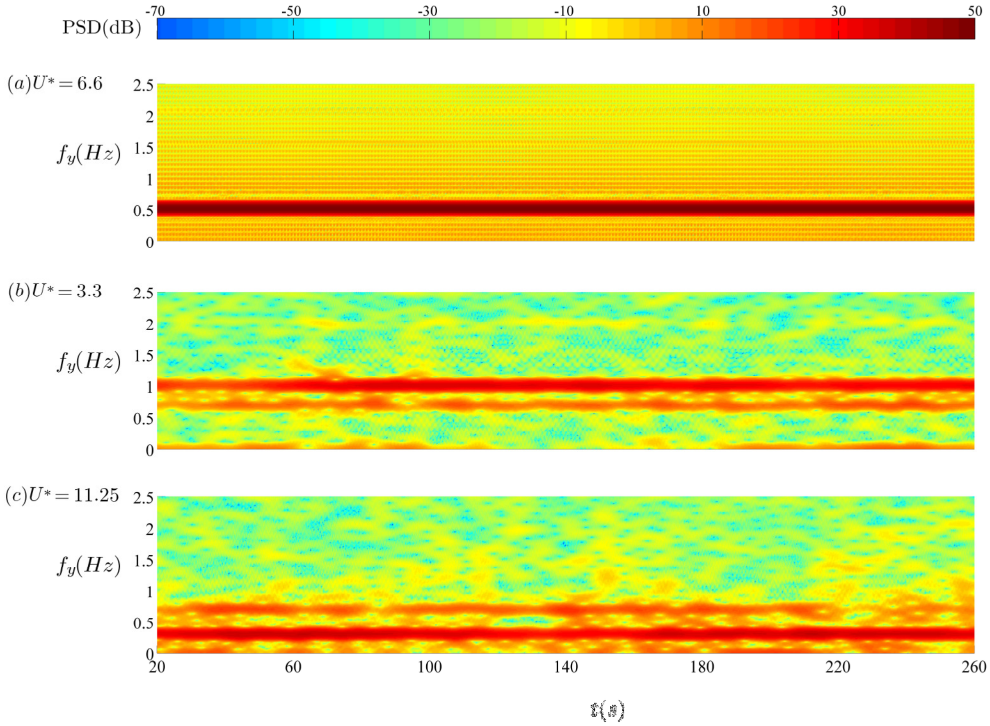

Figure 4.6 Spectrograms of transverse vibrations.

Spectral analysis of streamwise vibrations showed that the frequency of streamwise vibrations locks onto the natural frequency of the structure in the synchronization region, as illustrated in Fig. 4.7. Thus, in the synchronization region, the frequencies of both the streamwise and transverse vibrations match the natural frequency of the structure, so that the cylinder traces elliptic trajectories which will be discussed in detail in section 4.3. Although such a response has been observed in vortex-induced vibrations of cylindrical structures, e.g., Ishizaki (1967) and Vandiver et al. (2005), in laboratory investigations involving pivoted circular cylinders, e.g., Flemming & Williamson (2005) and Leong & Wei (2008), the classical figure-8 response was observed, with streamwise frequency of oscillations being twice that of the transverse oscillations. Thus, it is of interest to investigate a mechanism responsible for

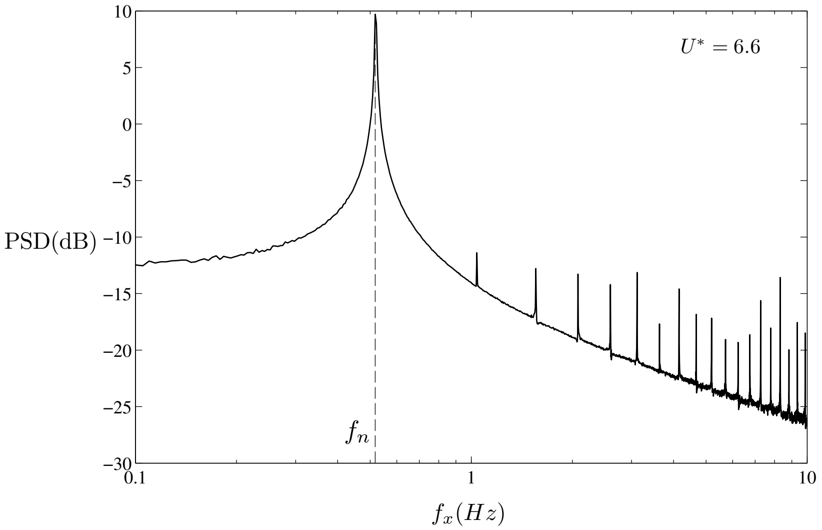

Figure 4.7 Spectrum of streamwise vibrations.

the occurrence of either figure-8 or elliptic trajectories for cylindrical structures undergoing VIV. To facilitate this, the following simplified mathematical model based on the equations of motion of the structure is considered:

$$\mathrm{I}\frac{\mathrm{d}^2}{\mathrm{dt}^2}(\mathrm{x/L}) + \mathrm{Cb}^2\frac{\mathrm{d}}{\mathrm{dt}}(\mathrm{x/L}) + (\mathrm{K_e b^2} - \mathrm{mg\,L/2} + \mathrm{m_d g\,L_0/2})(\mathrm{x/L}) + \mathrm{K_c b^2}(\mathrm{y/L}) = \mathrm{M_x(t)} \tag{4.1}$$

$$\mathrm{I}\frac{\mathrm{d}^2}{\mathrm{dt}^2}(\mathrm{y/L}) + \mathrm{Cb}^2\frac{\mathrm{d}}{\mathrm{dt}}(\mathrm{y/L}) + (\mathrm{K_e b^2} - \mathrm{mg\,L/2} + \mathrm{m_d g\,L_0/2})(\mathrm{y/L}) + \mathrm{K_c b^2}(\mathrm{x/L}) = \mathrm{M_y(t)} \tag{4.2}$$

The model is similar to the mathematical model proposed in Flemming & Williamson (2005). However, the proposed model incorporates the effect of coupling observed in the free-vibration tests, which is modeled utilizing the same approach as that employed in the free-vibration model. The structural moments in Eqs. 4.1 and 4.2, i.e., the inertial, damping, restoring, and cross-stiffness moments, are balanced by the fluid moments exerted on the structure, i.e., $M_x(t)$ and $M_y(t)$. As suggested by Flemming & Williamson (2005), the fluid moments can be decomposed into the total instantaneous fluid forcing moment and the fluid inertia moment as follows:

$$M_x(t) = \int_{L-L_0}^{L} F_x(z,t)(L-z)dz - I_A \frac{d^2(x/L)}{dt^2}$$

$$M_y(t) = \int_{L-L_0}^{L} F_y(z,t)(L-z)dz - I_A \frac{d^2(y/L)}{dt^2}$$

where $F_x(z,t)$ and $F_y(z,t)$ are the instantaneous local forces per unit length exerted from the fluid to the structure in the streamwise and transverse directions, respectively, and I_A is the added moment of inertia. Following Jauvtis & Williamson (2004) and Flemming & Williamson (2005), it is assumed that, in the synchronization region, the forcing frequencies in the transverse and the streamwise directions are equal to the natural frequency (f_n) and twice the natural frequency ($2f_n$) of the structure, respectively. Thus, incorporating a phase difference (ψ) between the forcing in the streamwise and transverse directions, the forces per unit length in the x and y directions can be modeled as $F_x(z,t) = 0.5\rho U^2 D C_x(z)\sin(2\omega_n t + \psi)$ and $F_y(z,t) = 0.5\rho U^2 D C_y(z)\sin(\omega_n t)$, respectively. As shown in Jauvtis & Williamson (2004), force coefficients C_x and C_y are proportional to the local amplitude of oscillations in the streamwise and transverse directions, respectively. With the linear variation of the amplitudes of vibrations along the cylinder span, the force coefficients can be expressed as $C_x(z) = C_D(L-z)/L_0$ and $C_y(z) = C_L(L-z)/L_0$. Introducing $f_n = [1/(2\pi)]\sqrt{(K_e b^2 - mgL/2 + m_d g L_0/2)/(I + I_A)}$, $f_r = (f_a/f_n)[I^*/(I^* + C_A)]$, and $U_r = (U^*/U_c^*)^2[I^*/(I^* + C_A)]$, where C_A is the added mass coefficient, Eqs. 4.1 and 4.2 can be cast in a non-dimensional form as follows:

$$x''/D + 4\pi\zeta f_r\, x'/D + 4\pi^2\, x/D + 4\pi^2 U_r\, y/D = \frac{2}{\pi} C_D \frac{L}{L_0} \frac{U^{*2}}{(I^* + C_A)} \sin(4\pi t^{**} + \psi) \qquad (4.3)$$

$$y''/D + 4\pi\zeta f_r\, y'/D + 4\pi^2\, y/D + 4\pi^2 U_r\, x/D = \frac{2}{\pi} C_L \frac{L}{L_0} \frac{U^{*2}}{(I^* + C_A)} \sin(2\pi t^{**}) \qquad (4.4)$$

where $()'$ denotes the differentiation with respect to t^{**} ($t^{**} = tf_n$). For $f_c/f_n < 1$ and $\zeta^2 << 1$, the steady state solution of Eqs. 4.3 and 4.4 can be obtained analytically and is given by Eqs. 4.5 and 4.6.

$$x_{ss}(t^{**})/D = \frac{A}{U_r}[a_3 \sin(4\pi t^{**}) + a_4 \cos(4\pi t^{**})] + B(\frac{U^*}{U_c^*})^2 \sin(2\pi t^{**}) \tag{4.5}$$

$$y_{ss}(t^{**})/D = A[a_1 \sin(4\pi t^{**}) + a_2 \cos(4\pi t^{**})] - B(2\zeta \frac{f_a}{f_n}) \cos(2\pi t^{**}) \tag{4.6}$$

where A, B, a_1, a_2, a_3, and, a_4 are presented in Table 4.2 for conciseness. Detailed derivations are provided in Appendix E.

Although due to its simplified formulation the proposed mathematical model is not expected to provide accurate estimates of VIV characteristics, it allows analyzing important trends in the frequency response. In particular, Eqs. 4.5 and 4.6 suggest that the frequency response in the x and y directions involve the natural frequency of the structure (f_n) and its first harmonic ($2f_n$). To determine the dominant frequency in each direction, the ratio of the amplitude associated with f_n and that associated with $2f_n$ can be evaluated from Eqs. 4.5 and 4.6 for the streamwise and transverse vibrations, respectively. These ratios, R_x and R_y, are given in Eqs. 4.7 and 4.8.

$$R_x = \frac{B}{A} \frac{(U^*/U_c^*)^2}{\sqrt{a_3^2 + a_4^2}} U_r \tag{4.7}$$

$$R_y = \frac{B}{A} \frac{2\zeta(f_a/f_n)}{\sqrt{a_1^2 + a_2^2}} \tag{4.8}$$

where A, B, a_1, a_2, a_3, and, a_4 are presented in Table 4.2.

It can be shown that:

$$\sqrt{a_3^2+a_4^2}=\sqrt{\{4\zeta f_r[6U_r+16\zeta^2 f_r^2+(U_r-3)^2]\}^2+\{3[U_r^2-9-16\zeta^2 f_r^2]\}^2}$$

$$\sqrt{a_1^2+a_2^2}=\sqrt{(U_r^2-9+16\zeta^2 f_r^2)^2+(24\zeta f_r)^2}$$

Table 4.2 Coefficients in Eqs. 4.5 - 4.8.

A	$\dfrac{U_r C_D (L/L_0) U^{*2}}{2\pi^3 (I^* + C_A)[16\zeta^2 f_r^2 + (U_r-3)^2][16\zeta^2 f_r^2 + (U_r+3)^2]}$
B	$\dfrac{C_L (L/L_0) U^{*2}}{2\pi^3 (I^* + C_A)[4\zeta^2 (f_a/f_n)^2 + (U^*/U_c^*)^4]}$
a_1	$(U_r^2 - 9 + 16\zeta^2 f_r^2)\cos(\psi) + 24\zeta f_r \sin(\psi)$
a_2	$-24\zeta f_r \cos(\psi) + (U_r^2 - 9 + 16\zeta^2 f_r^2)\sin(\psi)$
a_3	$4\zeta f_r[6U_r + 16\zeta^2 f_r^2 + (U_r-3)^2]\sin(\psi) + 3[U_r^2 - 9 - 16\zeta^2 f_r^2]\cos(\psi)$
a_4	$3[U_r^2 - 9 - 16\zeta^2 f_r^2]\sin(\psi) - 4\zeta f_r[6U_r + 16\zeta^2 f_r^2 + (U_r-3)^2]\cos(\psi)$

Thus, R_x and R_y, given by Eqs. 4.7 and 4.8, are independent of ψ and depend on U^*, U_c^*, ζ, C_L/C_D, f_a/f_n, and I^*. Using the results of Jauvtis & Williamson (2004) to estimate C_L/C_D, a parametric analysis of Eqs. 4.7 and 4.8 showed that, for a range of influencing parameters feasible in practical applications, R_x and R_y depend primarily on U_c^* and ζ in the synchronization region. Representative results for R_x are depicted in Fig. 4.8. Two distinct regions can be identified in the data presented: (i) a region corresponding to $R_x > 1$ and (ii) a region corresponding to $R_x < 1$. For lower U_c^*, i.e., for structures with stronger coupling, the mathematical model predicts $R_x > 1$, so that vibrations in the streamwise direction occur primarily at $f_x = f_n$. Thus, in agreement with the present experimental results, the frequency of vibrations in the streamwise direction is expected to lock onto the natural frequency for $R_x >> 1$. In contrast to the experimental setup used in the present investigation, Flemming & Williamson (2005) and Leong & Wei (2008) mounted a rigid cylinder on a pin. In such an arrangement, the pin can be approximated as a Bernoulli beam (i.e., a beam with an aspect ratio of more than ten), and vibrations in the x and y directions are expected to be weakly coupled. Indeed, Flemming & Williamson (2005) did not incorporate any coupling in their mathematical model. Thus, for the structures investigated in Flemming & Williamson (2005) and Leong & Wei (2008), K_c is expected to be negligible, i.e., $U_c^* \to \infty$. It follows from Eq. 4.7 that $R_x \to 0$ when $U_c^* \to \infty$, which implies that $f_x \to 2f_n$ when $U_c^* \to \infty$, corresponding to the results of Flemming & Williamson (2005) and Leong & Wei (2008). To validate this argument, an experimental setup with weak coupling between the streamwise and transverse vibrations, similar to the arrangement utilized in Flemming & Williamson (2005), was also tested in the present investigation. In agreement with the results presented in Fig. 4.8 for structures with weak coupling, experimental results demonstrated that $f_x = 2f_n$, with details provided in Appendix F. The analysis of Eq. 4.8 showed that $R_y >> 1$ for all the parameters investigated, implying $f_y = f_n$. Therefore, the mathematical model demonstrates that, for structures with significant coupling, vortex-induced vibrations in the streamwise and transverse directions lock onto the natural frequency of the structure, resulting in elliptic trajectories. On the other hand, for structures with weak coupling, the frequencies of streamwise and transverse vibrations lock onto $2f_n$ and f_n, respectively, so that the cylinder traces figure-8 type trajectories. This analysis agrees with experimental observations in Flemming & Williamson (2005), Leong & Wei (2008), and the present study and shows that either elliptic or figure-8 type trajectories can be observed depending on the structural characteristics, in particular, structural coupling.

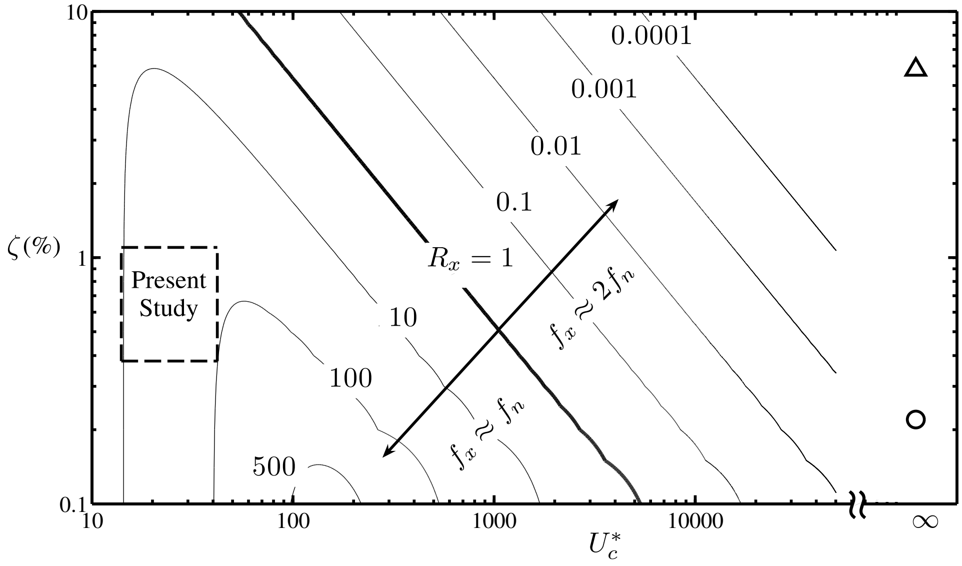

Figure 4.8 R_x contours computed from Eq. 4.7 for $U^* = 6.5$, $C_L/C_D = 0.9$, $f_a/f_n = 1$, and $I^* = 66.8$. Dashed lines mark the region corresponding to the experimental conditions in the present study; Δ - Leong & Wei (2008); ○- Flemming & Williamson (2005).

4.3 Cylinder trajectories

Experimental results indicate that there exist four types of elliptic trajectories, with representative experimental results shown in Fig. 4.9. The results demonstrate that the orientation and direction of orbiting vary with experimental conditions. Two special cases of the observed elliptic trajectories are depicted in Fig. 4.10, where elliptic trajectories are stretched to straight line segments.

Since the frequencies of streamwise and transverse vibrations were shown to lock onto the natural frequency of the structure in the synchronization region, the following equations can be used to represent the streamwise and transverse vibrations of the cylinder.

$$x/D = A_x^* \sin(2\pi f_n t + \theta) \tag{4.9}$$

$$y/D = A_y^* \sin(2\pi f_n t) \tag{4.10}$$

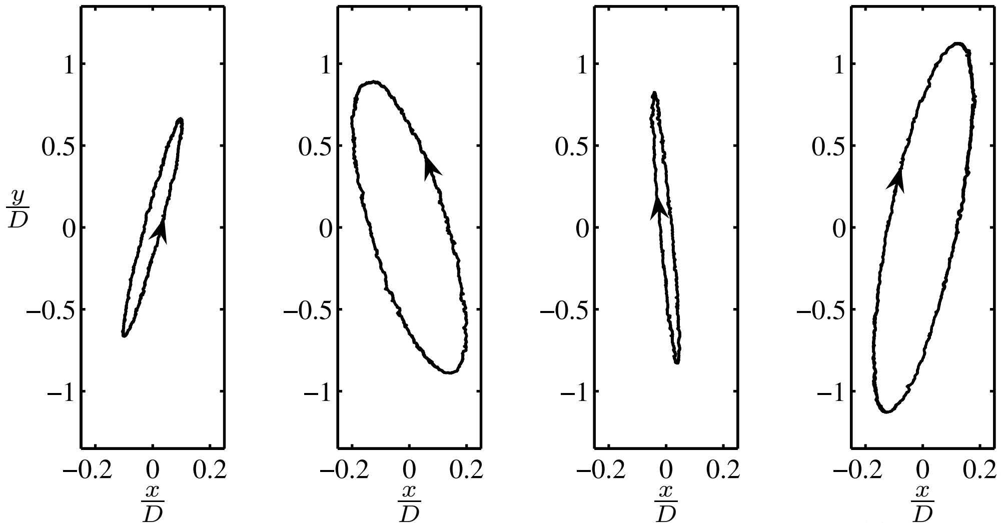

(a) $U^* = 6.62$ $U_c^* = 13.79$ $\zeta = 0.01$

(b) $U^* = 6.62$ $U_c^* = 28.8$ $\zeta = 0.0071$

(c) $U^* = 5.73$ $U_c^* = 19.76$ $\zeta = 0.0081$

(d) $U^* = 5.87$ $U_c^* = 36.69$ $\zeta = 0.0043$

Figure 4.9 Experimental elliptic cylinder tip trajectories.

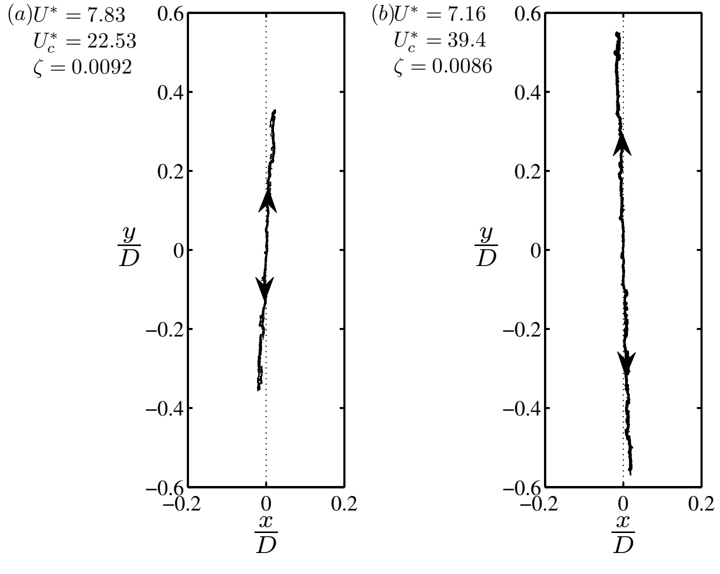

Figure 4.10 Special cases of the observed elliptic cylinder tip trajectories.

Based on Eqs. 4.9 and 4.10, Fig. 4.11 illustrates possible types of elliptic trajectories attainable for various phase angles (θ), with the selected values of A_x^* and A_y^* being comparable to those observed

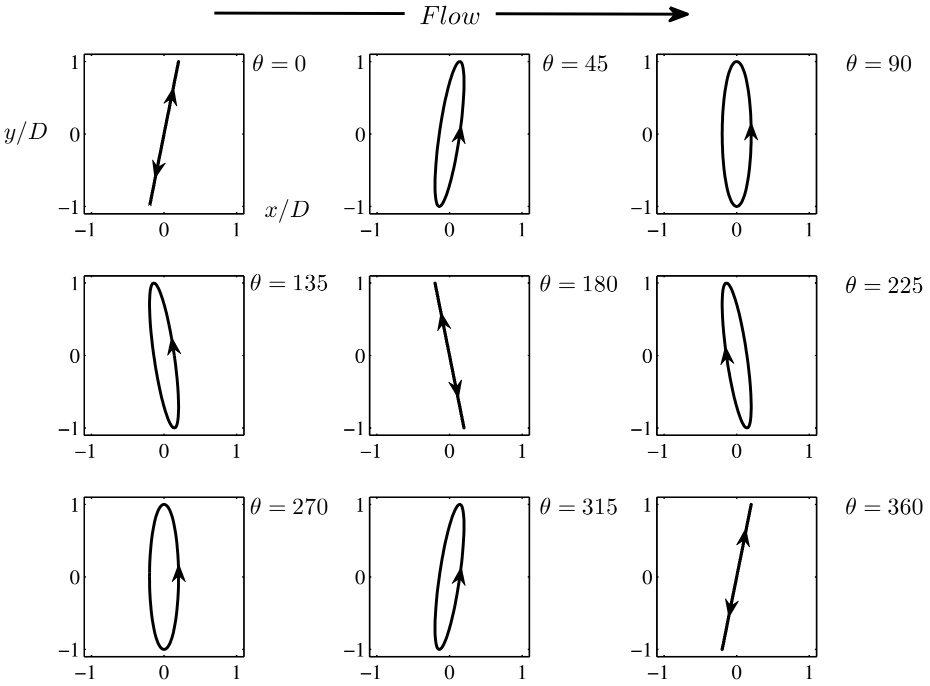

Figure 4.11 Possible cylinder tip trajectories predicted based on Eqs. 4.9 and 4.10 for $A_x^* = 0.2$ and $A_y^* = 1$.

experimentally. Comparing Fig. 4.11 with the experimentally measured trajectories in Fig. 4.9, it can be seen that the four types of elliptic trajectories presented in Figs. 4.9a, b, c, and d correspond to those predicted from Eqs. 4.9 and 4.10 for $0° < \theta < 90°$, $90° < \theta < 180°$, $180° < \theta < 270°$, and $270° < \theta < 360°$, respectively. Also, the two special cases of elliptic trajectories depicted in Figs. 4.10a and 4.10b agree with the predictions for $\theta = 0°$ (or 360°) and $\theta = 180°$, respectively. The comparison of the experimental results and the trajectories predicted from Eqs. 4.9 and 4.10 suggest that the different orientations and directions of orbiting for elliptic trajectories depend on the phase angle between the streamwise and transverse vibrations of the cylinder. However, it should be mentioned that such an effect of θ will be negligible when $A_x^*/A_y^* << 1$ because elliptic trajectories for any value of θ will be essentially line segments normal to the flow (Fig. 4.12).

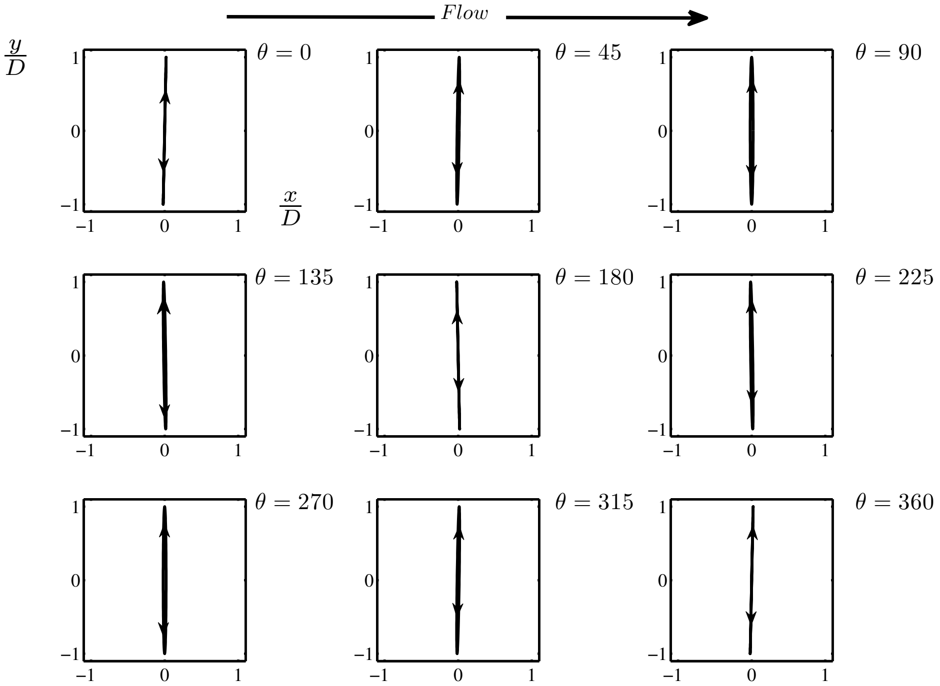

Figure 4.12 Possible cylinder tip trajectories predicted based on Eqs. 4.9 and 4.10 for $A_x^* = 0.02$ and $A_y^* = 1$.

The Hilbert transform was employed to estimate the phase angle based on experimental data. The results corresponding to the experimental trajectories shown in Fig. 4.9 and Fig. 4.10 are presented in Figs. 4.13 and 4.14, respectively. Agreeing with the predictions in Fig. 4.11, the phase angles for the trajectories shown in Figs. 4.9a, b, c, and d are θ = 18°, 135°, 229°, and 315°, respectively (Fig. 4.13). Also, in agreement with Fig. 4.11, the phase angles corresponding to the trajectories in Figs. 4.10a and b fluctuate about θ = 360° and 180° (Fig. 4.14), respectively. The higher fluctuations in θ in Fig. 4.14 are attributed to the relatively low amplitudes of streamwise vibrations observed in the corresponding trajectories in Fig. 4.14. It should be noted that, in contrast with the results shown for the synchronization region (Figs. 4.13 and 4.14), random phase angle fluctuations occur in the non-synchronized region, as depicted in Fig. 4.15. The random fluctuations in θ are associated with irregular, low amplitude transverse and streamwise vibrations of the structure in the non-synchronized region.

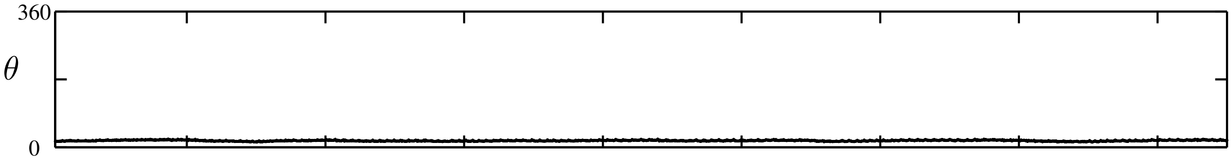

$(a) U^* = 6.62, U_c^* = 13.8, \zeta = 0.01$

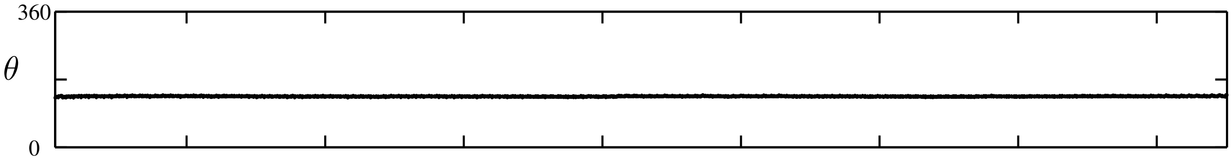

$(b) U^* = 6.62, U_c^* = 28.8, \zeta = 0.0071$

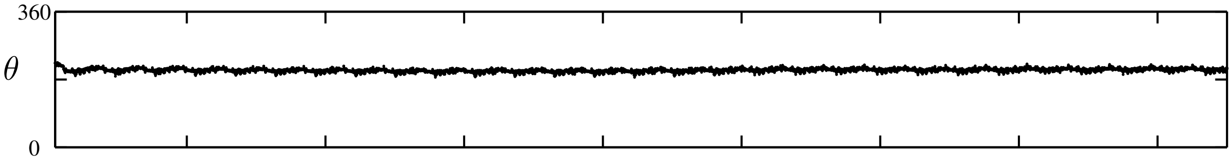

$(c) U^* = 5.73, U_c^* = 19.8, \zeta = 0.0081$

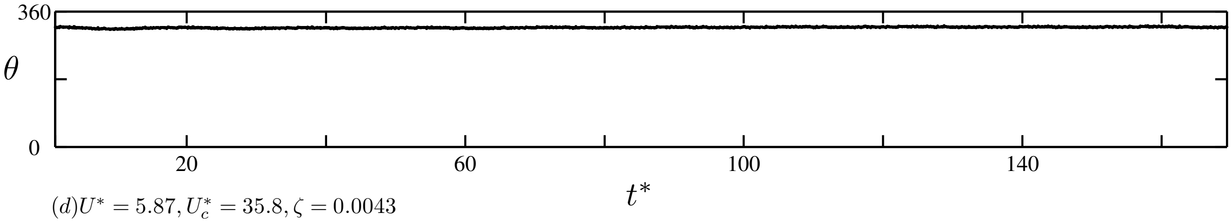

$(d) U^* = 5.87, U_c^* = 35.8, \zeta = 0.0043$

Figure 4.13 Variation of the phase with time for elliptic trajectories in the synchronization region.

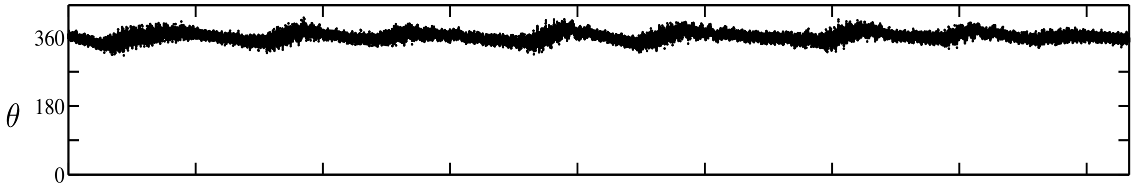

$(a) U^* = 7.83, U_c^* = 22.53, \zeta = 0.0092$

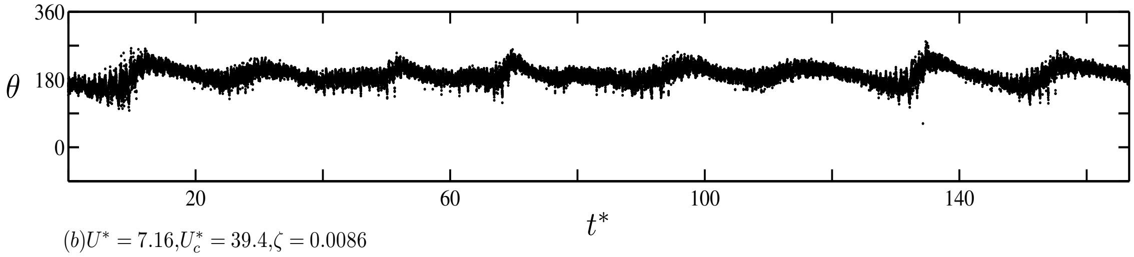

$(b) U^* = 7.16, U_c^* = 39.4, \zeta = 0.0086$

Figure 4.14 Variation of the phase with time for line segment trajectories in the synchronization region.

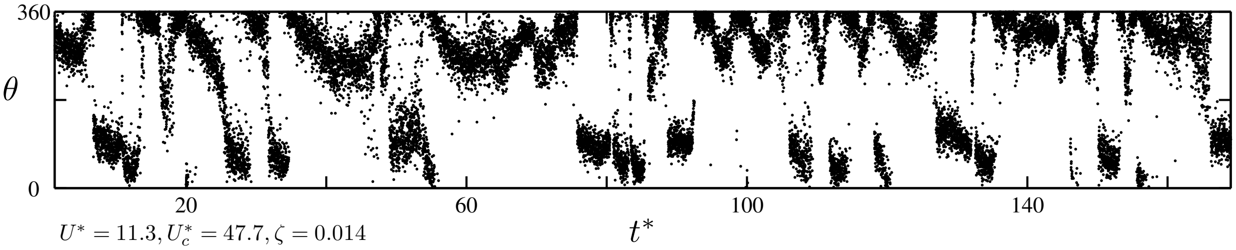

Figure 4.15 Variation of the phase with time in the non-synchronized region.

It can be inferred from the results presented in Figs. 4.13 and 4.14 that changing the experimental conditions can significantly affect θ, thereby affecting the orientation and direction of orbiting for the elliptic trajectories. Figure 4.16 shows the variation of the phase angle with reduced velocity and damping ratio, and Fig. 4.17 illustrates the effect of U_c^* on θ for all the experiments conducted in the synchronization region. Note that higher error bars associated with several data points in Figs. 4.16 and 4.17 are attributed to higher fluctuations in the phase angle estimates due to low streamwise amplitudes of vibrations observed for the corresponding experimental conditions. Examining the results in Figs. 4.16 and 4.17 suggests that the four types of elliptic trajectories are governed primarily by structural coupling (U_c^*). For example, Fig. 4.17 shows that increasing U_c^* from 16.1 to 19.8 or from 31.6 to 35.7 shifts the phase angle by about 180°, resulting in drastic changes in the orientation and the direction of orbiting motion. In contrast, despite having a measurable effect on θ, Fig. 4.16 shows that changing the reduced velocity or damping ratio does not appear to be sufficient to switch between the four types of elliptic trajectories. For example, for $28.3 < U_c^* < 31.6$, increasing the reduced velocity from 5.4 to 7.6 and damping ratio from 0.65% to 1.1% decreases the phase angle from 157° to 105°. Although the resulting change in the phase angle is about 50%, θ remains between 90° and 180°, associated with the same distinct type of elliptic trajectory. The results presented in Figs. 4.16 and 4.17 suggest that each of the four identified types of cylinder trajectories corresponds to a distinct range of U_c^*, with approximate boundaries of such ranges shown in Fig. 4.17 by vertical dashed lines.

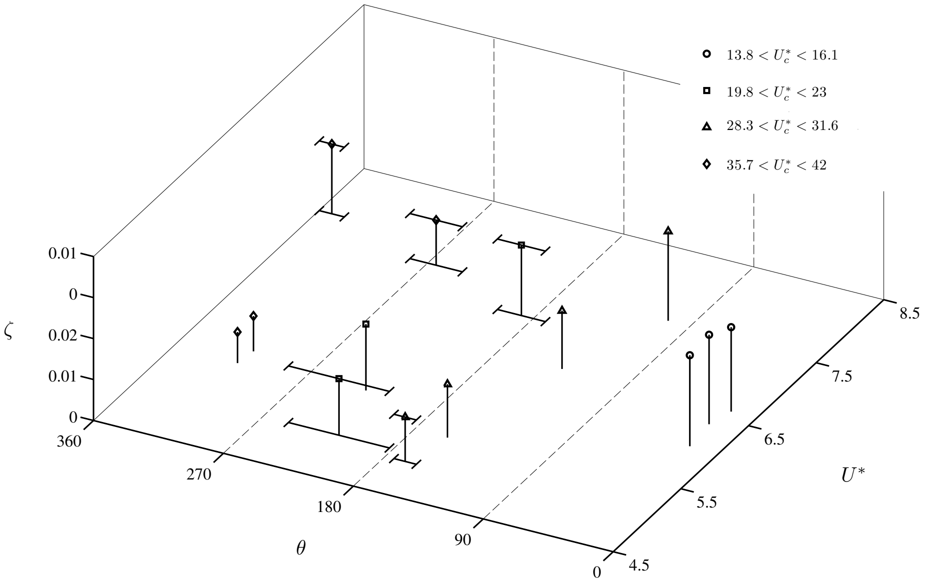

Figure 4.16 Phase angle variation with reduced velocity and damping ratio. Note that, unless shown otherwise, the uncertainty is accommodated by the size of the corresponding data legends.

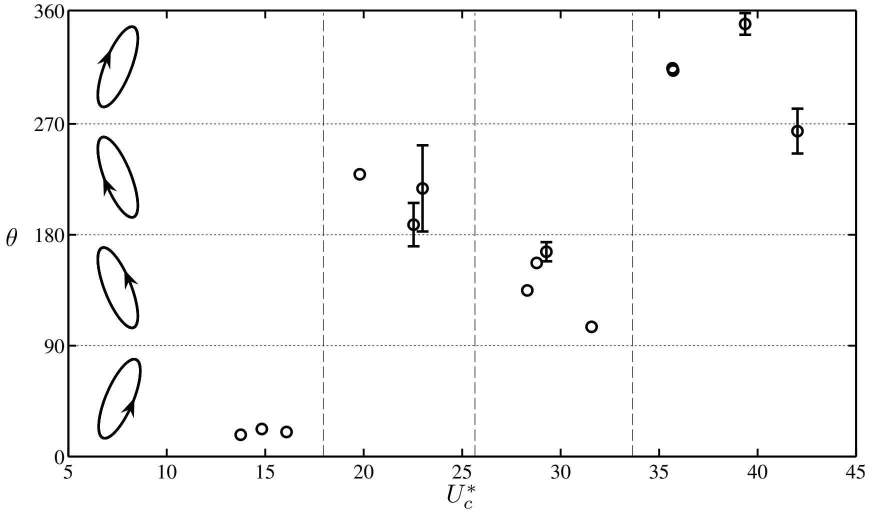

Figure 4.17 Phase angle variation with U_c^*. Note that, unless shown otherwise, the uncertainty is accommodated by the size of the corresponding data legend.

4.4 Wake vortex shedding

The forgoing discussion of the experimental results suggests that the structural response is governed by U^*, U^*_c, and ζ. Thus, these three parameters are expected to influence the wake development. In this study, the variation of the vortex pattern along the span was investigated via flow visualization. The experiments were performed at $U^* = 6.6$, i.e., in the synchronizations region, with the experimental conditions detailed in Table 4.3. The two cases investigated (A and B) correspond to two different types of elliptic trajectories, with cases A and B (Table 4.3) corresponding to Figs. 4.9b and a, respectively. For each of these two cases, flow visualization was performed at z/L = 0.65 and z/L = 0.84.

Table 4.3 Test conditions for flow visualizations.

Case		U^*	U^*_c	ζ	**z/L**	A^*_y **at z/L**
A	A1	6.6	28.8	0.007	0.65	0.32
	A2	6.6	28.8	0.007	0.84	0.15
B	B1	6.6	13.8	0.01	0.65	0.24
	B2	6.6	13.8	0.01	0.84	0.11

An analysis of flow visualization images revealed that double roll up of the shear layers occurs in the near wake. A representative image shown in Fig. 4.18 suggests that the flow topology is similar to the 2P vortex shedding pattern observed for VIV of one DOF circular cylinders, e.g., Williamson & Roshko (1988). However, the downstream development of the wake vortices was found to depend significantly on the test conditions.

Cases A1 and A2: Based on the downstream evolution of the two co-rotating vortices shed each half cycle, two distinct types of wake development for case A1 are depicted in Figs. 4.19d and 4.20. An analysis of flow visualization videos and images showed that two counter-clock-wise (CCW) vortices,

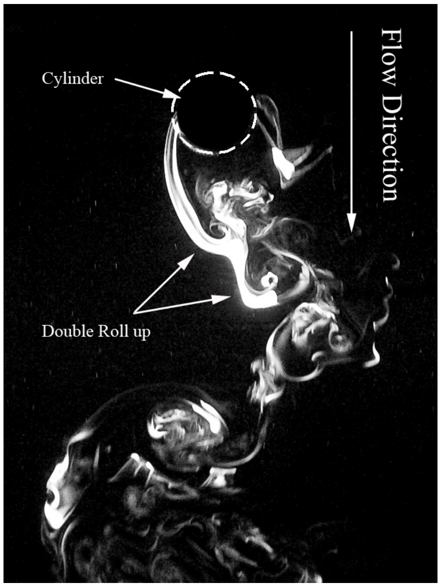

Figure 4.18. Flow visualization of the double roll up of shear layers for U^* = 6.6, z/L = 0.65, ζ = 0.007, and U_c^* = 28.8.

shed from the left hand side of the cylinder, merge within about four diameters downstream of the cylinder. The process of vortex merging is illustrated in the sequence of images shown in Figs. 4.19a-d. Adopting the terminology introduced by Cerretelli & Williamson (2003), the vortex merging process can be broken into four stages, namely, first diffusive, convective, second diffusive, and merged diffusive stages. The merged vortices identified in both Figs. 4.19c and d are representative of the last stage of vortex merging. In comparison with merging of CCW vortices, it was occasionally observed that these vortices remain separated in the near wake (Fig. 4.20). It should be noted that the clock-wise (CW) vortices shed on the right hand side of the cylinder have not been observe to merge in the near wake.

As the elevation is decreased along the span of the cylinder (case A2), the CCW as well as the CW vortices merge within about ten diameters downstream of the cylinder. Comparing the results for cases A1 and A2 (Figs. 4.19 and 4.21a), it can be seen that vortex merging occurs within a longer region at

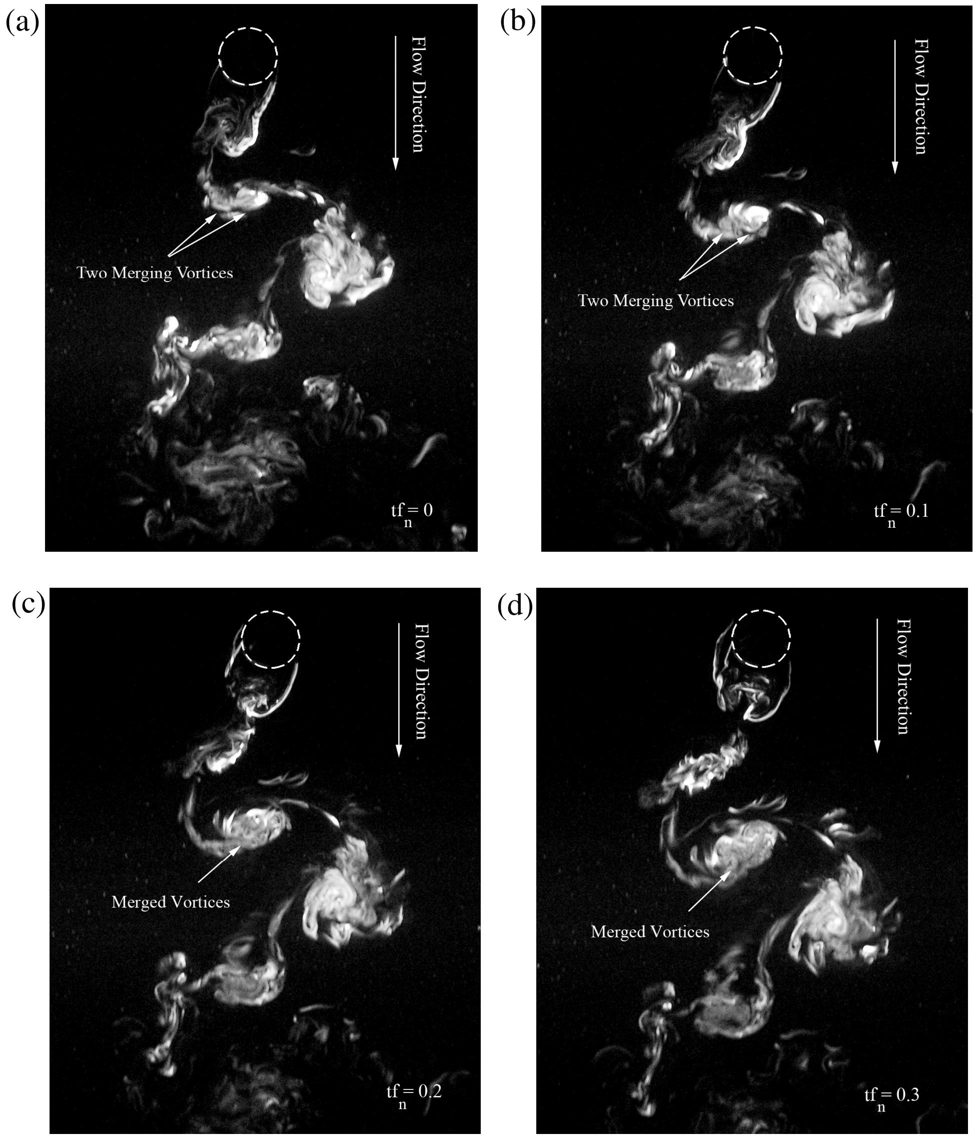

Figure 4.19 Vortex merging process for case A1, ($U^* = 6.6$, $z/L = 0.65$, $\zeta = 0.007$, and $U_c^* = 28.8$). The cylinder moves to the right in (a), (b), and (c), and reaches to an almost rest in (d).

lower elevations. For case A2, the pattern of the merged co-rotating vortices is similar to the 2S vortex shedding pattern (Fig. 4.21a).

Cases B1 and B2: At the higher elevation (case B1), a 2P vortex shedding pattern occurs (Fig. 4.22). In contrast, at the lower elevation (case B2), Fig. 4.21b, a vortex shedding pattern similar to that for case A2 (Fig. 4.21a) is observed.

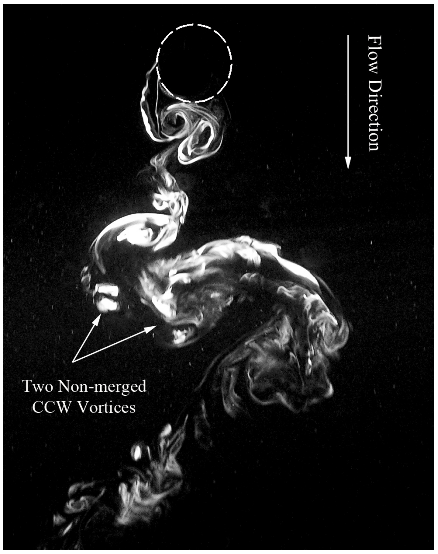

Figure 4.20 2P-like shedding pattern for case A1 (U^* = 6.6, z/L = 0.65, ζ = 0.007, and U_c^* = 28.8).

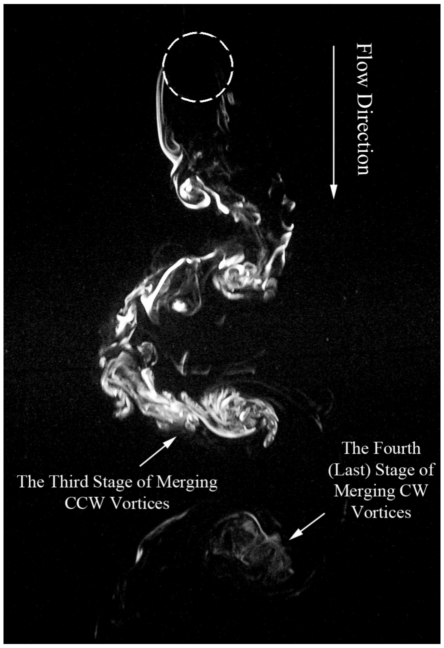

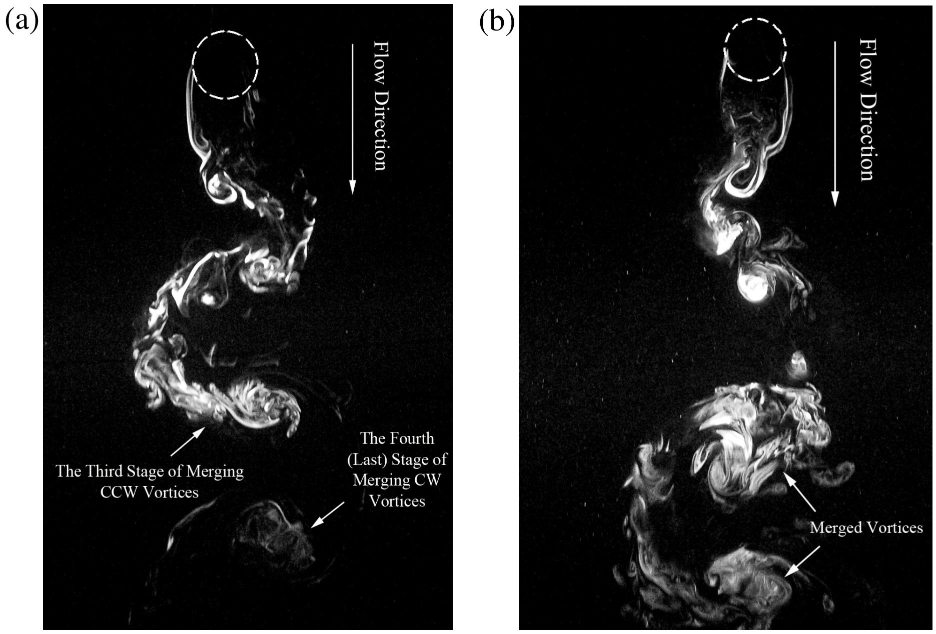

Figure 4.21 Flow visualization of: (a) case A2, (U^* = 6.6, z/L = 0.84, ζ = 0.007, and U_c^* = 28.8), and (b) case B2, (U^* = 6.6, z/L = 0.84, ζ = 0.01, and U_c^* = 13.8).

Analysis of vortex shedding patterns: Comparing the wake flow development at a constant U^* shows that changing U_c^* and ζ can affect the wake vortex shedding patterns. The shedding pattern is expected to depend primarily on the response of the structure. For example, in the case of a one DOF uniform amplitude cylinder vibrations (Morse & Williamson, 2009), varying the transverse amplitude of response can produce different shedding patterns (Fig. 4.23). Thus, the observed variation in the vortex shedding patterns between cases A1 and B1 is attributable to the associated changes in the amplitudes of response caused by the variation of U_c^* and ζ. On the other hand, the attendant change in the transverse amplitude is not sufficient to affect vortex shedding patterns at lower elevations (cases A2 and B2).

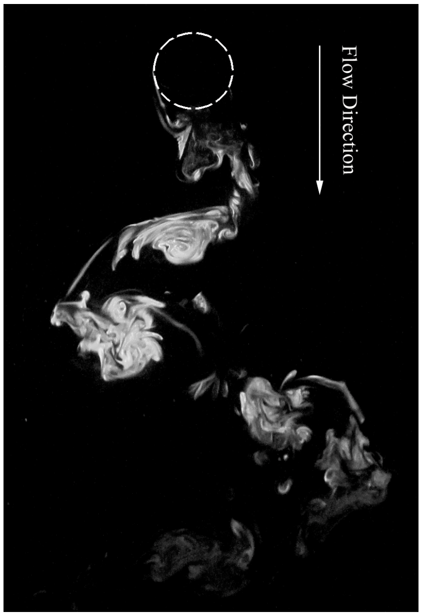

Figure 4.22 Flow visualization for case B1, (U^* = 6.6, z/L = 0.65, ζ = 0.01, and U_c^* = 13.8).

It is of interest to investigate if wake vortex shedding patterns for two DOF linear amplitude cylinder vibrations can be predicted based on the results available for one DOF cylinders. In Fig. 4.23, the current results pertaining to cases A1, A2, B1, and B2 (Table 4.3) are overlaid onto an updated Williamson- Roshko map from Morse & Williamson (2009). The map predicts a 2P vortex shedding pattern for cases A1 and B1. Indeed, the double roll up of the separated shear layer was observed for these cases. However, unlike 2P shedding seen in the near wake for case B1 (Fig. 4.22), flow visualization shows frequent merging of CCW vortices for case A1 (Fig. 4.19). For the lower elevation, the map predicts an intermittent switching between the 2P and "non- synchronized" pattern for case A2 and the non-synchronized pattern for case B2. In contrast, for both cases, flow visualization reveals a transition from 2P to 2S vortex shedding pattern. The foregoing comparison suggests that the results pertaining to one DOF uniform amplitude VIV should not, in general, be extrapolated to the cases of two DOF linear amplitude VIV. A similar conclusion can be reached based on the results of Leong & Wei (2008).

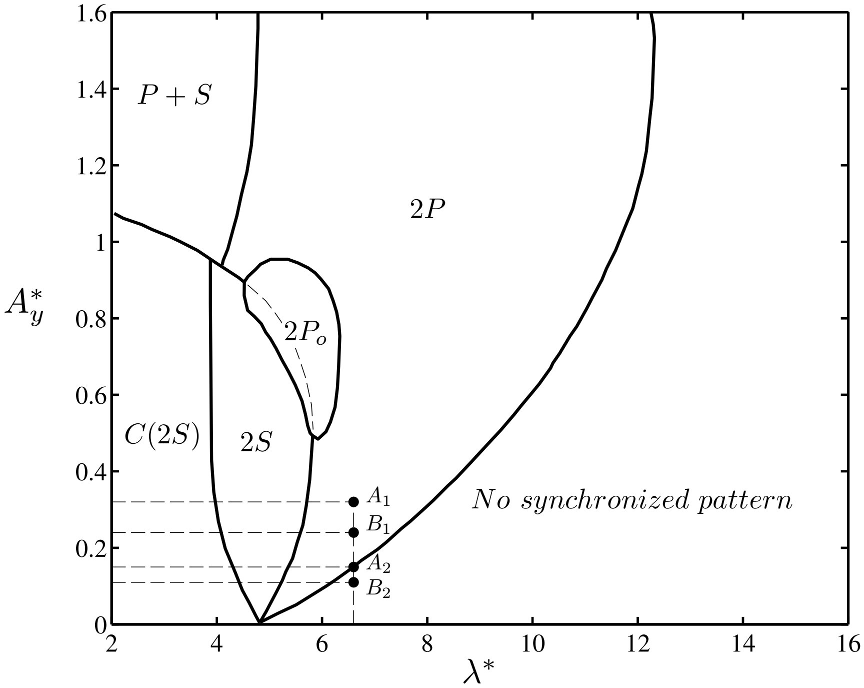

Figure 4.23 Comparison of cases A and B with the results of Morse & Williamson (2009). Note that λ^* = U^* in the synchronization region.

The present results show that the vortex shedding pattern can change along the span of the cylinder. Therefore, vortex dislocations, accompanied by complex vortex connections, are expected to occur along the span. Moreover, a simultaneous occurrence of synchronized and non-synchronized vortex shedding patterns at two different elevations, such as that predicted by the map in Fig. 4.23 for cases B1 and B2, is not possible since vortex lines cannot terminate in the fluid. Thus, at a given Reynolds number, a new, multidimensional map needs to be composed to predict vortex shedding patterns along the span of a cylindrical structure undergoing two DOF variable amplitude VIV.

5 Effect of tuned mass damper on vortex-induced vibrations

In this chapter a simplified mathematical model is introduced to investigate the influence of various parameters on the response of a one DOF structure equipped with a one DOF TMD. Then, experimental results characterizing the effect of a two DOF tuned-mass damper on vortex-induced vibrations of a two DOF pivoted circular cylinder are presented.

5.1 Parametric study of a one DOF structure equipped with a one DOF TMD

Figure 5.1 shows schematically one DOF structure equipped with a one DOF TMD. The motion of the system shown in Fig. 5.1 is governed by Eqs. 5.1 and 5.2.

$$M\ddot{X}_M(t) + C\dot{X}_M(t) - c[\dot{X}_{TMD}(t) - \dot{X}_M(t)] + KX_M(t) - k[X_{TMD}(t) - X_M(t)] = F(t) \tag{5.1}$$

$$m_{TMD}\ddot{X}_{TMD}(t) + c[\dot{X}_{TMD}(t) - \dot{X}_M(t)] + k[X_{TMD}(t) - X_M(t)] = 0 \tag{5.2}$$

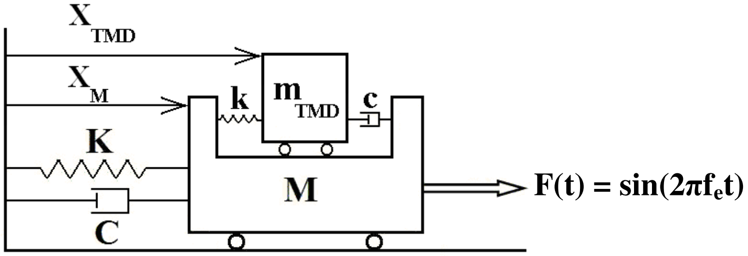

Figure 5.1 Schematic of a one DOF main structure equipped with a one DOF TMD.

The forcing was selected to be harmonic as it represents the forcing in the case of vortex-induced vibrations. Effects of tuning frequency ratio ($f_r^* = f_{TMD} / f_n$), forcing frequency ratio ($f_e^* = f_e / f_n$), TMD mass ratio (μ), and TMD damping ratio (ζ_{TMD}) on normalized amplitudes and frequencies of vibrations of the main structure were investigated by solving Eqs. 5.1 and 5.2 numerically. The investigated ranges of governing parameters are presented in Table 5.1. These values were selected to approximate experimental conditions.

Table 5.1 Governing non-dimensional parameters investigated in the parametric study.

Parameters	Value
$1/f_r^*$	0 - 1.6
f_e^*	0.4 - 1.8
μ	0.02 - 0.15
ζ_{TMD}	0 - 1
ζ	0.01

5.1.1 Amplitude of response

Normalized amplitude of vibrations (A^*) is defined as the ratio of the amplitude of vibrations of the main structure to the static displacement of the structure subjected to a constant force of 1 N. Den Hartog (1956) solved Eqs. 5.1 and 5.2 and showed that the normalized amplitude of vibrations is given by Eq. 5.3.

$$A^* = \sqrt{\frac{\left(1-\frac{f_e^*}{f_r^{*2}}\right)^2 + 4\left(\zeta_{TMD}\frac{f_e^*}{f_r^*}\right)^2}{\left[\frac{f_e^{*2}}{f_r^{*2}}\left(\frac{f_e^{*2}}{1+\mu}-1\right)-f_e^{*2}-4\frac{\zeta\zeta_{TMD}f_e^{*2}}{f_r^*\sqrt{1+\mu}}+1\right]^2+\left[2\frac{\zeta f_e^{*3}}{f_r^*(1+\mu)}+2\zeta_{TMD}\frac{f_e^{*3}}{f_r^*}-2\zeta_{TMD}\frac{f_e^*}{f_r^*}-2\frac{\zeta f_e^*}{\sqrt{1+\mu}}\right]^2}} \quad (5.3)$$

Figure 5.2 illustrates the effect of $1/f_r^*$ and ζ_{TMD} on the amplitudes of vibrations for the lock-in condition, i.e., f_e^* = 1, and the TMD mass ratio (μ) of 0.087, matching that in the experiments. TMD damping ratios are selected to be 0, 0.1, 0.24, and 0.5, where ζ_{TMD} = 0.24 corresponds to the TMD damping ratio tested in the experiments. The results indicate that both $1/f_r^*$ and ζ_{TMD} significantly affect the normalized amplitude of vibrations. The maximum amplitude of vibrations occurs for $\zeta_{TMD} = 0$, and at $1/f_r^* = 0.23$. Increasing the TMD damping ratio decreases the maximum normalized amplitudes of vibrations and reduces $1/f_r^*$ at which it occurs. For example, increasing ζ_{TMD} from 0 to 0.5 decreases the maximum of the normalized amplitude from 61 to 58 and the associated values of $1/f_r^*$ from 0.23 to 0.19. The results indicate that increasing the TMD damping ratio increases the minimum A^* and the corresponding $1/f_r^*$. For example, increasing ζ_{TMD} from 0 to 0.5 increases the minimum A^* from 0 to 9.2 and the associated values of $1/f_r^*$ from 1 to 1.3.

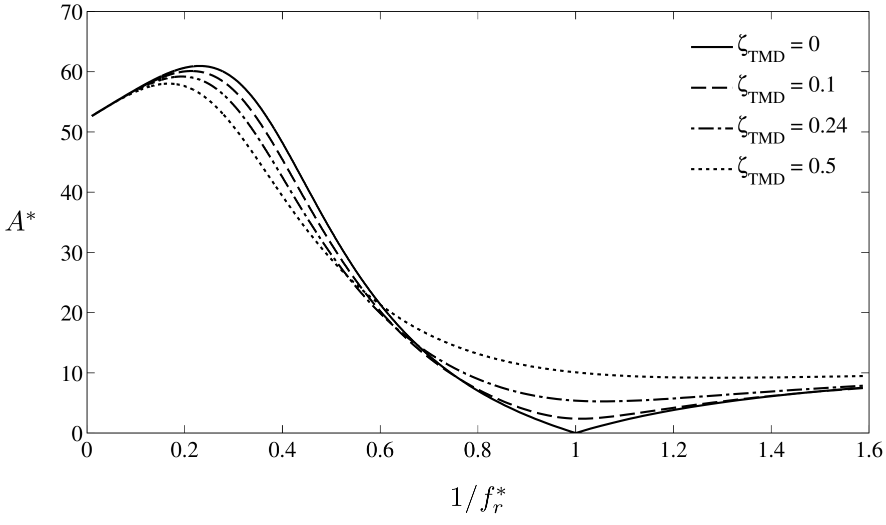

Figure 5.2 Normalized amplitudes of vibrations at $f_e^* = 1$, $\mu = 0.087$, and $\zeta = 0.01$.

Figure 5.3 illustrates the effect of mass ratio on the normalized amplitude of vibrations at $f_e^* = 1$ and $\zeta_{TMD} = 0$. The figure indicates that, for $1/f_r^* \geq 0.23$, increasing the TMD mass ratio decreases the normalized amplitude of vibrations. The results show that, for all mass ratios, A^* is minimized at $1/f_r^*$ = 1. Also, there exists a range of $1/f_r^*$ for which the normalized amplitudes of vibrations are less than the static displacement of the structure, i.e., $A^* < 1$. This range of $1/f_r^*$ broadens with increasing TMD mass ratio. For example, increasing μ from 0.02 to 0.15 broadens the range from $0.99 < 1/f_r^* < 1.01$ to $0.94 < 1/f_r^* < 1.06$.

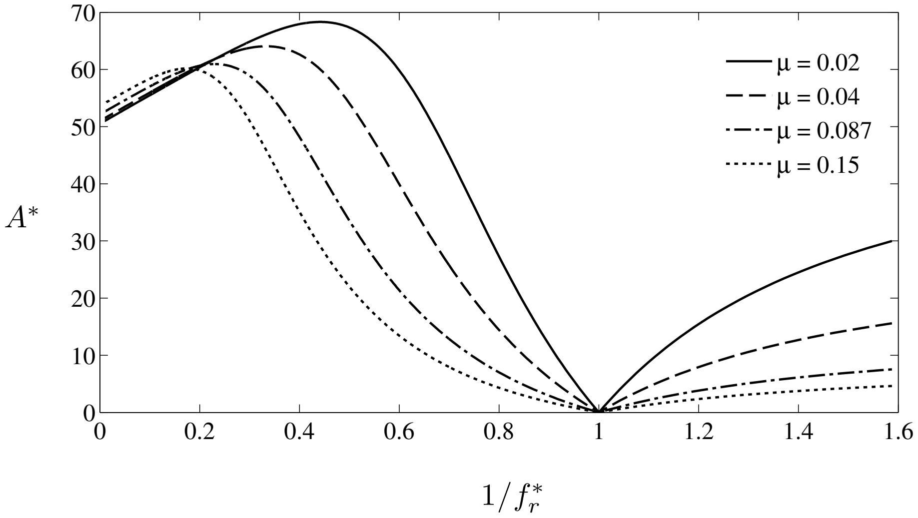

Figure 5.3 Normalized amplitudes of vibrations at f_e^* = 1, ζ_{TMD} = 0, and ζ = 0.01.

Figure 5.4 shows the variation of A^* with f_e^* and ζ_{TMD} for the tuned condition, i.e., $1/f_r^* = 1$, at μ = 0.087. The results indicate that A^* increases substantially when the forcing frequency locks onto $0.88f_n$ or $1.18f_n$. Moreover, the results show that the amplitude of vibrations decreases to below the static displacement of the structure for the following conditions: (i) $f_e^* \geq 1.53$ and $0 < \zeta_{TMD} \leq 1$, and (ii) $0.97 \leq f_e^* \leq 1.04$ and $0 < \zeta_{TMD} \leq 0.04$.

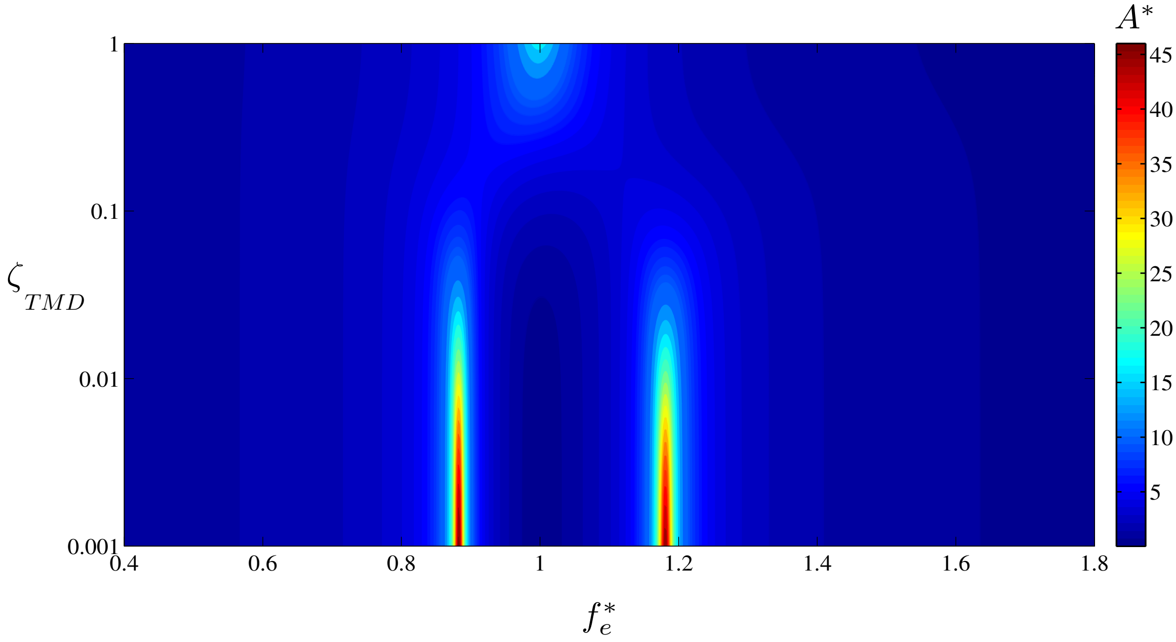

Figure 5.4 Normalized amplitudes of vibrations at $1/f_r^* = 1$, $\mu = 0.087$, and $\zeta = 0.01$.

Figure 5.5 shows the variation of A^* with f_e^* and μ at $1/f_r^* = 1$ and $\zeta_{TMD} = 0$. Similar to Fig. 5.4, the results presented in Fig. 5.5 show two branches of high normalized amplitudes of vibrations. For the mass ratio investigated experimentally, i.e., $\mu = 0.087$, the highest normalized amplitudes of vibrations occur at two critical forcing frequency ratios of $f_e^* = 0.88$, and 1.18. The figure shows that increasing the mass ratio decreases the lower critical forcing frequency ratio and increases the higher critical forcing frequency ratio. Also, the results indicate that, at any mass ratio, lower amplitudes of vibrations ($A^* < 1$) are observed for two ranges of forcing frequency ratios. For example, for $\mu = 0.087$, the amplitudes of vibrations are less than the static displacement of the structure for $f_e^* \geq 1.53$ and $0.97 \leq f_e^* \leq 1.04$. The results indicate that increasing the mass ratio narrows the first range and broadens the second range of forcing frequencies.

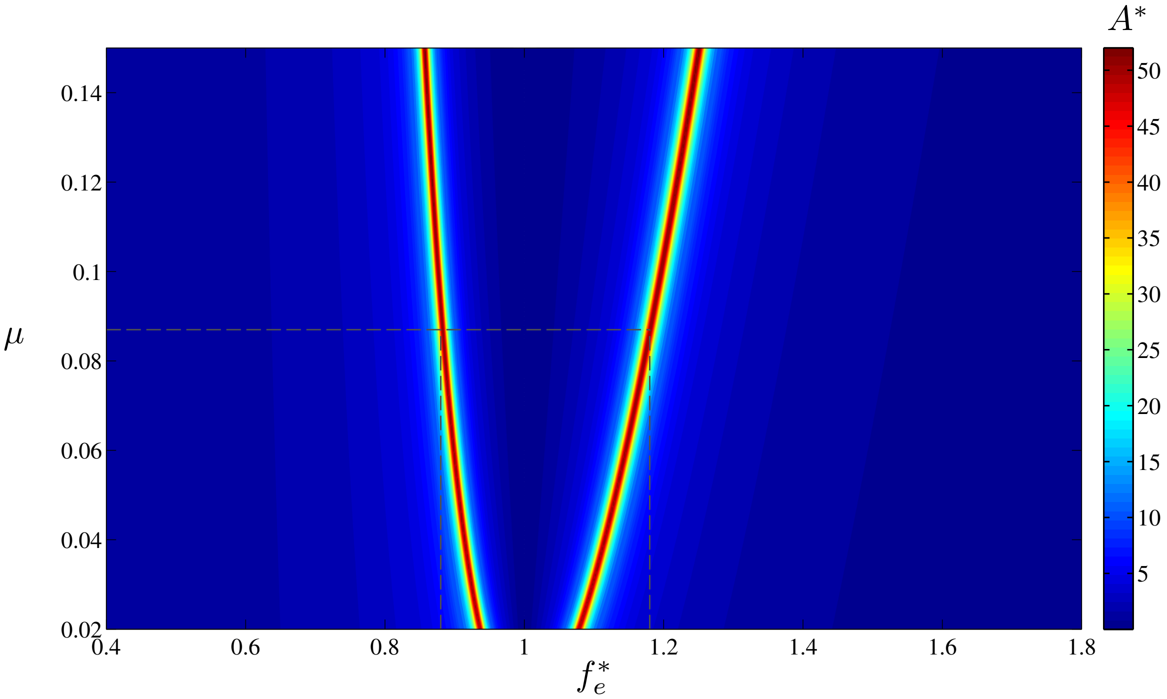

Figure 5.5 Normalized amplitudes of vibrations at $1/f_r^* = 1$, $\zeta_{TMD} = 0$, and $\zeta = 0.01$.

It can be concluded from the results presented in Figs. 5.2 to 5.5 that, when the forcing frequency matches the natural frequency and the TMD natural frequency is tuned to the main structure natural frequency ($1/f_r^* = 1$), decreasing ζ_{TMD} and/or increasing μ decreases the normalized amplitude of vibrations. However, relatively high amplitudes of vibrations can occur for two narrow bands of forcing frequencies, one centered at a frequency lower than f_n and another centered at a frequency higher than f_n. The results show that the central frequencies of these frequency bands are independent of ζ_{TMD} and depend strongly on μ. Increasing the TMD mass ratio decreases the central frequency of the first band and increases that of the second band.

5.1.2 Frequency of response

The mathematical model given by Eqs. 5.1 and 5.2 was used to investigate the frequency response of the main structure. All parametric investigations were conducted for $\mu = 0.087$ and $\zeta_{TMD} = 0$ and 0.24. The selected parameters correspond to those in experimental tests.

Figure 5.6 shows the variation of the normalized frequency of vibrations (f_y^*) of the main structure with $1/f_r^*$ for the lock-in condition ($f_e^* = 1$) and $\zeta_{TMD} = 0.24$. The results show that the dominant frequency of vibrations does not depend on $1/f_r^*$ and locks onto the natural frequency of the structure. However, for $\zeta_{TMD} = 0$ (Fig. 5.7) three distinct types of frequency response can be identified, as depicted in Figs. 5.7b-d by spectra corresponding to $1/f_r^* = 0.6$, 1, and, 1.3. For $0 < 1/f_r^* < 0.88$, the spectra of vibrations of the structure feature two peaks centered at f_n ($f_y^* = 1$), and a higher frequency labeled f_2 (Fig. 5.7b). For $0.88 \leq 1/f_r^* \leq 1.02$, the spectra of vibrations feature three peaks centered at f_n, f_2, and a frequency lower than f_n, labeled f_1 (Fig. 5.7c). Finally, for $1.02 < 1/f_r^* \leq 1.6$, the spectra of vibrations feature two dominant peaks, one peak centered at f_n and the other at f_1 (Fig. 5.7d). Analysis of the results indicates that for the first and second types of frequency response, increasing $1/f_r^*$ decreases $f_2^* = f_2/f_n$. For example, increasing $1/f_r^*$ from 0 to 1.02 decreases f_2^* from 7 to 1.18. Similarly, for the second and third types of frequency response, increasing $1/f_r^*$ decreases $f_1^* = f_1/f_n$. For example, increasing $1/f_r^*$ from 1.02 to 1.6 decreases f_1^* from 0.93 to 0.61 (Fig. 5.7a).

Figure 5.8 shows the variation of the normalized frequency of vibrations of the main structure with f_e^* for the tuned condition and $\zeta_{TMD} = 0.24$. The results indicate that the dominant frequency of vibrations matches excitation frequency (f_e^*). However, for $\zeta_{TMD} = 0$, the results presented in Fig. 5.9a indicate that the spectra of vibration feature three peaks centered at f_e^*, f_1^*, and f_2^*. Analyzing the results,

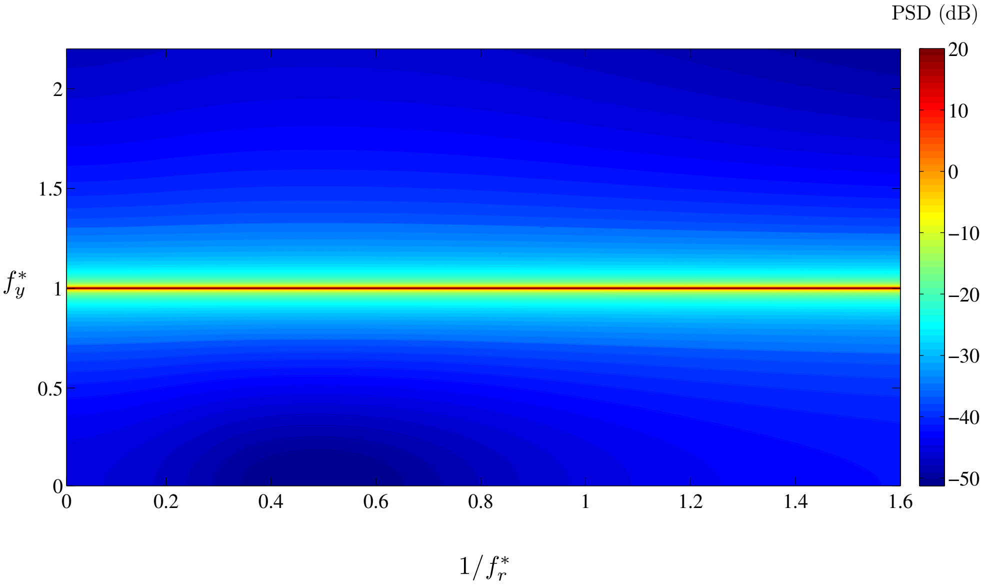

Figure 5.6 Normalized frequencies of vibrations at $f_e^* = 1$, $\zeta_{TMD} = 0.24$, $\mu = 0.087$, and $\zeta = 0.01$.

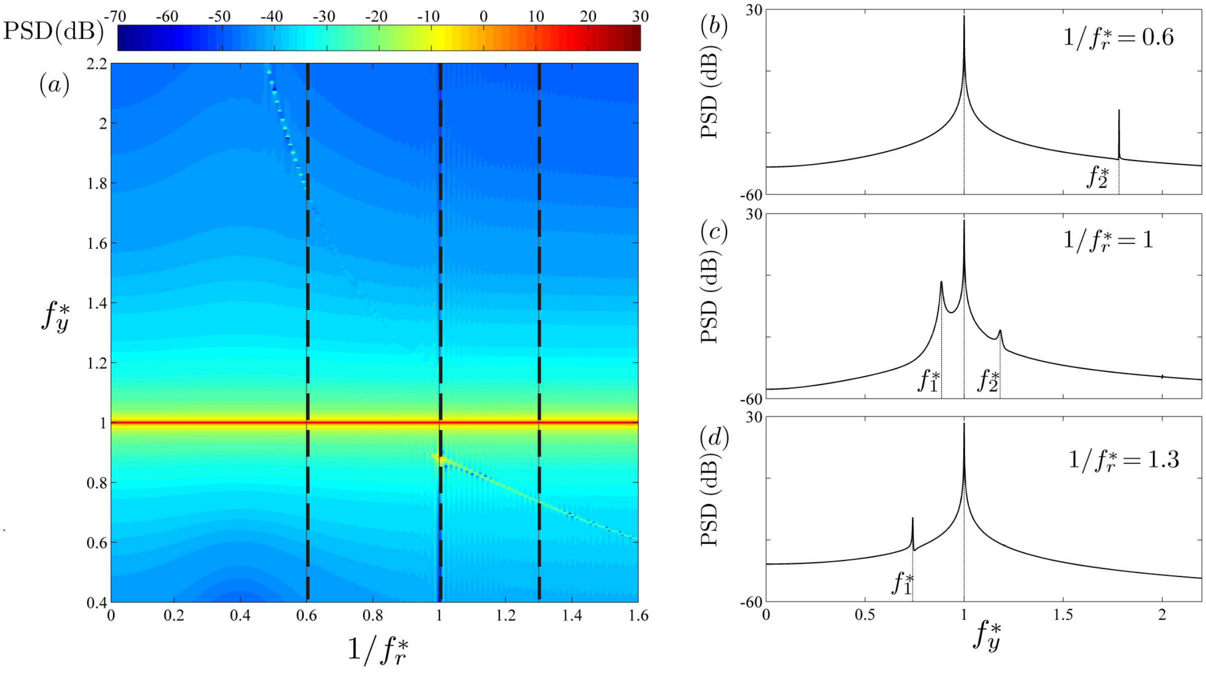

Figure 5.7 Normalized frequencies of vibrations at $f_e^* = 1$, $\zeta_{TMD} = 0$, $\mu = 0.087$, and $\zeta = 0.01$.

it can be seen that the values of f_1^* and f_2^* are independent of the excitation frequency and equal with f_1^* = 0.88 and f_2^* = 1.18, respectively.

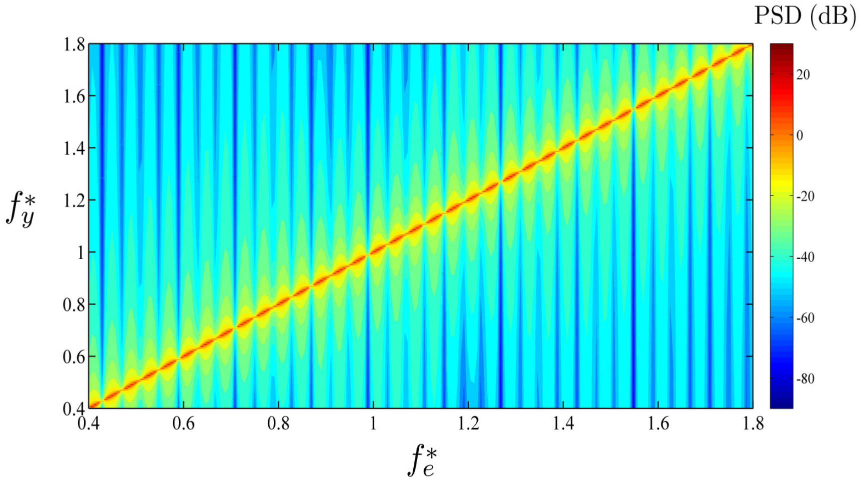

Figure 5.8 Normalized frequencies of vibrations at $1/f_r^*$ = 1, ζ_{TMD} = 0.24, μ = 0.087, and ζ = 0.01.

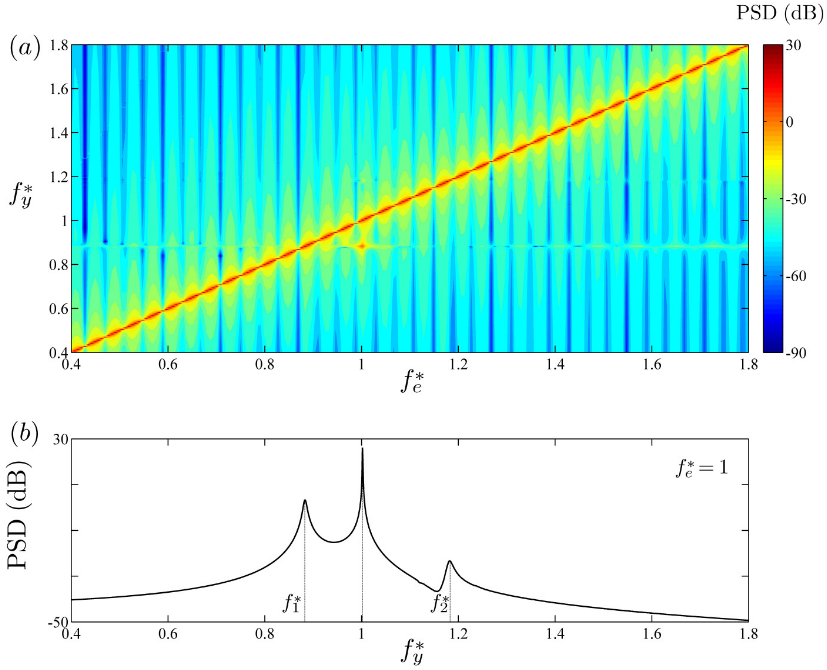

Figure 5.9 Normalized frequencies of vibrations at $1/f_r^*$ = 1, ζ_{TMD} = 0, μ = 0.087, and ζ = 0.01.

It can be concluded from the results presented in Figs. 5.6 to 5.9 that, for a relatively high TMD damping ratio of ζ_{TMD} = 0.24, the spectra of vibrations feature one dominant peak centered at the excitation frequency (f_e). In contrast, for ζ_{TMD} = 0, the frequency response is characterized by three frequencies, namely, excitation frequency, a frequency higher than f_n (f_1), and a frequency lower than f_n (f_2). The results indicate that values of both f_1 and f_2 depend strongly on $1/f_r^*$ and are independent of f_e^*.

5.2 Experimental testing of a two DOF tuned-mass damper on a two DOF pivoted circular cylinder undergoing VIV

The results presented in Chapter 4 show that a pivoted cylindrical structure may undergo relatively large amplitudes of vortex-induced vibrations ($A_y^* \approx 1$) in the synchronization region. One of the objectives of the present study is to investigate the effectiveness of a novel adaptive pendulum tuned-mass damper, i.e., introduced in Chapter 3, in mitigating such vibrations. The effect of the TMD on the response of the pivoted cylinder undergoing VIV was investigated experimentally and results are presented in this section.

Dimensional analysis can be employed to show that the amplitudes and frequencies of vibrations of the cylinder equipped with the TMD are dependent on Re, I^*, m^*, AR, Fr, μ, U^*, U_c^*, ζ, $1/f_r^*$, and ζ_{TMD}. Throughout the experiments, the Reynolds number (Re), moment of inertia ratio (I^*), mass ratio (m^*), aspect ratio (AR), Froude number (Fr), and TMD mass ratio (μ) were kept constant. The experiments were performed for two TMD damping ratios, ζ_{TMD} = 0.24 and $\zeta_{TMD} \approx 0$. For ζ_{TMD} = 0.24, the dampers were attached to the pendulum; whereas for ζ_{TMD} = 0, no dampers were utilized. The tests were conducted at three reduced velocities in the synchronization region (U^* = 5.44, 6, and 6.48, corresponding to f_n = 0.53, 0.57, and 0.63 Hz) and one reduced velocity in the non-synchronized region (U^* = 4.18, corresponding to f_n = 0.82 Hz). Changing the length of the pendulum, TMD natural frequency (f_{TMD}) was varied, allowing to investigate the range of $1/f_r^*$ from 0 to 1.59, where $1/f_r^* = 0$ corresponds to the case of restrained pendulum. All relevant non-dimensional parameters are summarized in Table 5.2.

Table 5.2 Governing non-dimensional parameters investigated in the experiments.

parameter	**Value**				
Re	2100				
I^*	188.9				
m^*	19.9				
AR	64.6				
Fr	0.17				
μ	0.087				
ζ_{TMD}	0.24				0
U^*	4.18	5.44	6	6.48	6
ζ	0.018	0.055	0.01	0.004	0.01
U_c^*	21.6	53.5	19.9	51.9	19.9
$1/f_r^*$	0-1.6	0-1.21	0-1.1	0-1	0-1.1

5.2.1 Amplitude of response

Figures 5.10a and b show the variation of the normalized transverse and streamwise amplitudes of vibrations, respectively, with the reduced velocity. The results are presented for two conditions: (i) $1/f_r^* = 0$, i.e., the restrained pendulum case, and (ii) $1/f_r^* = 1$, i.e., the pendulum tuned to the natural frequency of the structure. Within the synchronization region, i.e., $U^* = 5.44$, 6, and 6.48, the results show that activating the TMD tuned to the natural frequency of the structure reduces significantly the normalized transverse and streamwise amplitudes of vibrations. Specifically, the transverse vibrations are reduced by a factor of 10 and streamwise vibrations are reduced by a factor of 3. In contrast, the results show that the TMD has a negligible effect on both A_y^* and A_x^*, in the non-synchronized region, where vibrations of the structure are insignificant.

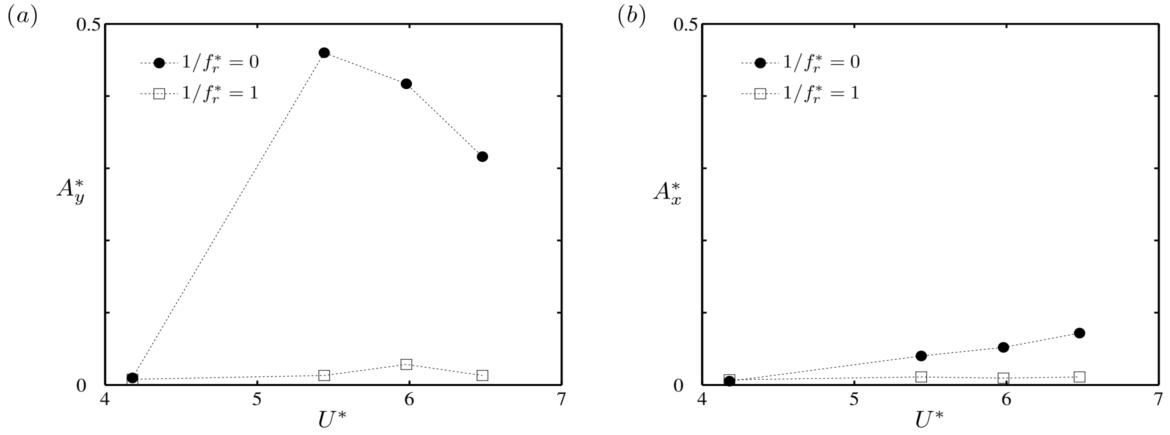

Figure 5.10 Normalized transverse and streamwise amplitudes of vibrations for restrained pendulum ($1/f_r^*$ = 0) and pendulum natural frequency tuned to the natural frequency of the structure ($1/f_r^*$ = 1).

Figure 5.11 shows the variation of the normalized transverse and streamwise amplitudes of vibrations with $1/f_r^*$. The experiments were conducted by increasing and decreasing $1/f_r^*$ over the investigated range. With dampers attached to the pendulum (ζ_{TMD} = 0.24), the results presented in Figs. 5.11a-h indicate that the lowest amplitudes of vibrations occur for $0.71 < 1/f_r^* < 1.1$. The results show that, for this range, variations in A_y^* and A_x^* are less than the experimental uncertainty, as seen in the enlarged plots shown for Figs. 5.11g and h. With dampers detached (ζ_{TMD} = 0), the results in Figs. 5.11i and j show that the effectiveness of the TMD is more sensitive to $1/f_r^*$ which is more pronounced for the normalized transverse amplitudes (Fig. 5.11i). The results presented in Fig. 5.11i indicate that, for 0.71 ≤ $1/f_r^* \leq 1$, increasing $1/f_r^*$ decreases A_y^*. Also, the results show that for this range, hysteresis exists, i.e., the results are sensitive to how $1/f_r^*$ was varied in the experiments (increased or decreased).

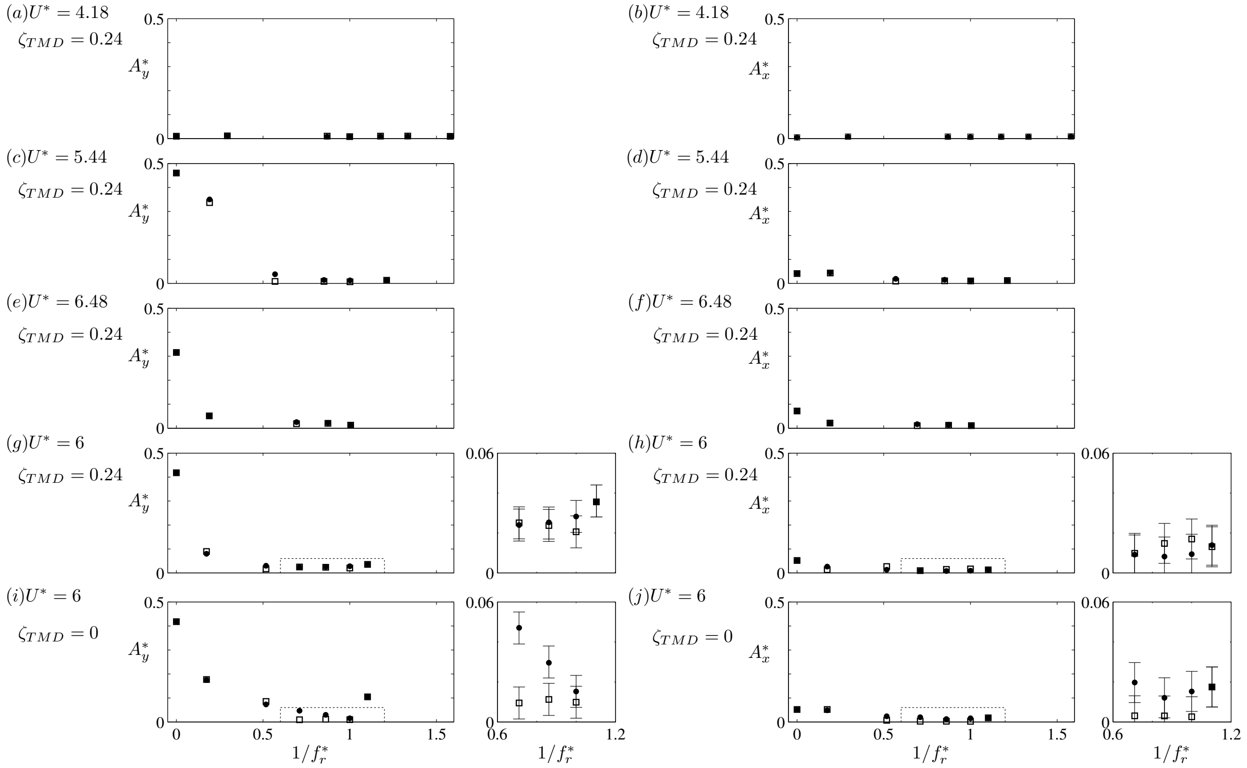

Figure 5.11 Normalized amplitudes of vibrations, ●-increasing, $1/f_r^*$ and -decreasing $1/f_r^*$.

Comparing the experimental results presented in Figs. 5.11g and i with those from simplified model presented in Fig. 5.2, it can be seen that the trends identified using the simplified model agree with those observed in experimental results. For example, both experimental and mathematical modeling results indicate that relatively low amplitudes of vibrations occur when $1/f_r^* \approx 1$, i.e., when pendulum is tuned to the natural frequency of the structure; whereas, detuning the TMD can significantly increase normalized amplitudes of vibrations. The adverse effect of detuning is more pronounced at lower damping ratios of the pendulum.

Figures 5.12a and b depict normalized transverse vibrations of the structure for $0 \leq 1/f_r^* \leq 1.1$ and for $\zeta_{TMD} = 0.24$ and 0, respectively. For each value of $1/f_r^*$ tested in the experiments, approximately fifty cycles of oscillations are shown to illustrate transverse vibrations observed in the experiments. Quasi-steady vibrations for each value of $1/f_r^*$ are shown for two cases: (i) when the corresponding conditions were set by increasing $1/f_r^*$ and (ii) by decreasing $1/f_r^*$. The results show that modulations of vibration amplitude may occur, which can be readily observed in the enlarged plots for $1/f_r^* = 0.9$. For $\zeta_{TMD} = 0.24$, these modulations are more pronounced when the natural frequency of the pendulum is set by incrementally decreasing $1/f_r^*$ (Fig. 5.12a). However, for $\zeta_{TMD} = 0$, the modulations are more pronounced when $1/f_r^*$ was set via incremental increases.

5.2.2 Frequency of response

Results presented in this section are grouped into two subsections. In the first subsection, experimental results of frequencies of transverse vibrations are presented, and in the second subsection, experimental results of the frequencies of streamwise vibrations are presented.

Frequency of transverse vibrations

Spectral analysis of the transverse vibrations showed that, when the dampers are attached to the pendulum, f_y locks onto f_n and the harmonics of f_n. However, when the dampers are detached from the pendulum, the frequency of transverse vibrations can vary significantly. Figure 5.13 shows the variation of f_y^* with $1/f_r^*$ for $U^* = 6$ and $\zeta_{TMD} = 0.24$. The results presented in the figure are similar to the results of

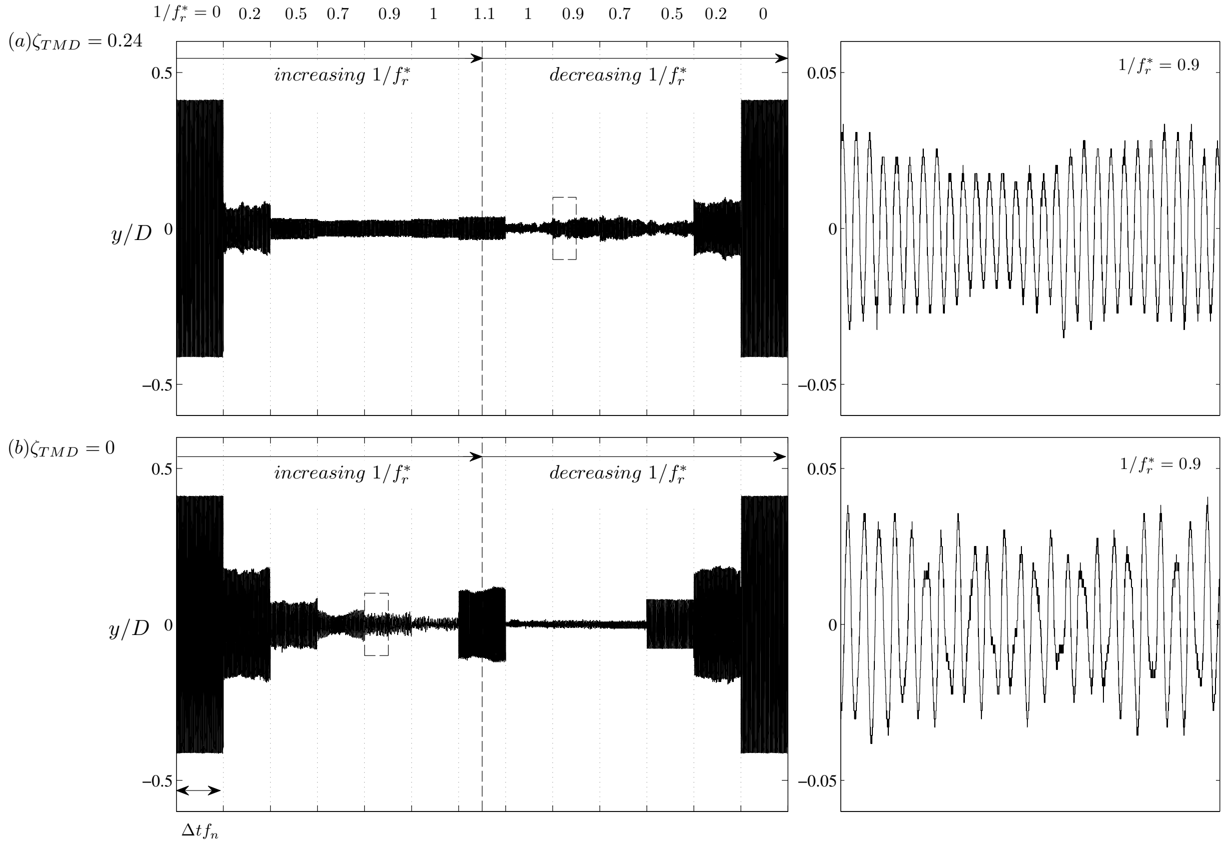

Figure 5.12 Normalized transverse vibrations for (a) $\zeta_{TMD} = 0.24$ and (b) $\zeta_{TMD} = 0$.

the simplified mathematical model presented in Fig. 5.6, which predicts that the frequency of vibrations of the structure locks onto f_n. However, in comparison with the experimental results, the results of the simplified mathematical model did not show the presence of the harmonics of the natural frequency of the structure.

Figure 5.14 shows the variation of the normalized frequency of transverse vibrations with $1/f_r^*$ for $U^* = 6$ and $\zeta_{TMD} = 0$. The results indicate that f_y locks onto f_n and harmonics of f_n for $1/f_r^* < 0.5$. However, for $1/f_r^* > 0.5$, spectra of transverse vibrations feature multiple peaks centered at a frequency lower than f_n, referred to as f_1, a frequency higher than f_n, referred to as f_2, and harmonics of f_1 and f_2. Note that the harmonics of f_n, f_1, and f_2 are not shown in Fig. 5.14 for clarity. The results show that both f_1

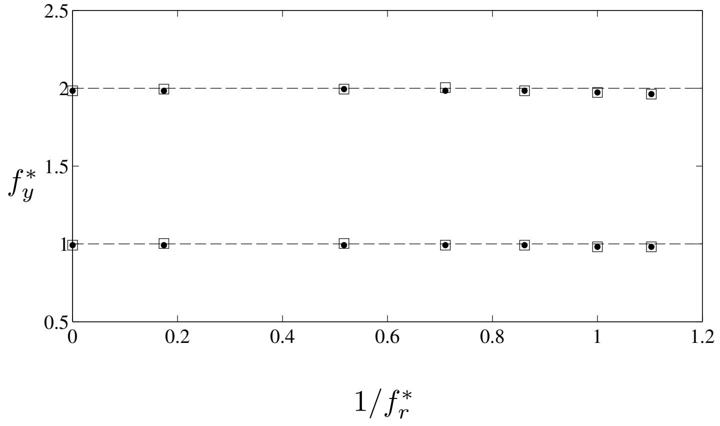

Figure 5.13 Normalized frequency of transverse vibrations at U^* = 6 and ζ_{TMD} = 0.24. (●) corresponds to increasing $1/f_r^*$ and (□) corresponds to decreasing $1/f_r^*$.

and f_2 decrease with increasing $1/f_r^*$. The presence of more than one dominant frequency in the frequency response for these experimental conditions agrees with the results obtained from the simplified model (Fig. 5.7). However, in contrast to two dominant frequencies observed experimentally, the model predicts three dominant frequencies, i.e., f_1, f_2, and f_n. The results presented in Fig. 5.14 indicate that hysteresis occurs at $1/f_r^* \approx 0.5$. Specifically, when $1/f_r^*$ = 0.52 is set by increasing $1/f_r^*$, the spectrum of transverse vibrations features dominant peaks centered at f_1, harmonics of f_1, and f_2, with $f_1 = 0.96f_n$ and $f_2 = 2.12f_n$. However, when $1/f_r^*$ = 0.52 is set by decreasing $1/f_r^*$, spectrum of transverse vibrations has peaks centered only at f_1 and harmonics of f_1.

Temporal analysis of frequencies of transverse vibrations

To investigate temporal variations in the frequency of transverse vibrations, spectrograms of transverse vibrations were computed using a short time fast Fourier transform (SFFT) technique. The width of time-window utilized in the SFFT was approximately ten cycles of the cylinder oscillations.

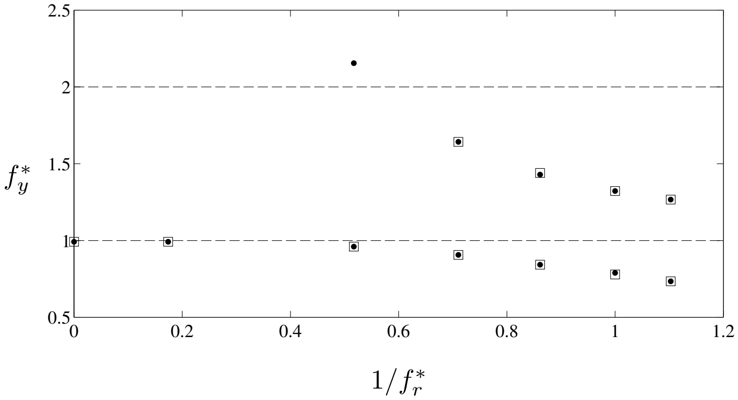

Figure 5.14 Normalized frequency of transverse vibrations at U^* = 6 and ζ_{TMD} = 0. (●) corresponds to increasing $1/f_r^*$ and (□) corresponds to decreasing $1/f_r^*$.

Figure 5.15 shows spectrogram of transverse vibrations for ζ_{TMD} = 0.24 and $1/f_r^* = 1$. The results show that the dominant frequency of transverse vibrations, which is equal to f_n, does not vary in time. Indeed, for all of the experiments performed for ζ_{TMD} = 0.24, temporal variations were not observed in the frequency response of the structure.

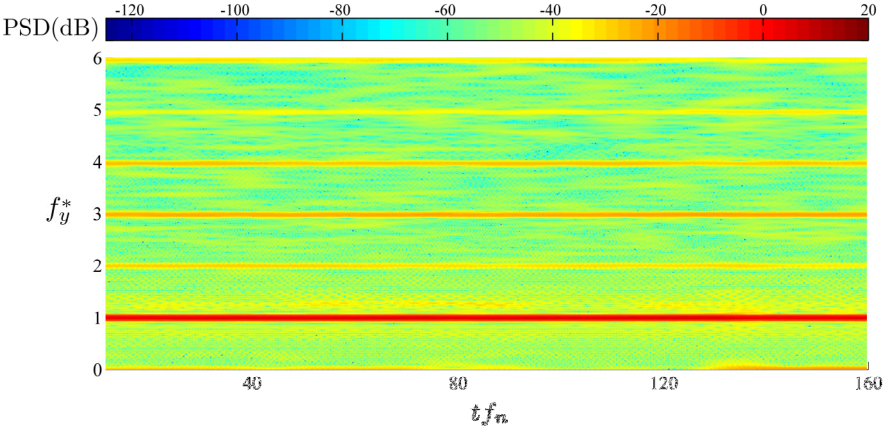

Figure 5.15 Spectrogram of transverse vibrations at U^* = 6, ζ_{TMD} = 0.24, and $1/f_r^*$ = 1.

For ζ_{TMD} = 0, analysis of experimental data indicate that temporal variation may occur in the frequency response for a range of $1/f_r^*$. Figures 5.16a and c show spectrograms of the transverse vibrations at $1/f_r^*$ = 0 and 0.17, respectively. The results presented in Figs. 5.16a and c indicate that the dominant frequency of transverse vibrations is invariant in time, similar to the results presented in Fig. 5.15. The spectra of transverse vibrations presented in Figs. 5.16b and d show that, for $1/f_r^*$ = 0 and 0.17, the frequency response is characterized by the natural frequency (f_n) and harmonics of the natural frequency. For $1/f_r^* > 0.5$, the dominant frequency of transverse vibrations does not match the natural frequency of the structure. Figures 5.17a, c, e, g, and i show spectrograms of transverse vibrations at $1/f_r^*$ = 0.52, 0.71, 0.86, 1, and 1.1, respectively, with the corresponding spectra of transverse vibrations presented in Figs. 5.17b, d, f, h, and j. The results shown in Fig. 5.17 were obtained for increasing values of $1/f_r^*$. The data in Figs. 5.17a-h show that the frequencies of transverse vibrations are centered at f_1, f_2, and harmonics of f_1. For $0.52 \leq 1/f_r^* \leq 0.86$, the spectrograms (Figs. 5.17a, c, and f) indicate that f_1 is the dominant frequency of transverse vibrations. For $1/f_r^*$ = 1, Fig. 5.17g shows that the dominant frequency intermittently switches between f_1 and f_2. For $1/f_r^*$ > 1, the dominant frequency of vibrations corresponds to f_2, with lower magnitude peaks centered at f_1 and harmonics of f_2 also observed in the spectra (Fig. 5.17j).

Figures 5.18a-j show spectrograms and spectra of transverse vibrations for $1/f_r^* \geq 0.17$ and for the case of decreasing $1/f_r^*$. The results illustrate similar trends to those observed for the case of increasing $1/f_r^*$. However, the ranges of $1/f_r^*$ corresponding to specific trends are affected by how the investigated values of $1/f_r^*$ were set. Specifically, for $1/f_r^*$ = 1, the results in Fig. 5.18a show that the dominant frequency of transverse vibrations is f_2 and does not switch intermittently with f_1. The

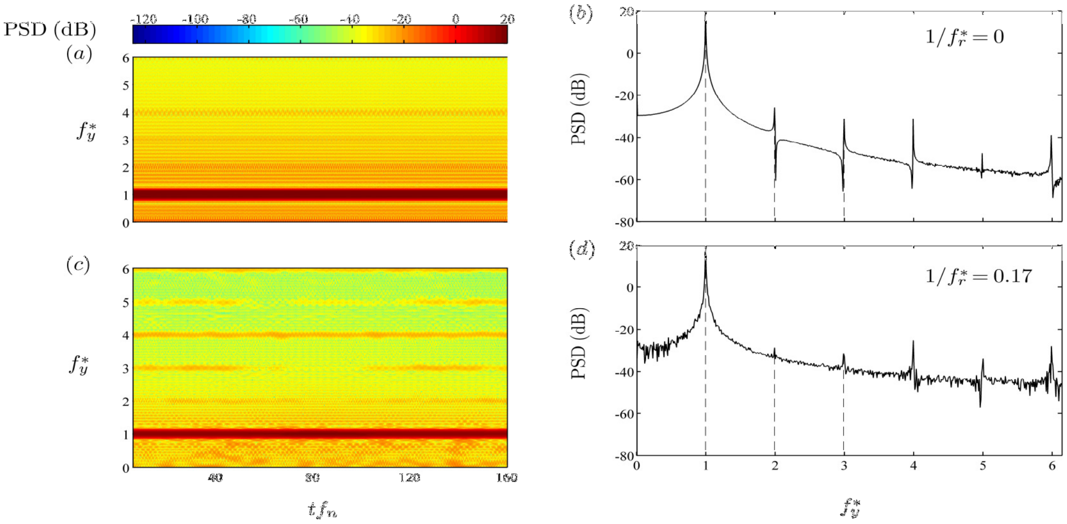

Figure 5.16 Spectrograms and spectra of transverse vibrations at U^* = 6 and ζ_{TMD} = 0: (a, b) $1/f_r^*$ = 0, and (c, d) $1/f_r^*$ = 0.17.

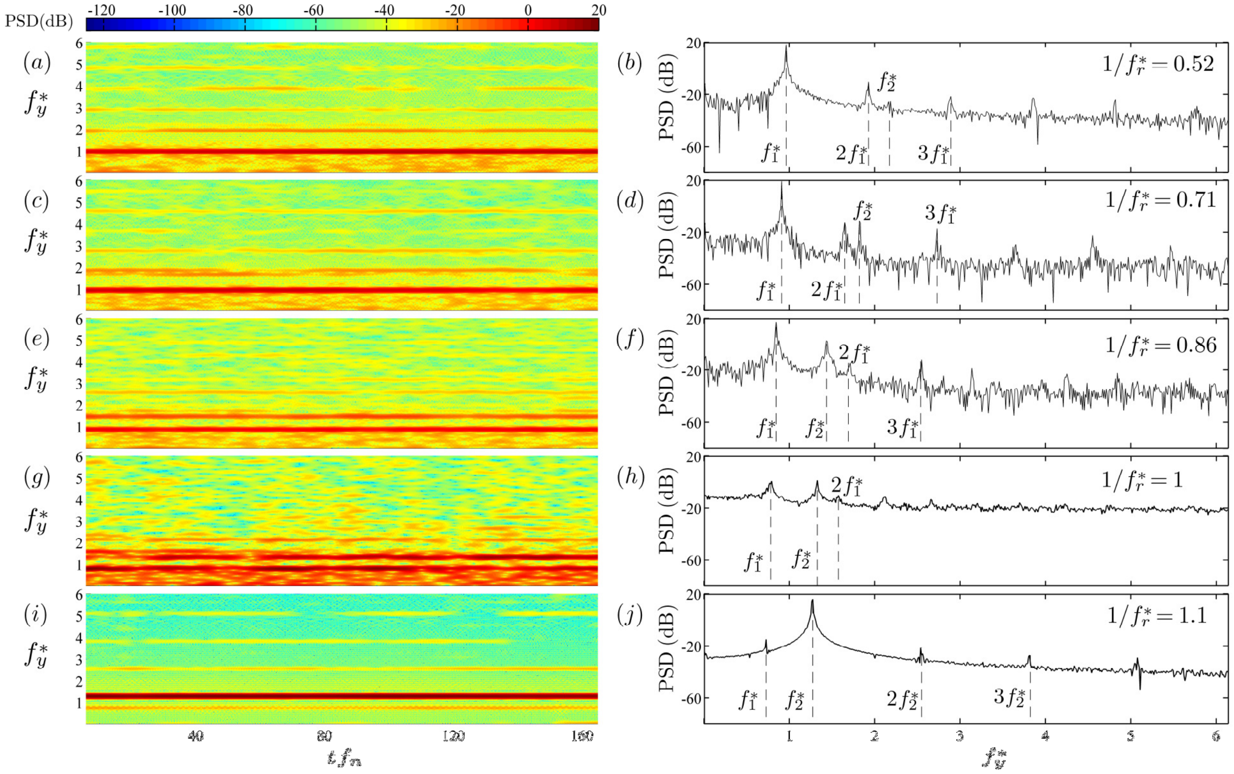

Figure 5.17 Spectrograms and spectra of transverse vibrations for increasing values of $1/f_r^*$ at U^* = 6 and ζ_{TMD}= 0.

intermittent switching in the dominant frequency between f_1 and f_2 is observed for $1/f_r^* = 0.86$ (Fig. 5.18c). For $1/f_r^* = 0.71$, the energy content associated with f_2 diminishes, and the dominant peak is associated with f_1. The results pertaining to $1/f_r^* \leq 0.71$ (Figs. 5.18e-j) are in agreement with those obtained by increasing $1/f_r^*$ (Figs. 5.16 and 5.17a-d).

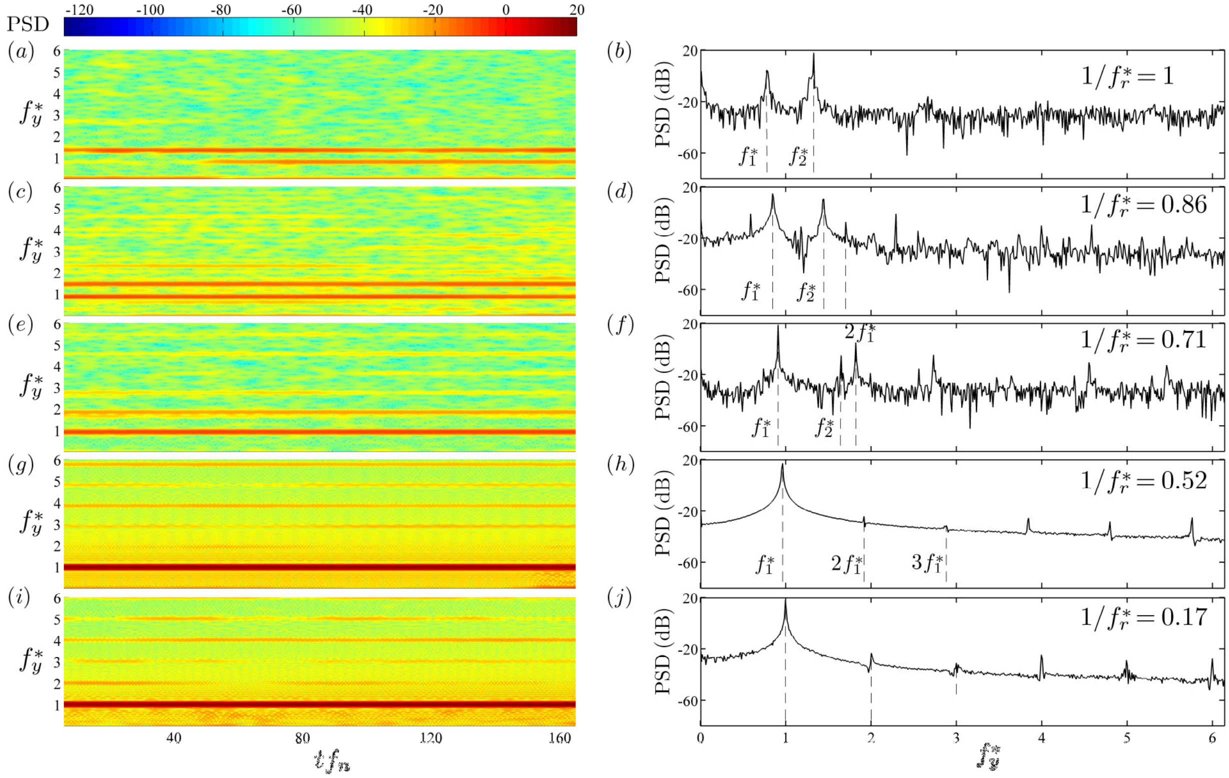

Figure 5.18 Spectrograms and spectra of transverse vibrations for decreasing values of $1/f_r^*$, at $U^* = 6$ and $\zeta_{TMD} = 0$.

Frequencies of streamwise vibrations

Figures 5.19a and b show spectra of streamwise vibrations at $U^* = 6$, $1/f_r^* = 1.1$, and $\zeta_{TMD} = 0.24$, and 0, respectively. Spectra of transverse vibrations are also included in the figures for comparison. Note that the spectra of streamwise vibrations in both figures are increased by 20 dB for clarity. The results presented in both figures show that the dominant frequencies of streamwise vibrations match those of transverse vibrations. For example, for ζ_{TMD} = 0.24, the dominant peak occurs at the natural frequency of the structure in the spectra of streamwise and transverse vibrations. Indeed, for all of the cases tested in the synchronization region, spectral analysis of the vibrations showed that the dominant frequencies of streamwise and transverse vibrations match.

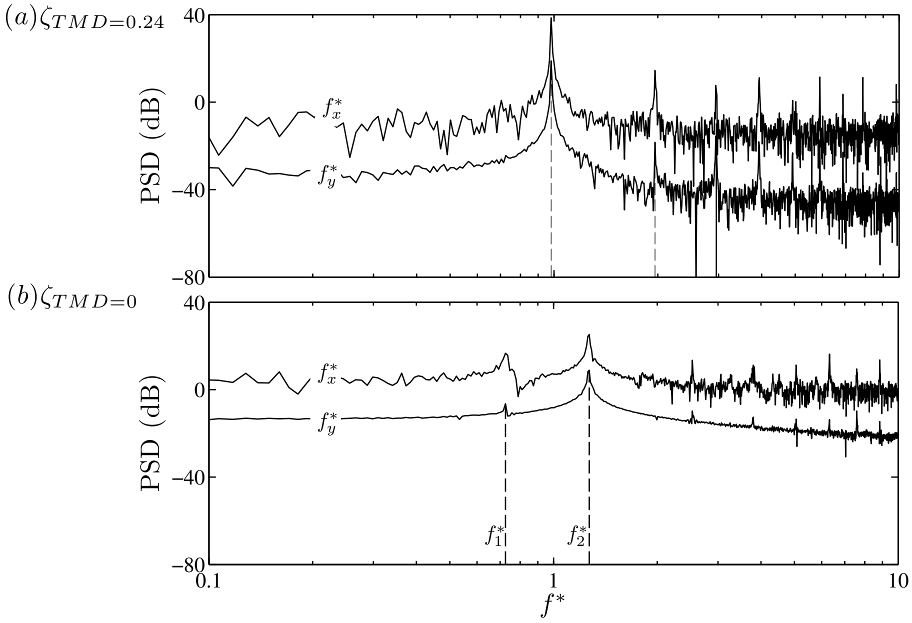

Figure 5.19 Spectra of streamwise vibrations at $U^* = 6$, $1/f_r^* = 1.1$, and for (a) $\zeta_{\mathrm{TMD}} = 0.24$ and (b) $\zeta_{\mathrm{TMD}} = 0$.

5.2.3 Cylinder tip trajectories

Figures 5.20 and 5.21 illustrate the effect of $1/f_r^*$ on cylinder tip trajectories for ζ_{TMD} = 0.24 and 0, respectively. The results in Fig. 5.20 are presented for three reduced velocities tested in the synchronization region (U^* = 5.44, 6, and 6.48) and the results in Fig. 5.21 are presented for U^* = 6. The phase angles between the streamwise and transverse vibrations corresponding to the results presented in

Figs. 5.20 and 5.21 are presented in Figs. 5.22 and 5.23, respectively. Figs. 5.20a, d, and g show that the cylinder traces elliptic trajectories at $1/f_r^* = 0$, i.e., when the pendulum is restrained. The results show that increasing the tuning frequency ratio from $1/f_r^* = 0$ to 1 significantly decreases the amplitudes of vibrations. The results presented in Fig. 5.22 and 5.23 indicate that the phase angle is relatively constant for $1/f_r^* = 0$ and 0.2. However, at the tuned condition ($1/f_r^* = 1$), the phase angle significantly fluctuates between -180° and 180°. This is speculated to be linked to the very low amplitudes of transverse and streamwise vibrations observed at the tuned condition.

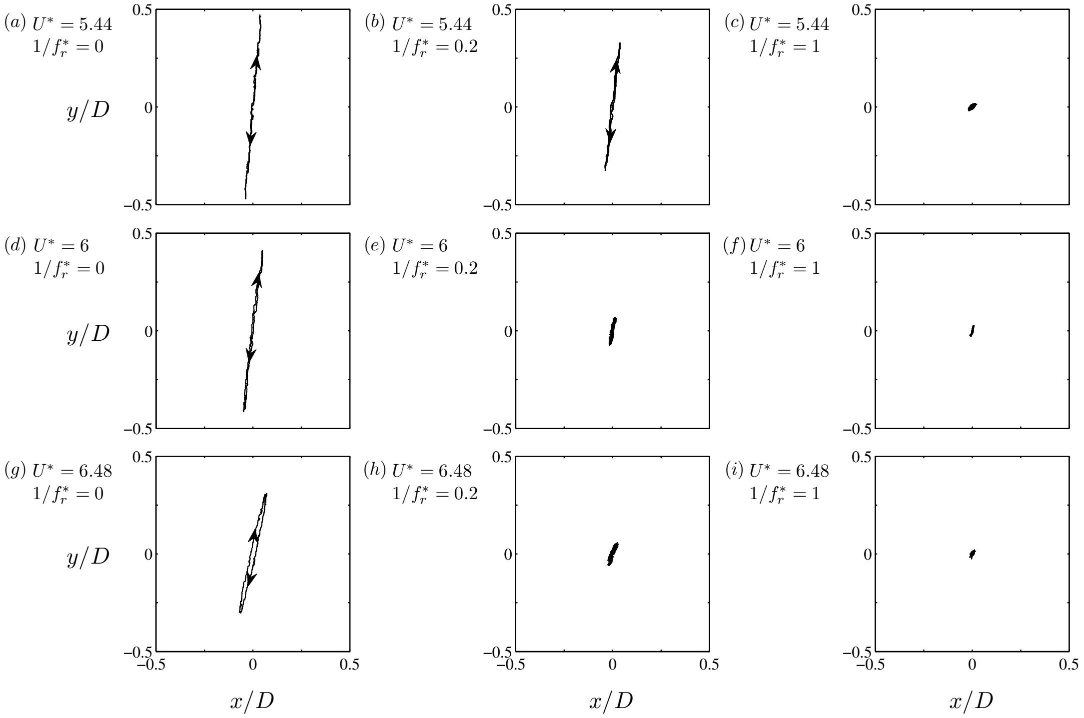

Figure 5.20 Cylinder tip trajectories for $\zeta_{TMD} = 0.24$.

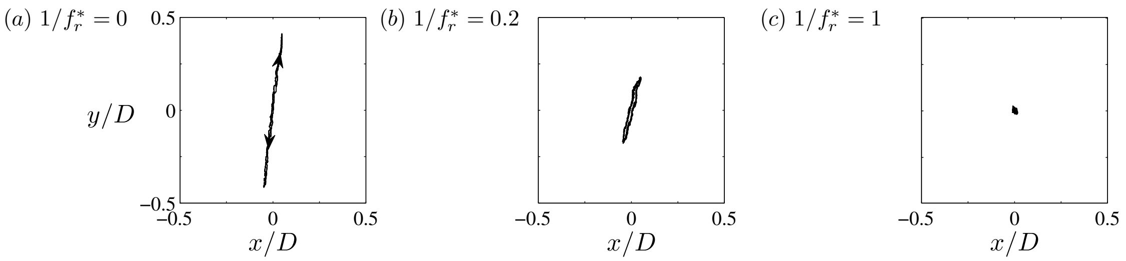

Figure 5.21 Cylinder tip trajectories for $U^* = 6$ and $\zeta_{TMD} = 0$.

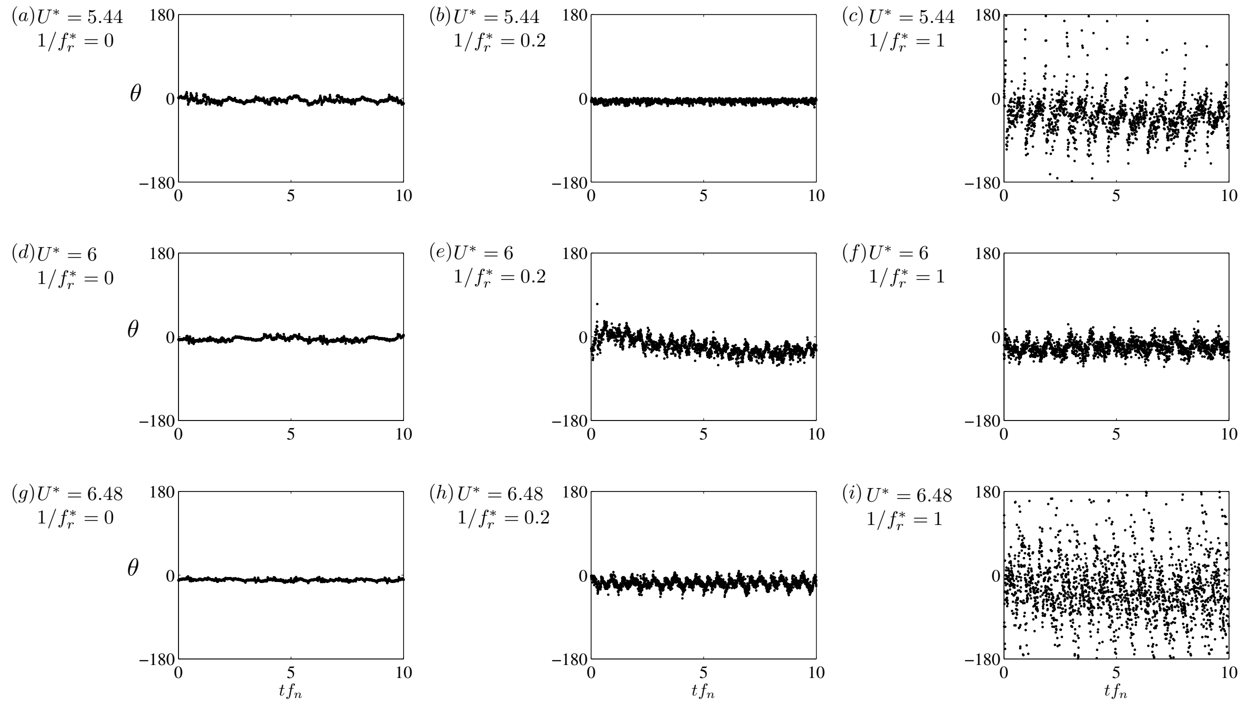

Figure 5.22 Phase angles for $\zeta_{TMD} = 0.24$.

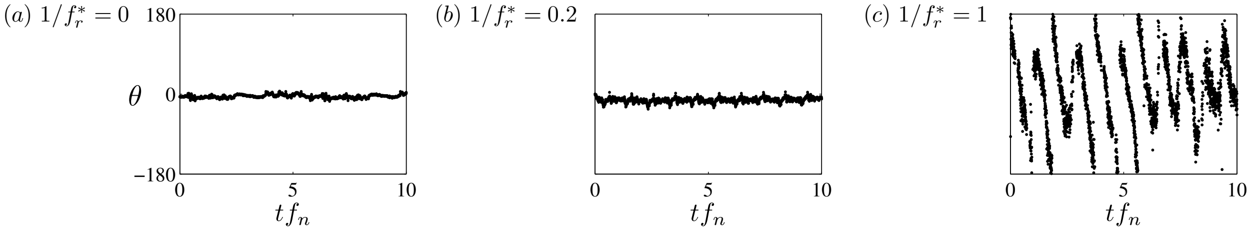

Figure 5.23 Phase angles for $U^* = 6$ and $\zeta_{TMD} = 0$.

5.2.4 Mathematical modeling of the frequency response

The experimental results demonstrate that the TMD damping ratio (ζ_{TMD}) and tuning frequency ratio ($1/f_r^*$) can significantly affect the frequency response of the structure. In this section, a mathematical model is introduced to gain added insight into the effects of ζ_{TMD} and $1/f_r^*$ on the frequency response of the structure. The results are presented for both free vibrations and vortex-induced vibrations of the structure.

Figure 5.24 shows schematic of the cylindrical structure equipped with the tuned-mass damper, where ε and χ indicate the streamwise degree of freedom of the structure and the pendulum, respectively (Fig. 5.24). The transverse degree of freedom of the structure and the pendulum are ϕ and γ, respectively. Lagrangian equations of free vibrations of the structure are presented in Eqs. 5.4-5.7.

$$\frac{d}{dt}\left(\frac{\partial \pounds}{\partial \dot{\varepsilon}}\right)-\frac{\partial \pounds}{\partial \varepsilon}=\frac{\partial Q}{\partial \dot{\varepsilon}} \tag{5.4}$$

$$\frac{d}{dt}\left(\frac{\partial \pounds}{\partial \dot{\phi}}\right)-\frac{\partial \pounds}{\partial \phi}=\frac{\partial Q}{\partial \dot{\phi}} \tag{5.5}$$

$$\frac{d}{dt}\left(\frac{\partial \pounds}{\partial \dot{\chi}}\right)-\frac{\partial \pounds}{\partial \chi}=\frac{\partial Q}{\partial \dot{\chi}} \tag{5.6}$$

$$\frac{d}{dt}\left(\frac{\partial \pounds}{\partial \dot{\gamma}}\right)-\frac{\partial \pounds}{\partial \gamma}=\frac{\partial Q}{\partial \dot{\gamma}} \tag{5.7}$$

$\pounds$ is the Lagrangian of the system ($\pounds$ = T - V); T and V are the kinetic and potential energies of the system, respectively; Q, T, and V are defined in Eqs. 5.8-5.10.

$$Q=-\frac{1}{2}Cb^2\dot{\varepsilon}^2-\frac{1}{2}Cb^2\dot{\phi}^2-\frac{1}{2}C_{TMD}l_p^2\dot{\chi}^2-\frac{1}{2}C_{TMD}l_p^2\dot{\gamma}^2 \tag{5.8}$$

$$T = \frac{1}{2} I(\dot{\varepsilon}^2 + \dot{\phi}^2) + \frac{1}{2} m[(L_p \dot{\varepsilon} + l_p \dot{\chi})^2 + (L_p \dot{\phi} + l_p \dot{\gamma})^2] \tag{5.9}$$

$$V = \frac{1}{2} K b^2 (\varepsilon^2 + \phi^2) + K_c b^2 \varepsilon\phi + M g l_g [1 - \frac{1}{2}(\varepsilon^2 + \phi^2)] + mg[(L_p - l_p) + \frac{1}{2} l_p (\chi^2 + \gamma^2) - \frac{1}{2}(L_p - l_p)(\varepsilon^2 + \phi^2)] \tag{5.10}$$

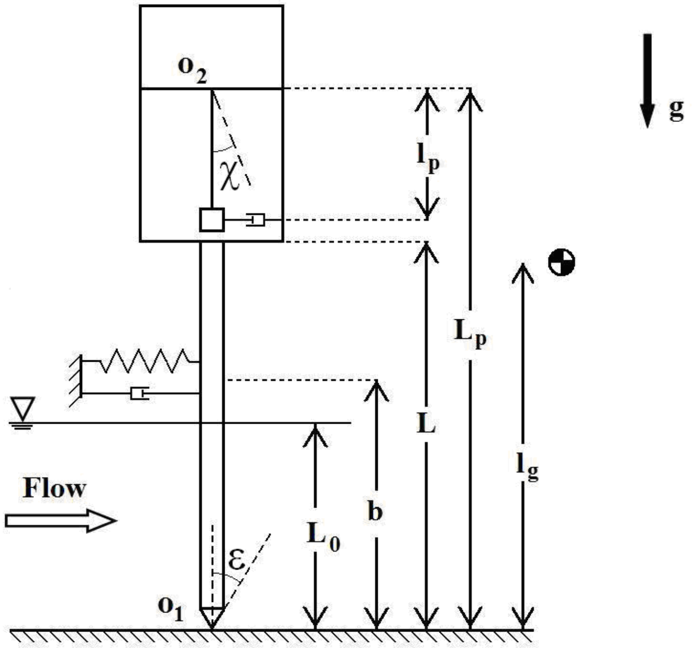

Figure 5.24 Schematic of the cylindrical structure equipped with the tuned-mass damper.

Substituting Eqs. 5.8-5.10 in Eqs. 5.4-5.7 and introducing $l^* = \frac{L_p}{l_p}$ and $I_s = \frac{m_{TMD} L_p l_p}{I + m_{TMD} L_p^2}$, the equations of free vibrations of the structure are obtained.

$$\frac{d^2\varepsilon}{dt^{*2}} + 4\pi\zeta \frac{d\varepsilon}{dt^*} + 4\pi^2 \varepsilon + 4\pi^2 (\frac{f_c}{f_a})^2 \phi + I_s \frac{d^2\chi}{dt^{*2}} = 0 \tag{5.11}$$

$$\frac{d^2\phi}{dt^{*2}} + 4\pi\zeta \frac{d\phi}{dt^*} + 4\pi^2 \phi + 4\pi^2 (\frac{f_c}{f_a})^2 \varepsilon + I_s \frac{d^2\gamma}{dt^{*2}} = 0 \tag{5.12}$$

$$\frac{d^2\chi}{dt^{*2}}+4\pi\zeta_{TMD}\frac{d\chi}{dt^*}+4\pi^2 f_r^{*2}\chi+1^*\frac{d^2\varepsilon}{dt^{*2}}=0 \tag{5.13}$$

$$\frac{d^2\gamma}{dt^{*2}}+4\pi\zeta_{TMD}\frac{d\gamma}{dt^*}+4\pi^2 f_r^{*2}\gamma+1^*\frac{d^2\phi}{dt^{*2}}=0 \tag{5.14}$$

The values of the non-dimensional governing parameters utilized in the parametric study are selected to match those investigated experimentally. Specifically, values of f_c/f_a, ζ, and ζ_{TMD} match the corresponding values presented in Table 5.2 for $U^* = 6$. The values of the governing parameters are presented in Table 5.3.

Table 5.3 Governing non-dimensional parameters.

Parameter	**Value**
f_c/f_a	0.3
ζ	0.01
ζ_{TMD}	0 and 0.24
$1/f_r^*$	0-1.6

Equations 5.11-5.14 were solved numerically for the following initial conditions:

$\varepsilon(t^{**}=0)=0.01$, and $\phi(t^{**}=0)=\chi(t^{**}=0)=\gamma(t^{**}=0)=\dot{\varepsilon}(t^{**}=0)=\dot{\phi}(t^{**}=0)=\dot{\chi}(t^{**}=0)=\dot{\gamma}(t^{**}=0)=0$

Figure 5.25 shows the spectra of transverse free vibrations of the structure at $1/f_r^*=1.1$ and for $0 \le \zeta_{TMD} \le 1$. For clarity, each spectrum is stepped by 20 dB with respect to the previous spectrum obtained for a lower TMD damping ratio. The results show that, for $0 \le \zeta_{TMD} \lesssim 0.24$, the frequency response of the structure features two dominant peaks, one centered at a frequency lower than f_n (f_1) and the other centered at a frequency higher than f_n (f_2). As the TMD damping ration increases, the spectral peaks centered at f_1 and f_2 become less pronounced. For $0.24 \lesssim \zeta_{TMD} \le 1$, the two peaks merge, forming a single dominant peak at the natural frequency. This indicates that, for $0.24 \lesssim \zeta_{TMD} \leq 1$, the TMD does not significantly affect the frequency response of the structure in free vibrations. Similar conclusion can be reached using the simplified model discussed in this Chapter (section 5.1).

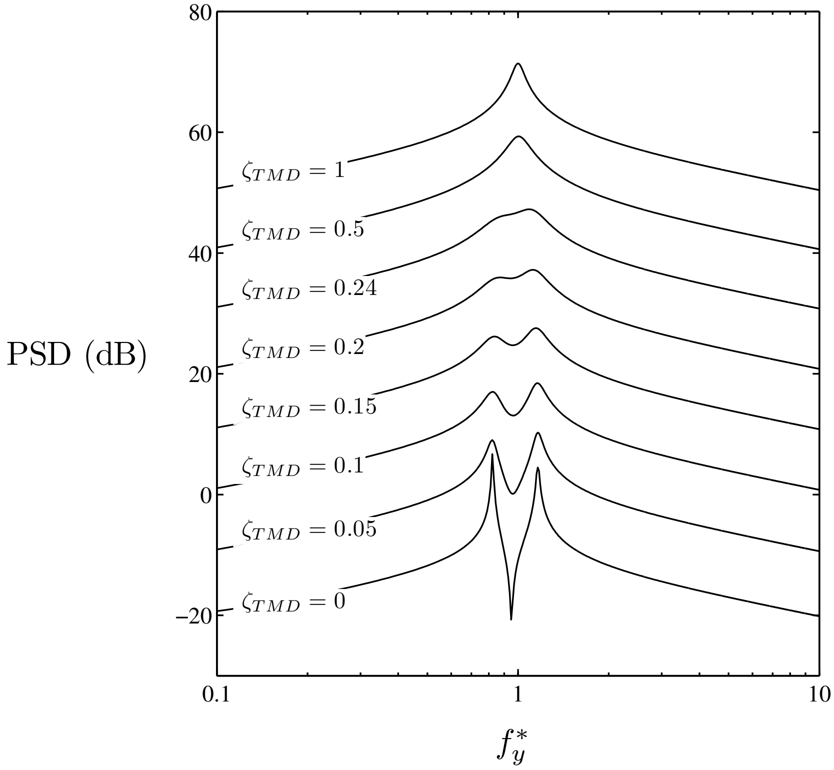

Figure 5.25 Model predictions for frequency of transverse free vibrations of the structure at $1/f_r^* = 1.1$.

Figures 5.26a and b illustrate the effect of $1/f_r^*$ on the spectra of transverse free vibrations for $\zeta_{TMD} = 0.24$ and 0, respectively. For clarity, each spectrum is stepped by 20 dB with respect to the previous spectrum obtained for a lower tuning frequency ratio. The results presented in Fig. 5.26a indicate that, for $\zeta_{TMD} = 0.24$, the frequency response of transverse free vibrations is characterized by the natural frequency of the structure, with broader peaks observed for $1/f_r^* \approx 1$. In contrast, for $\zeta_{TMD} = 0$, the results presented in Fig. 5.26b show that the spectra of transverse free vibrations feature two peaks centered at frequencies different from f_n (f_1 and f_2). The results show that increasing the tuning frequency ratio decreases both f_1 and f_2. Specifically, the results presented in Fig. 5.26b show that increases $1/f_r^*$ from 0.17 to 1.6 decreases f_1 from 0.99 to 0.62 and f_2 from 6.5 to 1.02.

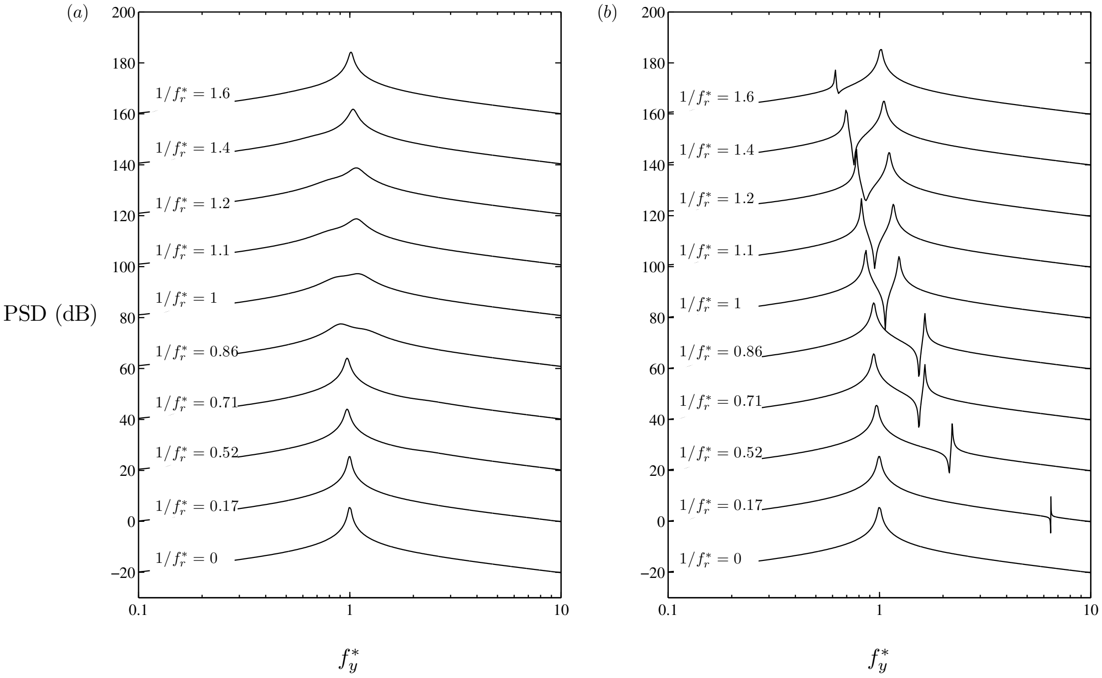

Figure 5.26 Model predictions for frequency of transverse free vibrations of the structure for (a) $\zeta_{TMD} = 0.24$ and (b) $\zeta_{TMD} = 0$.

As the first step towards modeling vortex-induced vibrations, it is instructive to investigate the response of the structure to single harmonic forcing. The forcing frequencies in streamwise and transverse directions are assumed to be $f_{e,x}$ and $f_{e,y}$, respectively. The following system of equations represents the equations of forced vibrations of the structure.

$$\frac{d^2\varepsilon}{dt^{**2}} + 4\pi\zeta\frac{d\varepsilon}{dt^{**}} + 4\pi^2\varepsilon + 4\pi^2(\frac{f_c}{f_a})^2\phi + I_s\frac{d^2\chi}{dt^{**2}} = \sin(2\pi\frac{f_{e,x}}{f_n}t^{**} + \psi) \tag{5.15}$$

$$\frac{d^2\phi}{dt^{**2}} + 4\pi\zeta\frac{d\phi}{dt^{**}} + 4\pi^2\phi + 4\pi^2(\frac{f_c}{f_a})^2\varepsilon + I_s\frac{d^2\gamma}{dt^{**2}} = \sin(2\pi\frac{f_{e,y}}{f_n}t^{**}) \tag{5.16}$$

$$\frac{d^2\chi}{dt^{**2}} + 4\pi\zeta_{TMD}\frac{d\chi}{dt^{**}} + 4\pi^2 f_r^{*2}\chi + 1^*\frac{d^2\varepsilon}{dt^{**2}} = 0 \tag{5.17}$$

$$\frac{d^2\gamma}{dt^{**2}} + 4\pi\zeta_{TMD}\frac{d\gamma}{dt^{**}} + 4\pi^2 f_r^{*2}\gamma + 1^*\frac{d^2\phi}{dt^{**2}} = 0 \tag{5.18}$$

The system of Eqs. 5.15-5.18 was solved numerically. The governing parameters, f_c/f_a, ζ, and ζ_{TMD}, were selected to match those presented in Table 5.3. Figure 5.27 illustrates a general case when the frequency of forcing does not match the fundamental frequencies of the structure identified for free vibrations, with $f_{e,x} = 0.5f_n$ and $f_{e,y} = 1.3f_n$. Figures 5.27a and c show the spectra of transverse and streamwise vibrations, respectively, for $\zeta_{TMD} = 0.24$. The results illustrate that the frequencies of both transverse and streamwise vibrations are characterized by the natural frequency, the frequency of excitation in the streamwise direction, and the frequency of excitation in the transverse direction. Figures 5.27b and d show the spectra of transverse and streamwise vibrations, respectively, for $\zeta_{TMD} = 0$. The results presented in Fig. 5.27b and d illustrate that the frequencies of both transverse and streamwise vibrations are characterized by f_1, f_2, the frequency of excitation in the streamwise direction ($f_{e,x}$), and the frequency of excitation in the transverse direction ($f_{e,y}$). Comparing the results presented in Fig. 5.27 and those for free vibrations (Fig. 5.26), it can be seen that the frequency response of the structure to forced vibrations is characterized by the fundamental frequencies of the structure (i.e., frequencies determined from the free vibration tests), frequency of excitation in the streamwise direction, and the frequency of excitation in the transverse direction.

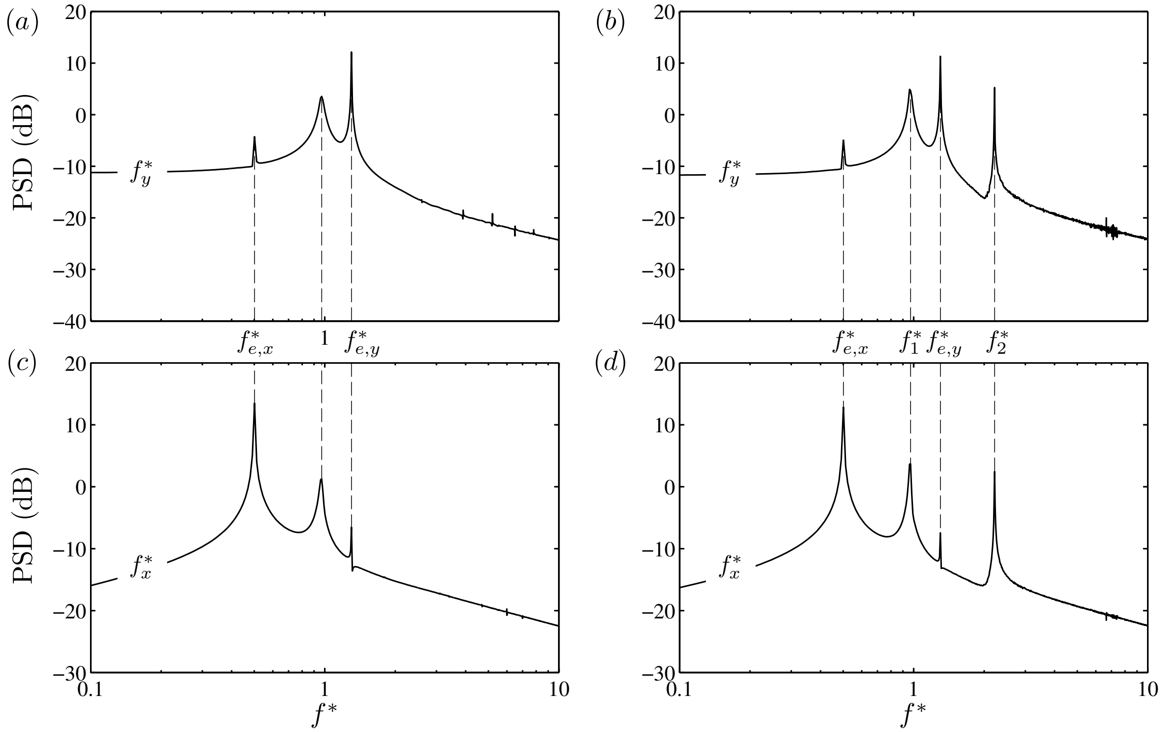

Figure 5.27 Frequency of transverse and streamwise forced vibrations of the structure at $1/f_r^* = 0.52$, $f_{e,x}^* = 0.5$, $f_{e,y}^* = 1.3$; (a,c) $\zeta_{TMD} = 0.24$ and (b,d) $\zeta_{TMD} = 0$.

Clearly, proper modeling of fluid forcing is critical for creating a viable mathematical model of vortex-induced vibrations. Since the results presented in Fig. 5.27 demonstrated that the TMD damping ratio can significantly affect the frequency response of the system, it can be speculated that this parameter may influence the nature of fluid structure interactions in the case of vortex-induced vibrations.

For $\zeta_{TMD} = 0.24$, the model shows that the response of the structure with the TMD is characterized by a single frequency, i.e., the natural frequency (e.g., Fig. 5.26a). This is similar to the behaviour of the structure with the pendulum restrained (Fig. 5.26a for the case $1/f_r^* = 0$) or that without a TMD (Fig. 3.3). Thus, it is reasonable to assume that the presence of the TMD will not affect the nature of vortex-structure interactions in the synchronization region, where the forcing frequency is linked to the natural frequency of the structure. Based on this argument, fluid forcing is modeled using the same formulation as that employed in Chapter 4 for VIV of a two DOF pivoted cylinder. Introducing $U_{r,TMD}=(\frac{U^*}{U_c^*})^2(\frac{I+m_{TMD}L_p^2}{I+m_{TMD}L_p^2+I_A})$, $f_{r,TMD}=\frac{f_a}{f_n}\frac{m_{TMD}L_p^2}{I+m_{TMD}L_p^2+I_A}$, and $I_s^*=\frac{m_{TMD}L_p l_p}{I+m_{TMD}L_p^2+I_A}$, the equations of vortex-induced vibrations of the structure can be represented in the following non-dimensional form:

$$\frac{d^2\varepsilon}{dt^{**2}}+4\pi\zeta f_{r,TMD}\frac{d\varepsilon}{dt^{**}}+4\pi^2\varepsilon+4\pi^2U_{r,TMD}\phi+I_s^*\frac{d^2\chi}{dt^{**2}}=\frac{2}{\pi}\frac{U^{*2}C_D D}{(I^*+C_A)L_0}\sin(4\pi t^{**}+\psi) \qquad (5.19)$$

$$\frac{d^2\phi}{dt^{**2}}+4\pi\zeta f_{r,TMD}\frac{d\phi}{dt^{**}}+4\pi^2\phi+4\pi^2U_{r,TMD}\varepsilon+I_s^*\frac{d^2\gamma}{dt^{**2}}=\frac{2}{\pi}\frac{U^{*2}C_L D}{(I^*+C_A)L_0}\sin(2\pi t^{**}) \qquad (5.20)$$

$$\frac{d^2\chi}{dt^{**2}}+4\pi\zeta_{TMD}\frac{d\chi}{dt^{**}}+4\pi^2 f_r^{*2}\chi+1^*\frac{d^2\varepsilon}{dt^{**2}}=0 \qquad (5.21)$$

$$\frac{d^2\gamma}{dt^{**2}}+4\pi\zeta_{TMD}\frac{d\gamma}{dt^{**}}+4\pi^2 f_r^{*2}\gamma+1^*\frac{d^2\phi}{dt^{**2}}=0 \qquad (5.22)$$

where, the terms on the right-hand-side of Eqs. 5.19 and 5.20 are non-dimensional fluid moments previously presented in Chapter 4. Figures 5.28a and b show spectra of transverse and streamwise vibrations, respectively, for $\zeta_{TMD} = 0.24$ and $0 \le 1/f_r^* \le 1.6$. For clarity, each spectrum is stepped by 20 dB with respect to the previous spectrum obtained for a lower tuning frequency ratio. The results presented in Fig. 5.28a show that the dominant frequency of transverse vibrations occurs at the natural frequency of the structure. In contrast, the spectrum of streamwise vibrations (Fig. 5.28b) features two peaks, one centered at the natural frequency and the other at the first harmonic of the natural frequency. These results are in agreement with the experimental data presented in Fig. 5.19a. Thus, it can concluded that, in the synchronization region, the nature of fluid-structure interactions is not affected by the presence of the TMD if the TMD damping ratio is relatively high. Specifically, in the synchronization region, the frequency of fluid forcing in the streamwise direction is twice that in the transverse direction, and is twice the natural frequency of the structure.

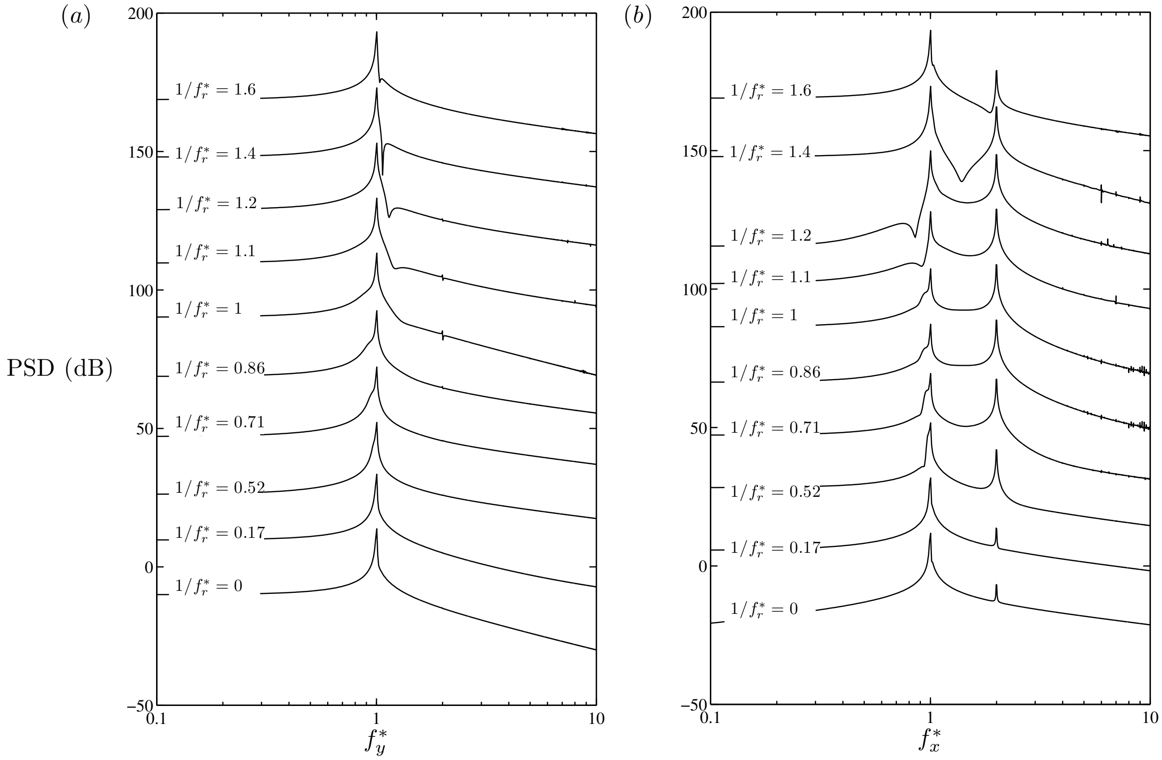

Figure 5.28 Model predictions for spectra of (a) transverse vibrations and (b) streamwise vibrations at ζ_{TMD} = 0.24.

For $\zeta_{TMD} = 0$, model suggests that, depending on $1/f_r^*$, the presence of the TMD may significantly influence the frequency response of the structure in free-vibrations as well as in forced vibrations. In particular, for $1/f_r^* < 0.5$, the frequency response of the structure is characterized by a single fundamental frequency, i.e., the natural frequency of the structure; whereas, for $0.5 < 1/f_r^* \leq 1.1$, the frequency response of the free vibrations of the structure is characterized by two fundamental frequencies f_1 and f_2.

Thus, it can be speculated that, for $1/f_r^* < 0.5$, the fluid forcing can be modeled using the same approach as that employed for $\zeta_{TMD} = 0.24$ (Eqs. 5.19-5.22). However, for $1/f_r^* > 0.5$, in the synchronization region, the forcing frequency should be related to the fundamental frequencies f_1 and f_2 rather than f_n. Indeed, a comparative analysis of the model predictions for the forced vibrations (Figs. 5.27b and d) and the experimental results (Fig. 5.19b) suggests that the fluid forcing frequency does not involve f_n, as no peaks are observed at f_n in the spectra of experimentally measured vortex-induced vibrations. Thus, a different model for fluid forcing is required. It is proposed to model that the fluid forcing in the transverse direction as a linear combination of two sinusoidal functions with characteristic frequencies of f_1 and f_2. Then, the fluid forcing in the streamwise direction can be assumed to be a linear combination of two sinusoidal functions with characteristic frequencies of $2f_1$ and $2f_2$. The proper formulation for VIV of a two DOF pivoted circular cylinder equipped with a two DOF TMD with relatively low TMD damping ratios is devised in the following system of equations:

$$\frac{d^2\varepsilon}{dt^{**2}} + 4\pi\zeta f_{r,TMD}\frac{d\varepsilon}{dt^{**}} + 4\pi^2\varepsilon + 4\pi^2 U_{r,TMD}\phi + I_s^*\frac{d^2\chi}{dt^{**2}} = \Delta^*\Lambda[\sin(4\pi\frac{f_1}{f_n}t^{**}) + (\frac{1}{\Lambda}-1)\sin(4\pi\frac{f_2}{f_n}t^{**})] \quad (5.23)$$

$$\frac{d^2\phi}{dt^{**2}} + 4\pi\zeta f_{r,TMD}\frac{d\phi}{dt^{**}} + 4\pi^2\phi + 4\pi^2 U_{r,TMD}\varepsilon + I_s^*\frac{d^2\gamma}{dt^{**2}} = \frac{\Delta^* C_L\Lambda}{C_D}[\sin(2\pi\frac{f_1}{f_n}t^{**}) + (\frac{1}{\Lambda}-1)\sin(2\pi\frac{f_2}{f_n}t^{**})] \quad (5.24)$$

$$\frac{d^2\chi}{dt^{**2}} + 4\pi\zeta_{TMD}\frac{d\chi}{dt^{**}} + 4\pi^2 f_r^{*2}\chi + l^*\frac{d^2\varepsilon}{dt^{**2}} = 0 \quad (5.25)$$

$$\frac{d^2\gamma}{dt^{**2}} + 4\pi\zeta_{TMD}\frac{d\gamma}{dt^{**}} + 4\pi^2 f_r^{*2}\gamma + l^*\frac{d^2\phi}{dt^{**2}} = 0 \quad (5.26)$$

where, $\Delta^* = \frac{2}{\pi}\frac{U^{*2}C_D D}{(I^* + C_A)L_0\sqrt{(1-\Lambda)^2 + (\Lambda)^2}}$ and Λ the weighting factor characterizing relative magnitudes of the fluid forcing associated with f_1 and f_2. Analysis of the spectra of transverse and streamwise vibrations showed that the frequency of transverse vibrations is characterized by f_1 and f_2 and the frequency of streamwise vibrations is characterized by f_1, f_2, $2f_1$, and $2f_2$. This is illustrated in Figs. 5.29a and b, which depict spectra of transverse and streamwise vibrations using data obtained for $1/f_r^* = 1.1$ and $0 \leq \Lambda \leq 1$. The results indicate that varying Λ does not change the dominant frequencies of transverse and streamwise vibrations. However, changing Λ can significantly influence the relative magnitude of the corresponding spectral peaks. The results presented in Figs. 5.29a and b for $\Lambda = 1$ are similar to the experimental results presented in Fig. 5.19b. It can concluded that, in the synchronization region, the frequency of fluid forcing in the transverse direction is characterized by the fundamental frequencies of the structure (i.e., f_1 and f_2), and the fluid forcing in the streamwise direction is characterized by the first harmonic of the fundamental frequencies ($2f_1$ and $2f_2$) for relatively low TMD damping ratios and $1/f_r^* > 0.5$. The foregoing discussion presented in this section suggests that the definition of synchronization or lock-in, which traditionally describes matching of the forcing frequency and the natural frequency for one DOF structures, can be extrapolated to the matching of the forcing frequency to the fundamental frequencies of the higher DOF structures.

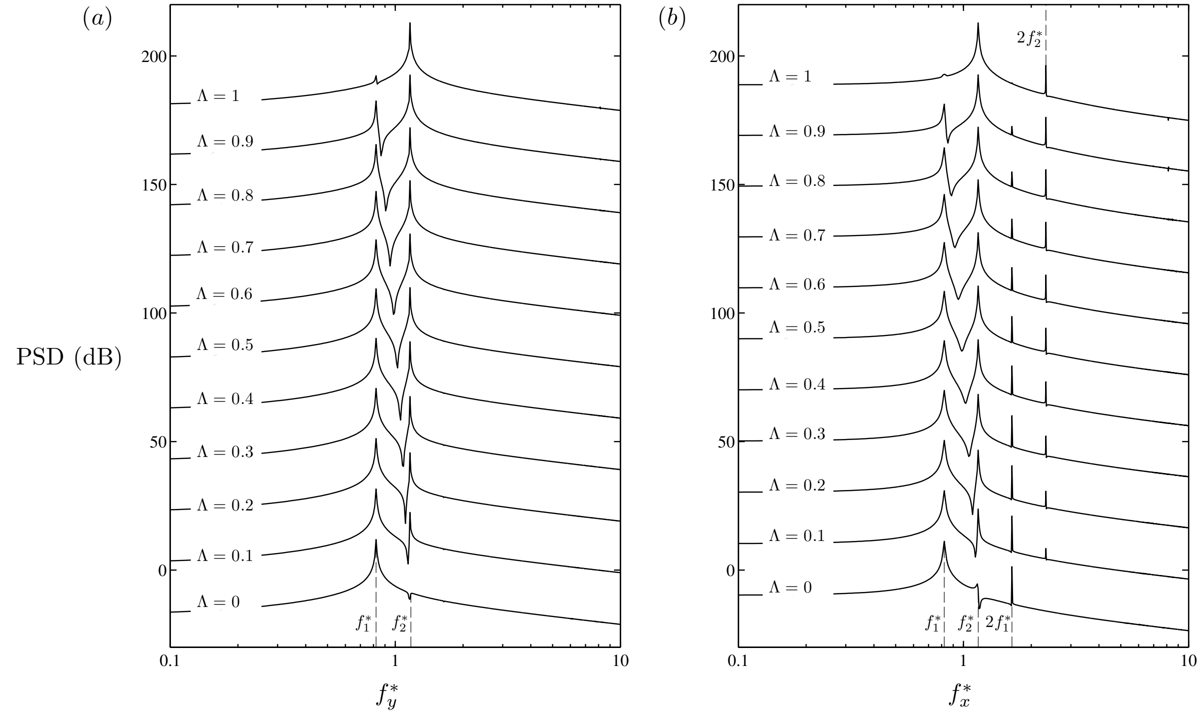

Figure 5.29 Spectra of (a) transverse and (b) streamwise vibrations obtained from Eqs. 5.19-5.22 for $\zeta_{TMD} = 0$.

6 Conclusions

Experimental studies were performed to investigate vortex-induced vibrations of a pivoted two DOF circular cylinder and to assess the effectiveness of an adaptive TMD in controlling these vibrations. A novel experimental setup was designed to reproduce orbiting response observed in some engineering applications. Vortex-induced vibrations of the model were investigated using vibration measurements and flow visualizations. For the control of vortex-induced vibrations, an adaptive pendulum tuned-mass damper was designed and integrated with the cylindrical structure.

6.1 Vortex-induced vibrations of a two DOF pivoted circular cylinder

Experiments were performed at a constant Reynolds number of 2100 for $3.4 \leq U^* \leq 11.3$ and $0.004 \leq \zeta \leq 0.011$. The results show that relatively high amplitudes of transverse vibrations ($A_y^* \approx 1$) occur in the synchronization region situated within $5 \lesssim U^* \lesssim 8.2$. In contrast, the streamwise amplitudes of vibrations were measured to be relatively low in the synchronization region ($A_x^* < 0.2$). In agreement with previous studies, the damping ratio was shown to have a significant effect on the amplitudes of vibrations.

The results show that, in the synchronization region, the frequencies of transverse and streamwise vibrations lock onto the natural frequency of the structure ($f_x = f_y = f_n$). In the non-synchronized region, the frequencies of transverse and streamwise vibrations match the natural frequency of the structure and the vortex shedding frequency of a stationary circular cylinder. Due to the frequency of transverse vibrations matching the frequency of streamwise vibrations, the cylinder traces elliptic trajectories. Since in previous laboratory studies figure-8 type trajectories were observed, with $f_x = 2f_y$, a mathematical model was introduced to analyze the mechanism responsible for the occurrence of either figure-8, or the elliptic trajectories. The model shows that, for rigid pivoted cylinders undergoing VIV in the synchronization region, the streamwise vibrations involve oscillations at the natural frequency and its first harmonic; whereas, the transverse vibrations lock onto the natural frequency. Thus, the figure-8 or elliptic trajectories can occur and their occurrence is shown to be governed primarily by structural coupling. In particular, for weak structural coupling, figure-8 type trajectories ($f_x = 2f_y$) are observed; whereas, for stronger structural coupling, elliptic trajectories occur ($f_x = f_y$).

Four distinct types of elliptic trajectories were observed experimentally in the synchronization region. The four types of trajectories are shown to be associated with four distinct ranges of phase angles between the streamwise and transverse vibrations, which define the orientation of the trajectory and the direction of orbiting. Although varying the reduced velocity and damping ratio can affect the phase angle, the four types of elliptic trajectories are governed primarily by structural coupling. Each of the four identified types of trajectories is shown to correspond to a specific range of U_c^* .

Flow visualization was performed in the wake of the cylinder at a single reduced velocity in the synchronization region and for two different sets of ζ and U_c^*. For each set of parameters, flow visualization was performed at two different elevations along the cylinder span (z/L = 0.65 and 0.84). The results show that a double roll up of shear layers occurs in the formation region. However, the downstream development of the wake vortices is found to depend on the elevation at which the flow visualization was performed and the values of ζ and U_c^*. For the higher elevation (z/L = 0.65), the results show that, depending on ζ and U_c^*, two different vortex shedding patterns occur: (i) a 2P vortex shedding pattern, with counter-clock-wise vortices merging in the near wake (ii) a 2P vortex shedding pattern without merging of the vortices in the near wake. For the lower elevation (z/L = 0.65) and for both sets of ζ and U_c^* investigated, the counter-clock-wise and clock-wise vortices merge in the wake of the cylinder and form a 2S-like vortex shedding pattern.

6.2 Control of vortex-induced vibrations of a two DOF pivoted circular cylinder using a two DOF tuned-mass damper

Experimental studies were performed to assess the effectiveness of an adaptive TMD in mitigating vortex-induced vibrations of a two DOF pivoted circular cylinder. Throughout the experiments, the Reynolds number, moment of inertia ratio, mass ratio, aspect ratio, Froude number, and TMD mass ratio were kept constant. The experiments were performed for two TMD damping ratios (ζ_{TMD} = 0.24 and 0). Changing the length of the pendulum, the TMD natural frequency was varied, allowing to investigate the range of tuning frequency ratio ($1/f_r^*$) from 0 to 1.59.

The results show that tuning the TMD natural frequency to the natural frequency of the structure reduces significantly the amplitudes of vibrations. Specifically, the amplitudes of transverse vibrations were decreased by a factor of ten and the streamwise amplitudes of vibrations were decreased by a factor of three. The results suggest that, for the relatively high TMD damping ratio tested (ζ_{TMD} = 0.24), changing the tuning frequency ratio within $0.7 < 1/f_r^* < 1.1$ does not change appreciably the transverse and streamwise amplitudes of vibrations. However, for ζ_{TMD} = 0, increasing the tuning frequency ratio from 1 to 1.1 (10 % increase) increases the transverse amplitudes of vibrations by a factor of five and the streamwise amplitudes of vibrations by 50 %. The results show that modulations occur in the amplitudes of vibrations for both TMD damping ratios tested. For ζ_{TMD} = 0.24, the modulations are more pronounced when the natural frequency of the pendulum is set by incrementally decreasing $1/f_r^*$. However, for ζ_{TMD} = 0, the modulations are more pronounced when the natural frequency of the pendulum is set via incremental increases.

The results show that the TMD damping ratio (ζ_{TMD}) significantly affects the frequency response of the structure. For ζ_{TMD} = 0.24, the frequency of transverse vibrations is independent of tuning frequency ratio ($1/f_r^*$) and is characterized by the natural frequency and harmonics of the natural frequency. However, for $\zeta_{TMD} = 0$, the frequency of the transverse vibrations depends significantly on the tuning frequency ratio. Specifically, for $1/f_r^* < 0.5$, the spectra of transverse vibrations feature peaks at the natural frequency (f_n) and harmonics of the natural frequency ($2f_n$, $3f_n$, etc.); whereas, for $0.5 < 1/f_r^* \leq 1.1$, the spectra of transverse vibrations are characterized by two frequencies, f_1 and f_2, with f_1 being lower than f_n and f_2 higher than f_n.

Analysis of the frequency of streamwise vibrations showed that, in the synchronization region, the dominant frequencies of streamwise vibrations match those of transverse vibrations. As a result, the cylinder traces elliptic type trajectories. The results show that the tuning frequency ratio significantly affects the elliptic trajectories. Specifically, tuning the TMD to $1/f_r^* \approx 1$ scales down the elliptic trajectory to a point, with insignificant vibrations observed close to $1/f_r^* = 1$. Analysis of the phase angle between the streamwise and transverse vibrations of the structure showed that θ depends significantly on the tuning frequency ratio. The results show that for $1/f_r^* < 1$, the phase angle is nearly constant. However, at the tuned condition ($1/f_r^* = 1$), the phase fluctuates with time significantly. This was speculated to be attributed to the very low streamwise and transverse amplitudes of vibrations of the structure at the tuned condition.

A mathematical model was proposed to gain insight into the forcing frequency and frequency of response for the two TMD damping ratios tested in the experiments. For the higher TMD damping ratio ($\zeta_{TMD} = 0.24$), the modeling results suggest that, in the synchronization region, the frequency of fluid forcing in the streamwise direction is twice that of the transverse direction and twice the natural frequency of the structure ($f_{e,x} = 2f_{e,y} = 2f_n$). For the lower TMD damping ratio ($\zeta_{TMD} = 0$) and for $1/f_r^* < 0.5$, the modeling suggests that the same conclusion applies. However, for $1/f_r^* > 0.5$, the model suggests that, in the synchronization region, the frequency of fluid forcing in the transverse direction is linked to the fundamental frequencies of the structure (i.e., f_1 and f_2), and the frequency of fluid forcing in the streamwise direction is characterized by the first harmonics of the fundamental frequencies ($2f_1$, and $2f_2$). The modeling results imply that, independent of the value of the TMD damping ratio and tuning frequency ratio, the frequency of transverse vibrations is characterized by the fundamental frequency or frequencies of the structure. The frequency of streamwise vibrations is characterized by the fundamental frequency or frequencies of the structure as well as the first harmonic of the fundamental frequency or frequencies of the structure.

7 Recommendations

A mathematical model was proposed to predict the frequency response of a two DOF circular cylinder with a structural coupling between streamwise and transverse vibrations. The model was shown to be capable of predicting the frequency response of the structure. However, it does not provide sufficient insight into the amplitude response of the structure. This is speculated to be linked to the simplifying assumptions made for the forcing functions utilized in the model. Previous analytical investigations, e.g., Hartlen & Currie (1970), show that a lift oscillator model can properly predict amplitude and frequency response of one DOF structure. It is speculated that by implementing a similar model for the forcing functions, further insight can be gained into the amplitude response of VIV of a two DOF cylindrical structures with coupling characteristic.

The flow visualization experiments were performed at a single reduced velocity. Further investigations should be performed to identify different vortex shedding patterns for a range of reduced velocities. Moreover, it was shown that not all of the vortex shedding patterns observed in the present study match the map developed for one DOF cylindrical structures. Thus, it is recommended that the map be upgraded to a multidimensional map that accounts for the effect of the second degree of freedom.

The experiments, performed to investigate the effectiveness of the TMD for the mitigation of VIV were conducted for a single TMD mass ratio and for two different TMD damping ratios. Further investigations should be performed to study the effect of TMD mass ratio and damping ratio on the TMD performance.

In the present study, vibrations of the pendulum were not measured. Since the amplitude of vibrations of the pendulum is of significance in practical applications, further investigations should be performed to study the effect of the governing parameters, e.g., TMD mass and damping ratios, on the vibrations of the pendulum.

References

Assi, G.R.S. (2009) "Mechanisms for Flow-induced vibration of interfering bluff bodies," Imperial College London Ph.D. thesis.

Bearman, P.W. (1984) "Vortex shedding from oscillating bluff bodies," Annual Review of Fluid Mechanics, Vol. 16, pp. 195-222.

Berger, E., and Wille, R. (1972) "Periodic flow phenomena," Annual Review of Fluid Mechanics, Vol. 4, pp. 313-340.

Bishop, R.E.D., and Hassan, A.Y. (1963) "The lift and drag forces on a circular cylinder oscillating in a flowing fluid," Proceedings of the Royal Society A, Vol. 277, pp. 51-75.

Blevins, R.D., and Coughran, C.S. (2009) "Experimental investigation of vortex-induced vibration in one and two dimensions with variable mass, damping, and Reynolds number," ASME Journal of Fluids Engineering, Vol.131, pp. 101202-7.

Brika, D., and Laneville, A. (1993) "An experimental study of the aeolian vibrations of a flexible circular cylinder at different incidences," Journal of Fluids and Structures, Vol. 9, pp. 371-391.

Burrough, H.L. (1975) "Structural dynamics of large multi-flue chimneys," Proceedings of the International Conference on Wind Effects on Buildings and Structures, pp. 497-514.

Cerretelli, C., and Williamson, C.H.K. (2004) "The physical mechanism for vortex merging," Journal of Fluid Mechanics, Vol. 475, pp. 41-77.

Chang C.C., and Gu, M. (1999) "Suppression of vortex-excited vibration of tall buildings using tuned liquid dampers," Journal of Wind Engineering and Industrial Aerodynamics, Vol. 83, pp. 225-237.

Choi, H., Jeon, W., and Kim, J. (2008) "Control of flow over a bluff body," Annual Review of Fluid Mechanics, Vol. 40, pp. 113-139.

Dailey, J.E., Weidler, J.B., Hanna, S., Zedan, M., and Yeung, J. (1987) "Pile fatigue failures. III: motions in seas," ASCE Journal of Waterway, Port, Coastal, Ocean Engineering, Vol. 113, pp. 233-250.

Every, M.J., King, R., and Weaver, D.S. (1982) "Vortex-excited vibrations of cylinders and cables and their suppression," Journal of Ocean Engineering, Vol. 2, pp. 135-157.

Feng, C.C. (1968) "The measurement of vortex-induced effects in flow past stationary and oscillating circular and D-section cylinders," University of British Columbia Master's thesis.

Fischer, F.J., Jones, W.T., and Kino, R. (1979) "Current induced oscillations of cognac piles during installation-prediction and measurement'" Proceedings of Symposium on Practical Experiences with Flow-lnduced Vibrations, Berlin, pp. 570-581.

Flemming, F., and Williamson, C.H.K. (2005) "Vortex-induced vibrations of a pivoted cylinder," Journal of Fluid Mechanics, Vol. 522, pp. 215-252.

Frahm, H. (1911) "Device for Damping Vibrations of Bodies," US Patent 989,958.

Fujarra, A.L.C., Pesce, C.P., Flemming, F., and Williamson C.H.K. (2001) "Vortex-induced vibration of a flexible cantilever," Journal of Fluids and Structures, Vol. 15, pp. 651-58.

Gamble, S., RWDI, Personal Communication, 2009.

Gerges, R.R., Vickery, B.J. (2005) "Optimum design of pendulum-type tuned mass dampers," Journal of the Structural Design of Tall and Special Buildings, Vol. 14, pp. 353-368.

Gharib, M.R. (1999) "Vortex-induced vibration, absence of lock-in, and fluid force deduction," California Institute of Technology Ph.D. thesis.

Goswami, I., Scanlan, R.H., and Jones, N.P. (1993) "Vortex-induced vibration of circular cylinders-part 2: new model," Journal of Engineering Mechanics, Vol. 119, pp. 2288-2302.

Govardhan, R., and Williamson, C.H.K. (2000) "Modes of vortex formation and frequency response for a freely-vibrating cylinder," Journal of Fluid Mechanics, Vol. 420, pp. 85-130.

Griffin, O.M., Skop, R.A., and Koopmann, G.H. (1973) “The vortex-excited resonant vibrations of circular cylinders,” Journal of Sound and Vibration Vol. 31, pp. 235-242.

Griffin, O.M., (1980) “Vortex-excited cross-flow vibrations of a single cylindrical tube,” ASME Journal of Pressure Vessel Technolology, Vol. 102, pp. 158-166.

Hartlen, R.T., and Currie, I.G., (1970), “A lift-oscillator model for vortex-induced vibrations,” Proceedings of the ASCE, Journal of Engineering Mechanics, Vol. 69, pp. 577-591.

Huera-Huarte, F.J., and Bearman, P.W. (2009) “Wake structures and vortex-induced vibrations of a long flexible cylinder- Part 1: Dynamic response,” Journal of Fluids and Structures, Vol. 25, pp. 969-990.

Huse, E., Kleiven, G., and Nielsen, F.G. (1998) “Large scale model testing of deep sea risers,” Offshore Technology Conference, OTC Number 8701, 4-7 May, Houston, TX, USA.

Ishizaki, H. (1967) “Effects of wind pressure fluctuations on structures,” International Research Seminar N.R.C. Ottawa. Vol. 2, pp. 265-277.

Jeon, D., and Gharib, M. (2001) “On circular cylinders undergoing two degrees of freedom on vortex-induced vibration and at low mass and damping,” Journal of Fluid Mechanics, Vol. 19, pp. 389-447.

Jauvtis, N., and Williamson, C.H.K. (2004) “The effect of two degrees of freedom on vortex-induced vibration at low mass and damping,” Journal of Fluid Mechanics, Vol. 509, pp. 23-62.

Kareem, A. (1983) “Mitigation of wind induced motion of tall buildings,” Journal of Wind Engineering and Industrial Aerodynamics, Vol. 11, pp. 273-284.

Kareem, A., Kijewski, T., and Tamura, Y. (1999) “Mitigation of motion of tall buildings with specific examples of recent applications,” Journal of Wind and Structures, Vol. 2, pp. 201-251.

Khalak, A., and Williamson, C.H.K. (1999) “Motions, forces and mode transitions in vortex-induced vibrations at low mass-damping,” Journal of Fluids and Structures, Vol.13, pp. 813–851.

Kim, Y., You, K., and Kim, H. (2008) “Wind-induced excitation control of tall building with tuned mass dampers,” Journal of the Structural Design of Tall and Special Buildings, Vol. 17, pp. 669-682.

Kwok, K.C.S., and Samali, B. (1995) “Performance of tuned mass dampers under wind loads,” Journal of Engineering Structures, Vol. 17, pp. 655–667.

Landl, R. (1975) “A mathematical model for vortex-excited vibrations of bluff bodies,” Journal of Sound and Vibration, Vol. 42, pp. 219-234.

Leong, C.M., and Wei, T. (2008) “Two-degree-of-freedom vortex-induced vibration of a pivoted cylinder below critical mass ratio,” Proceedings of the Royal Society A, Vol. 464, pp. 2907-2927.

Lin, J.T., and Pao, Y.H. (1979) “Wakes in stratified fluids,” Annual Review of Fluid Mechanics, Vol. 11, pp. 317-338.

Lin, C., Ueng, J., and Huang, T. (1999) “Seismic response reduction of irregular buildings using passive tuned mass dampers,” Journal of Engineering Structures, Vol. 22, pp. 513-524.

Lourenco, R., (2011) “Design, construction and testing of an adaptive pendulum tuned mass damper,” University of Waterloo Master’s thesis.

Modi, V.J., Sun, J.L.C., Shupe, L.S., and Solyomvari, A.S. (1981) “Suppression of wind-induced instabilities using nutation dampers,” Proceedings of Indian Academy of Sciences, Vol. 4, pp. 461-470.

Modi, V.J., Welt, F., and Seto, M.L. (1995) “Control of wind-induced instabilities through application of nutation dampers: a brief review” Journal of Engineering Structures, Vol. 17, pp. 626-638.

Modi, V.J., and Seto, M.L. (1997) “Suppression of flow-induced oscillations using sloshing liquid dampers: analysis and experiments,” Journal of Wind Engineering and Industrial Aerodynamics, Vol. 67 and 68, pp. 611-625.

Moffat, R.J. (1988) “Describing the Uncertainties in Experimental Results” Experimental Thermal and Fluid Science Journal, Vol. 1, pp. 3-17.

Morse, T.L., and Williamson, C.H.K. (2006) “Employing controlled vibrations to predict fluid forces on a cylinder undergoing vortex-induced vibration,” Journal of Fluids and Structures Vol. 22, pp. 877-884.

Morton, C.R. (2010) “Experimental and numerical investigations of the flow development over cylinders with stepwise discontinuities in diameter,” University of Waterloo Master’s thesis.

Norberg, C. (1994) “An experimental investigation of the flow around a circular cylinder: influence of aspect ratio,” Journal of Fluid Mechanics, Vol. 258, pp. 287-316.

Oertel, H. (1990) “Wakes behind blunt bodies,” Annual Review of Fluid Mechanics, Vol. 22, pp. 539-564.

Owen, J.C., Bearman, P.W., and Szewczyk, A.A. (2001) “Passive Control of VIV with drag reduction,” Journal of Fluids and Structures, Vol. 15, pp. 597-605.

Parkinson, G.V. (1971) “Wind-induced instability of structures,” Philosophical Transactions of the Royal Society of London A, Vol. 269, pp. 395-409.

Price, P., and Thompson, R.W. (1956) “Suppression of the flow-induced vibration of circular cylinders,” Journal of Engineering Mechanics, Division of American Society of Civil Engineers, Vol. 82 (EM3), 1030.

Provansal, M., Mathis, C., and Boyer, L. (1987) “Benard-von Karman instability: transient and forced regimes,” Journal of Fluid Mechanics, Vol. 182, pp. 1-22.

Roshko, A. (1954) “On the development of turbulent wakes from vortex streets,” NACA Rep. 1191.

Sadek, F., Mohraz, B., Taylor, A.W., and Chung R.M. (1997) “A method of estimating the parameters of tuned mass dampers for seismic applications,” Journal of Earthquake Engineering and Structural Dynamics, Vol. 26, pp. 617-635.

Sallet, D.W. (1970) “On the reduction and prevention of the fluid induced vibrations of circular cylinders of finite length,” Shock and Vibration Bulletin, Vol. 41, pp. 31-37.

Sanchis, A., Saelevik, G., and Grue, J. (2008) “Two degrees-of-freedom vortex-induced vibrations of a spring mounted rigid cylinder with low mass ratio,” Journal of Fluids and Structures, Vol. 24, pp. 907-919.

Sarpkaya, T. (1995) “Hydrodynamic damping, flow-induced oscillations, and biharmonic response,” Journal of Offshore Mechanics and Arctic Engineering, Vol. 117, pp. 232-238.

Sarpkaya, T. (2004) “A critical review of the intrinsic nature of vortex-induced vibrations,” Journal of Fluids and Structures, Vol. 19, pp. 389-447.

Schneider, F.X. (1975) “An investigation of wind excited transversal oscillations of slender structures,” Proceedings of the International Conference on Wind Effects on Buildings and Structures, pp. 381-388.

Skop, R.A., and Griffin, O.M. (1973) “A model for the vortex-excited resonant response of bluff cylinders,” Journal of Sound and Vibration, Vol. 27, pp. 225-233.

Skop, R.A., and Griffin, O.M. (1975) “On a theory for the vortex-excited oscillations of flexible cylindrical structures,” Journal of Sound and Vibration, Vol. 41, pp. 263-274.

Sun, J.Q., Jolly, M.R. , and Norris, M.A. (1995) “Passive, adaptive and active tuned vibration absorbers-a survey” Journal of Vibration and Acoustics, Vol. 117, pp. 234-242.

Tanaka, H., and Mak, C.Y. (1983) “Effect of tuned mass dampers on wind induced response of tall buildings,” Journal of Wind Engineering and Industrial Aerodynamics, Vol. 14, pp. 357-368.

Vandiver, J.K., Marcollo, H., Swithenbank, S., and Jhingran, V. (2005) “High mode number vortex-induced vibration field experiments” Offshore Technology Conference Houston TX, OTC-17383.

Vickery, B.J., and Watkins, R.D. (1964) “Flow induced vibrations of cylindrical structures,” Proceedings of First Australian Conference on Hydraulics and Fluid Mechanics, Pergamon, pp. 213-241.

Voorhees., A., Dong, P., Atsavapranee, P., Benaroya, H., and Wei, T. (2008) “Beating of a circular cylinder mounted as an inverted pendulum,” Journal of Fluid Mechanics, Vol. 610, pp. 217-247.

Wardlaw, R.L., Cooper, K.R., Ko, R.G., and Watts, J.A. (1975) Wind tunnel and analytical investigations into the aeroelastic behavior of bundled conductors,” IEEE Transactions on Power Apparatus and Systems, PAS-94, Vol. 2, pp. 642-657.

Williamson, C.H.K. (1996) "Vortex dynamics in the cylinder wake," Annual Review of Fluid Mechanics, Vol. 28, pp. 477-539.

Williamson, C.H.K., and Govardhan, R. (2004) "Vortex-induced vibrations," Annual Review of Fluid Mechanics, Vol. 36, pp. 413-455.

Williamson, C.H.K., and Roshko, A. (1988) "Vortex formation in the wake of an oscillating cylinder," Journal of Fluids and Structures, Vol. 2, pp. 355-381.

Xu, Y.L., Kwok., K.C.S., and Samali, B. (1992) "Control of wind-induced tall building vibration by tuned mass dampers," Journal of Wind Engineering and Industrial Aerodynamics, Vol. 40, pp. 1-32.

Zdravkovich, M.M. (1981) "Review and classification of various aerodynamic and hydrodynamic means for suppressing vortex shedding" Journal of Wind Engineering and Industrial Aerodynamics, Vol. 7, pp. 145-189.

Zdravkovich, M.M. (1997) "Flow around circular cylinders, Vol. 1: Fundamentals," Oxford University Press, Vol. 1.

Appendix A: Calibration of the displacement sensors

Both of the sensors used for streamwise and transverse vibration measurements were calibrated using a high precision milling machine with a displacement resolution of one micron. Figures A.1a and b show the sensors output voltage with the cylinder location for the sensors used to measure the streamwise and transverse vibrations, respectively. The least square method was used to fit a straight line to the voltage output of the sensors. The linearities of the sensors used for streamwise and transverse vibrations were obtained to be 139 and 108 microns, corresponding to ± 0.005 and ± 0.004 cylinder diameters, respectively.

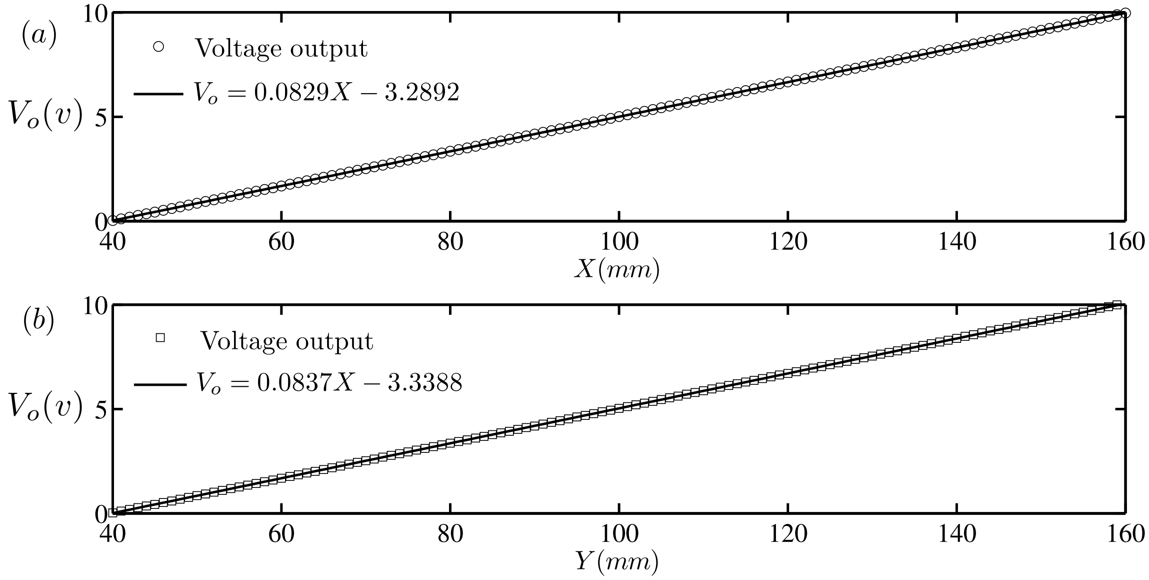

Figure A.1 Sensors calibration coefficients.

Appendix B: Uncertainty analysis

The uncertainty analysis is grouped into the following three subsections**:**

- (i) Amplitudes of vibrations
- (ii) Frequencies of vibrations
- (iii) Governing parameters

Amplitudes of vibrations

Estimates of the uncertainties associated with amplitudes of both streamwise and transverse vibrations are obtained using a method outlined by Moffat (1988). Specifically, Moffat (1988) indicated that uncertainty associated with experimental measurements can be obtained from the following equation:

$$U_{0.95} = \sqrt{Bi^2 + (t_s S)^2} \tag{B.1}$$

where, $U_{0.95}$ represents the 95% confidence level associated with an experimental measurement, which indicates that the measured value is within $\pm U_{0.95}$ of the true value 95 times out of 100; Bi and S are bias and precision errors, respectively: t_s is the Student's multiplier and is equal to 1.96 for data presented in this study (Moffat, 1988). For the amplitudes of vibrations, the bias error (Bi) is a fixed error mainly associated with the calibration uncertainty. The precision error (S) is a statistical error and is estimated from the following equation:

$$S = \sigma / N \tag{B.2}$$

where, σ is the root-sum-square of the measurements and N is the number of samples (Moffat, 1988). Table B.1 presents the uncertainties associated with both streamwise and transverse amplitudes of vibrations.

Table B.1 Uncertainties of the amplitudes of streamwise and transverse vibrations.

Quantity	**Bi**	**S**	$\mathbf{U_{0.95} = \sqrt{Bi^2 + (1.96S)^2}}$
A_x^*	0.5%	0.9%	1.9%
A_y^*	0.4%	0.7%	1.5%

Frequencies of vibrations

Uncertainties associated with the frequencies of streamwise and transverse vibrations of the structure are attributed primarily to the frequency resolution of the power spectra from which they were obtained. Here, the bias error is:

$$\mathrm{Bi} = \mathrm{F_s}/\mathrm{n} \tag{B.3}$$

where, F_s is the sampling frequency and n is the number of data points utilized in the FFT technique. The estimates of uncertainties are given in Table B2.

Table B.2 Uncertainties of the frequencies of streamwise and transverse vibrations.

Quantity	**Bi**	**S**	$\mathbf{U_{0.95} = \sqrt{Bi^2 + (1.96S)^2}}$
f_x^*	0.5%	1%	2.1%
f_y^*	0.5%	1%	2.1%

Governing parameters

Uncertainties associated with the governing parameters are presented in Table B.3. Estimates of these uncertainties were obtained using the following equation:

$$\delta R = \sqrt{\sum_{i=1}^{N} (\frac{\partial R}{\partial X_i} \delta X_i)^2} \tag{B.4}$$

where, δR is the uncertainty associated with the governing parameter, R, and δX_i is the uncertainty associated with the variable X_i. As an example, the uncertainty of the Reynolds number ($Re = UD/\upsilon$) is given by:

$$\delta Re = \sqrt{\left(\frac{\delta U}{U}\right)^2 + \left(\frac{\delta D}{D}\right)^2 + \left(\frac{\delta \upsilon}{\upsilon}\right)^2} \tag{B.5}$$

where, δU, δD, and $\delta \upsilon$ are the uncertainties associated with the free-stream velocity, cylinder diameter, and kinematic viscosity, respectively.

Table B.3 Uncertainties of the governing parameters.

Parameter	**Re**	$\mathbf{I^*}$	$\mathbf{m^*}$	**AR**	$\mathbf{U^*}$	$\mathbf{U_c^*}$	$\boldsymbol{\mu}$	$\mathbf{1/f_r^*}$
Uncertainty	1.75%	0.1%	0.1%	0%	2.7%	12.7%	0.1%	2.1%

Appendix C: Technical drawings

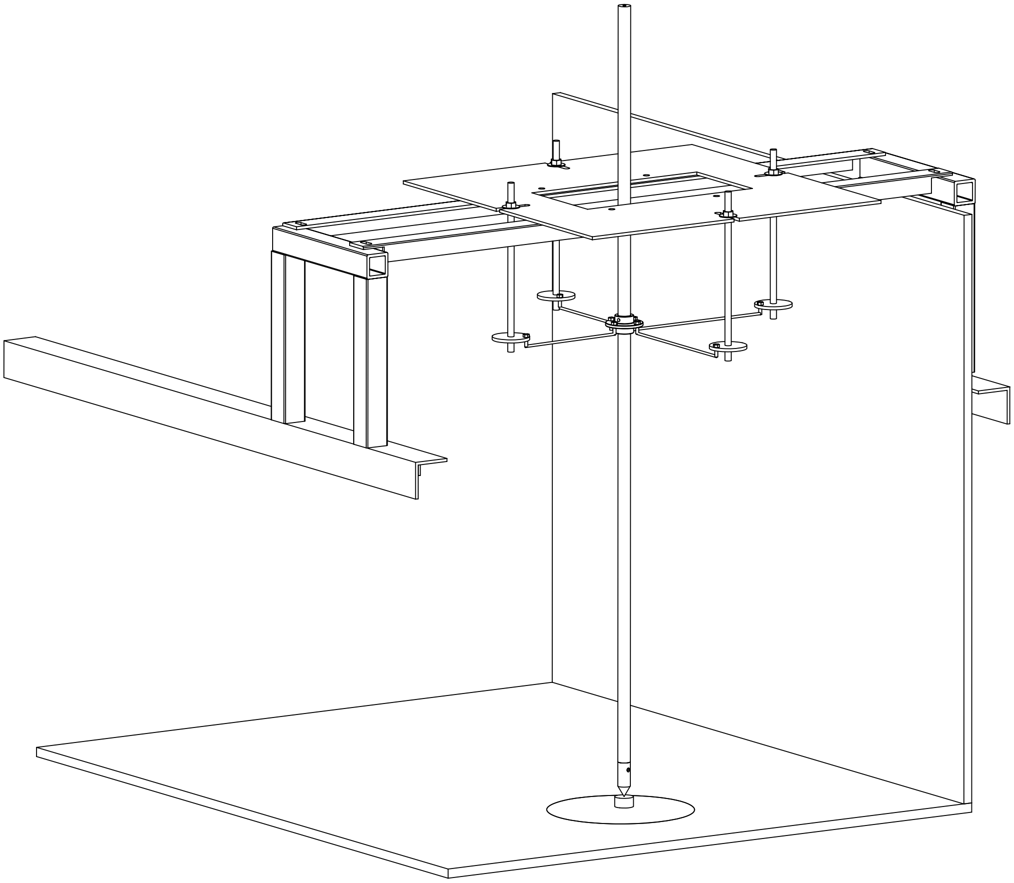

Figure C.1 Cylindrical structure.

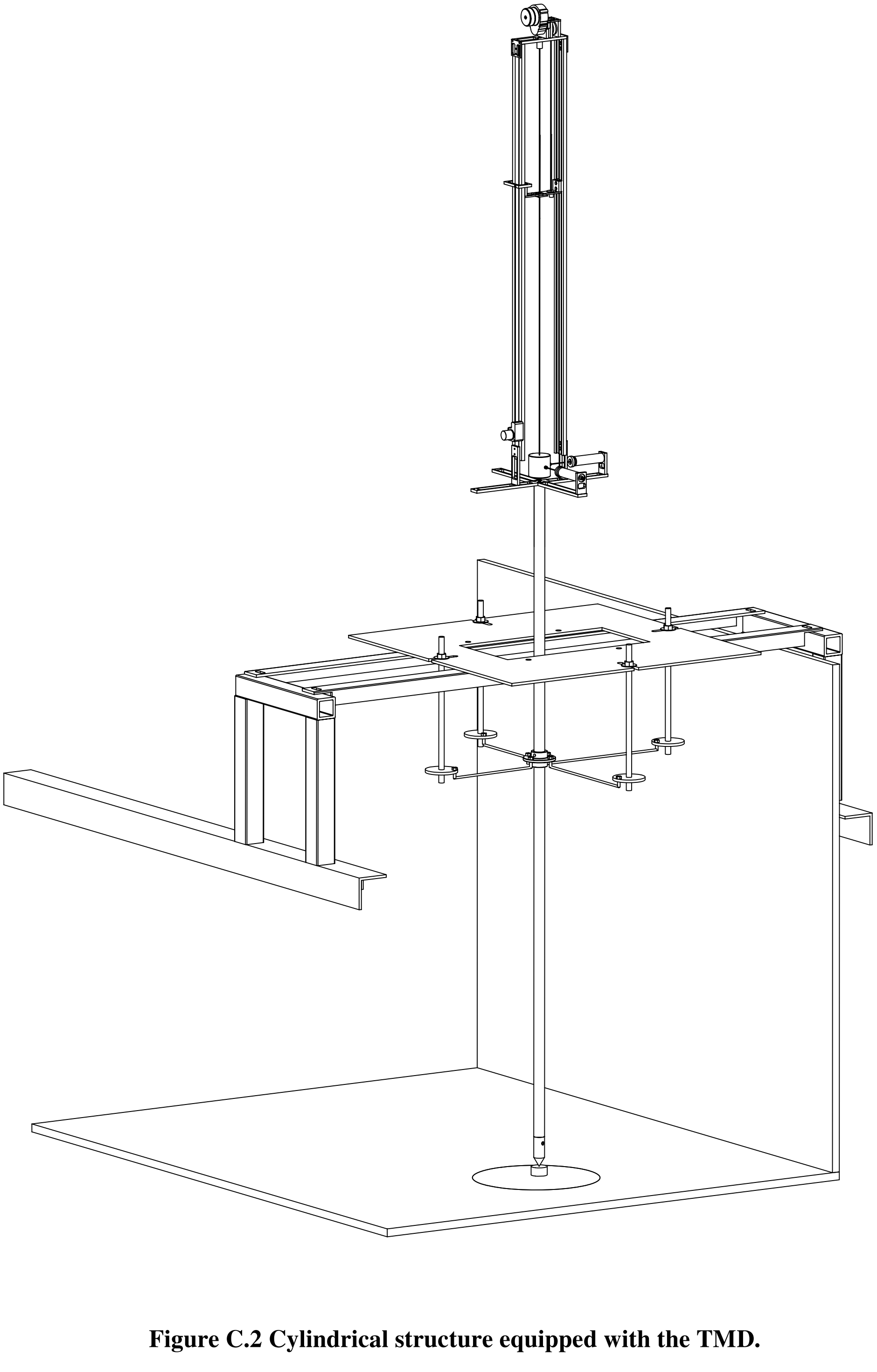

Figure C.2 Cylindrical structure equipped with the TMD.

Appendix D: Analytical solution of the free vibration equations of the structure

Free vibration equations of the structure, presented in Chapter 3, are shown in Eqs. D.1 and D.2.

$$\ddot{x}/D + 4\pi\zeta\,\dot{x}/D + 4\pi^2\,x/D + 4\pi^2(f_c/f_a)^2\,y/D = 0 \tag{D.1}$$

$$\ddot{y}/D + 4\pi\zeta\,\dot{y}/D + 4\pi^2\,y/D + 4\pi^2(f_c/f_a)^2\,x/D = 0 \tag{D.2}$$

Subtracting Eq. D.2 from Eq. D.1 and introducing $r(t) = x(t)/D - y(t)/D$, Eqs. D.1 and D.2 are reduced to Eq. D.3.

$$\ddot{r} + 4\pi\zeta\dot{r} + 4\pi^2[1-(f_c/f_a)^2]r = 0 \tag{D.3}$$

Assuming $(f_c/f_a)^2 < 1$ and $\zeta^2 << 1$, and introducing $\beta^2 = 1-(f_c/f_a)^2-\zeta^2$, the solution of Eq. D.3 can be obtained and is presented in Eq. D.4.

$$r(t) = e^{-2\pi\zeta t^*}[A\sin(2\pi\beta t^*) + B\cos(2\pi\beta t^*)] \tag{D.4}$$

Substituting $x(t)/D = y(t)/D + e^{-2\pi\zeta t^*}[A\sin(2\pi\beta t^*) + B\cos(2\pi\beta t^*)]$ in Eq. D.1, the following equation is obtained:

$$\ddot{y}/D + 4\pi\zeta\,\dot{y}/D + 4\pi^2[1+(f_c/f_a)^2]\,y/D = -4\pi^2(f_c/f_a)^2 e^{-2\pi\zeta t^*}[A\sin(2\pi\beta t^*) + B\cos(2\pi\beta t^*)] \tag{D.5}$$

Assuming that $\eta^2 = 1+(f_c/f_a)^2-\zeta^2$ and $y/D = y_h/D + y_p/D$, where y_h/D and y_p/D are the homogeneous and particular solutions of Eq. D.5, respectively, which must satisfy Eqs. D.6 and D.7.

$$\ddot{y}_h/D + 4\pi\zeta\,\dot{y}_h/D + 4\pi^2[\eta^2+\zeta^2]\,y_h/D = 0 \tag{D.6}$$

$$\ddot{y}_p/D + 4\pi\zeta\,\dot{y}_p/D + 4\pi^2[\eta^2+\zeta^2]\,y_p/D = -4\pi^2(f_c/f_a)^2 e^{-2\pi\zeta t^*}[A\sin(2\pi\beta t^*) + B\cos(2\pi\beta t^*)] \tag{D.7}$$

Solution of Eq. D.6 is presented in Eq. D.8.

$$y_h / D = e^{-2\pi\zeta t^*}[E\sin(2\pi\eta t^*) + G\cos(2\pi\eta t^*)] \tag{D.8}$$

Using the method of undetermined coefficients, the solution of Eq. D.7 was obtained as, $y_p/D = -\frac{1}{2}e^{-2\pi\zeta t^*}[A\sin(2\pi\beta t^*) + B\cos(2\pi\beta t^*)]$. Thus, $x(t)/D$ and $y(t)/D$ are given by Eq. D.9 and D.10:

$$x / D = e^{-2\pi\zeta t^*}[E\sin(2\pi\eta t^*) + G\cos(2\pi\eta t^*)] + \frac{1}{2}e^{-2\pi\zeta t^*}[A\sin(2\pi\beta t^*) + B\cos(2\pi\beta t^*)] \tag{D.9}$$

$$y / D = e^{-2\pi\zeta t^*}[E\sin(2\pi\eta t^*) + G\cos(2\pi\eta t^*)] - \frac{1}{2}e^{-2\pi\zeta t^*}[A\sin(2\pi\beta t^*) + B\cos(2\pi\beta t^*)] \tag{D.10}$$

The initial conditions are given by Eq. D.11:

$$\begin{aligned} x/D\,(t^* = 0) &= 0 \\ \dot{x}/D\,(t^* = 0) &= 0 \\ y/D\,(t^* = 0) &= y_0 / D \\ \dot{y}/D\,(t^* = 0) &= 0 \end{aligned} \tag{D.11}$$

Applying the initial conditions, it can be shown that the coefficients in Eqs. D.9 and D.10 are: $A = -(\zeta/\beta)(y_0/D)$, $B = -y_0/D$, $E = \frac{1}{2}(\zeta/\eta)(y_0/D)$, and $G = \frac{1}{2}(y_0/D)$. Considering $\zeta^2 << 1$, one can show that $A \approx 0$ and $E \approx 0$. Applying trigonometric identities, Eqs. D.9 and D.10 can be transferred to Eqs. D.12 and D.13.

$$x/D = -(y_0/D)e^{-2\pi\zeta t^*}\left\{\sin\left(\pi(\eta - \beta)t^*\right)\sin\left(\pi(\eta + \beta)t^*\right)\right\} \tag{D.12}$$

$$y/D = (y_0/D)e^{-2\pi\zeta t^*}\left\{\cos\left(\pi(\eta - \beta)t^*\right)\cos\left(\pi(\eta + \beta)t^*\right)\right\} \tag{D.13}$$

Using Maclaurin expansion, it can be shown that:

$$\beta = \sqrt{1 - (f_c/f_a)^2 - \zeta^2} \approx 1 + \frac{1}{2}[-(f_c/f_a)^2 - \zeta^2] \tag{D.14}$$

$$\eta = \sqrt{1 + (f_c/f_a)^2 - \zeta^2} \approx 1 + \frac{1}{2}[(f_c/f_a)^2 - \zeta^2] \tag{D.15}$$

Thus, $\eta - \beta \approx (f_c/f_a)^2$ and $\eta + \beta \approx 2$. Equations D.12 and D.13 were further simplified and presented in the form of Eqs. D.16 and D.17.

$$x/D = -y_0/D\, e^{-2\pi\zeta t^*} \left\{ \sin\left(\pi (f_c/f_a) t^*\right) \sin(2\pi t^*) \right\} \tag{D.16}$$

$$y/D = y_0/D\ e^{-2\pi\zeta t^*} \left\{ \cos\left(\pi (f_c/f_a) t^*\right) \cos(2\pi t^*) \right\} \tag{D.17}$$

Appendix E: Analytical solution of equations of VIV of the two DOF pivoted circular cylinder

The governing equations of vortex-induced vibrations of the structure, discussed in Chapter 4, are presented in Eqs. E.1 and E.2.

$$x''/D + 4\pi\zeta f_r\, x'/D + 4\pi^2\, x/D + 4\pi^2 U_r\, y/D = a^*\sin(4\pi t^{**} + \psi) \tag{E.1}$$

$$y''/D + 4\pi\zeta f_r\, y'/D + 4\pi^2\, y/D + 4\pi^2 U_r\, x/D = b^*\sin(2\pi t^{**}) \tag{E.2}$$

Where, $f_r = \left(\frac{f_a}{f_n}\right)\left(\frac{I^*}{I^* + C_A}\right)$, $U_r = \left(\frac{U^*}{U_c^*}\right)^2\left(\frac{I^*}{I^* + C_A}\right)$, $a^* = \frac{2}{\pi} C_D \frac{L}{L_0}\frac{U^{*2}}{(I^* + C_A)}$, and $b^* = \frac{2}{\pi} C_L \frac{L}{L_0}\frac{U^{*2}}{(I^* + C_A)}$. Subtracting Eq. E.2 from Eq. E.1 and introducing $r(t^{**}) = x(t^{**})/D - y(t^{**})/D$, Eqs. E.1 and E.2 are transferred to Eq. E.3.

$$\ddot{r} + 4\pi\zeta f_r \dot{r} + 4\pi^2(1 - U_r)r = a^*\sin(4\pi t^{**} + \psi) - b^*\sin(2\pi t^{**}) \tag{E.3}$$

Assuming that $r(t^{**}) = r_h(t^{**}) + r_p(t^{**})$, where $r_h(t^{**})$ and $r_p(t^{**})$ are the homogeneous and particular solutions of Eq. E.3, the equation can be transferred to the form of Eqs. E.4 and E.5.

$$\ddot{r}_h + 4\pi\zeta f_r \dot{r}_h + 4\pi^2(1 - U_r)r_h = 0 \tag{E.4}$$

$$\ddot{r}_p + 4\pi\zeta f_r \dot{r}_p + 4\pi^2(1 - U_r)r_p = a^*\sin(4\pi t^{**} + \psi) - b^*\sin(2\pi t^{**}) \tag{E.5}$$

Assuming $U_r < 1$ and $\zeta^2 f_r^2 << 1$, one can introduce $\beta_r = 1 - U_r - \zeta^2 f_r^2$. The solution of Eq. E.4 is obtained and presented in Eq. E.6.

$$r_h(t^{**}) = e^{-2\pi\zeta f_r t^*}[H\sin(2\pi\beta_r t^{**}) + J\cos(2\pi\beta_r t^{**})] \tag{E.6}$$

The homogeneous solution, $r_h(t^{**})$, vanishes in time and therefore the steady state solution of Eq. E.3 is equal to the particular solution, i.e., $r_{ss}(t^{**}) = r_p(t^{**})$. Using the method of undetermined coefficients, the solution of Eq. E.5 can be introduced as: $r_p(t^{**}) = \sigma_1 \sin(4\pi t^{**}) + \sigma_2 \cos(4\pi t^{**}) + \sigma_3 \sin(2\pi t^{**}) + \sigma_4 \cos(2\pi t^{**})$. Substituting $r_p(t^{**})$ in Eq. E.5, the following system of algebraic equations is obtained for σ_1, σ_2, σ_3, and σ_4.

$$\begin{aligned}
&(-U_r - 3)\sigma_1 - 4\zeta f_r \sigma_2 = \frac{a^*}{4\pi^2}\cos(\psi) \\
&4\zeta f_r \sigma_1 + (-U_r - 3)\sigma_2 = \frac{a^*}{4\pi^2}\sin(\psi) \\
&U_r \sigma_3 + 2\zeta f_r \sigma_4 = \frac{b^*}{4\pi^2} \\
&2\zeta (f_a/f_n)\sigma_3 - \left(U^*/U_c^*\right)^2 \sigma_4 = 0
\end{aligned} \tag{E.7}$$

Introducing,

$$B = \frac{b^*}{4\pi^2[4\zeta^2 (f_a/f_n)^2 + \left(U^*/U_c^*\right)^4]} \tag{E.8}$$

$$r_1 = \frac{(-U_r - 3)\cos(\psi) + 4\zeta f_r \sin(\psi)}{16\zeta^2 f_r^2 + (U_r + 3)^2}\left(\frac{a^*}{4\pi^2}\right) \tag{E.9}$$

$$r_2 = \frac{(-U_r - 3)\sin(\psi) - 4\zeta f_r \cos(\psi)}{16\zeta^2 f_r^2 + (U_r + 3)^2}\left(\frac{a^*}{4\pi^2}\right) \tag{E.10}$$

solution of Eqs. E.7 was obtained and $r_{ss}(t^{**})$ is presented in Eq. E.11.

$$r_{ss}(t^{**}) = r_1 \sin(4\pi t^{**}) + r_2 \cos(4\pi t^{**}) + B[\left(U^*/U_c^*\right)^2 \sin(2\pi t^{**}) + 2\zeta (f_a/f_n)\cos(2\pi t^{**})] \tag{E.11}$$

Substituting $x_{ss}(t^{**})/D = y_{ss}(t^{**})/D + r_{ss}(t^{**})$ in Eq. E.1, it can be shown that $y_{ss}(t^{**})/D$ is obtainable from Eq. E.12.

$$y''_{ss}/D + 4\pi\zeta f_r\, y'_{ss}/D + 4\pi^2(1+U_r)\, y_{ss}/D = b^* \sin(2\pi t^{**}) - 4\pi^2 U_r r_{ss}(t^{**}) \qquad \text{(E.12)}$$

Using the method of undetermined coefficients, the solution of Eq. E.12 can be introduced as: $y_{ss}(t^{**})/D = \kappa_1 \sin(4\pi t^{**}) + \kappa_2 \cos(4\pi t^{**}) + \kappa_3 \sin(2\pi t^{**}) + \kappa_4 \cos(2\pi t^{**})$. Substituting $y_{ss}(t^{**})/D$ and $r_{ss}(t^{**})$ in Eq. E.5, the following system of algebraic equations is obtained for κ_1, κ_2, κ_3, and κ_4.

$$\begin{aligned}
&(U_r - 3)\kappa_1 - 4\zeta f_r \kappa_2 = -U_r \sigma_1 \\
&4\zeta f_r \kappa_1 + (U_r - 3)\kappa_2 = -U_r \sigma_2 \\
&\left(U^*/U_c^*\right)^2 \kappa_3 - 2\zeta(f_a/f_n)\kappa_4 = \frac{b^*}{4\pi^2}\left(\frac{I^* + C_A}{I^*}\right) - \sigma_3\left(U^*/U_c^*\right)^2 \\
&2\zeta(f_a/f_n)\kappa_3 + \left(U^*/U_c^*\right)^2 \kappa_4 = -\sigma_4\left(U^*/U_c^*\right)^2
\end{aligned} \qquad \text{(E.13)}$$

Introducing,

$$A = \frac{a^* U_r}{4\pi^2[16\zeta^2 f_r^2 + (U_r - 3)^2][16\zeta^2 f_r^2 + (U_r + 3)^2]} \qquad \text{(E.14)}$$

$$a_1 = \left(U_r^2 - 9 + 16\zeta^2 f_r^2\right)\cos(\psi) + 24\zeta f_r \sin(\psi) \qquad \text{(E.15)}$$

$$a_2 = -24\zeta f_r \cos(\psi) + \left(U_r^2 - 9 + 16\zeta^2 f_r^2\right)\sin\psi \qquad \text{(E.16)}$$

the solution of Eqs. E.13 is obtained and $y_{ss}(t^{**})/D$ is presented in Eq. E.17.

$$y_{ss}(t^{**})/D = A[a_1 \sin(4\pi t^{**}) + a_2 \cos(4\pi t^{**})] - B\left(2\zeta\, f_a/f_n\right)\cos(2\pi t^{**}) \qquad \text{(E.17)}$$

Introducing,

$$a_3 = [4\zeta f_r(6U_r + 16\zeta^2 f_r^2 + (U_r - 3)^2]\sin(\psi) + 3[U_r^2 - 9 - 16\zeta^2 f_r^2]\cos(\psi) \qquad \text{(E.18)}$$

$$a_4 = 3[U_r^2 - 9 - 16\zeta^2 f_r^2]\sin(\psi) - [4\zeta f_r(6U_r + 16\zeta^2 f_r^2 + (U_r - 3)^2]\cos(\psi) \qquad \text{(E.19)}$$

$x_{ss}(t^{**})/D = y_{ss}(t^{**})/D + r_{ss}(t^{**})$, was also obtained and presented in Eq. E.20.

$$x_{ss}(t^{**})/D = \frac{A}{U_r}[a_3 \sin(4\pi t^{**}) + a_4 \cos(4\pi t^{**})] + B\left(U^*/U_c^*\right)^2 \sin(2\pi t^{**}) \qquad \text{(E.20)}$$

Having obtained the steady state response of the structure, R_x and R_y were obtained and presented in Eqs. E.21 and E.22, respectively.

$$R_x = \frac{B}{A}\frac{(U^*/U_c^*)^2}{\sqrt{a_3^2 + a_4^2}} = \left\{\frac{C_L}{C_D}\frac{(16\zeta^2 f_r^2 + (U_r - 3)^2)(16\zeta^2 f_r^2 + (U_r + 3)^2)}{4\zeta^2\left(f_a/f_n\right)^2 + \left(U^*/U_c^*\right)^4}\right\}\frac{\left(\dfrac{I^* + C_A}{I^*}\right)}{\sqrt{a_3^2 + a_4^2}} U_r \qquad \text{(E.21)}$$

$$R_y = \frac{B}{A}\frac{2\zeta(f_a/f_n)}{\sqrt{a_1^2 + a_2^2}} = \left\{\frac{C_L}{C_D}\frac{(16\zeta^2 f_r^2 + (U_r - 3)^2)(16\zeta^2 f_r^2 + (U_r + 3)^2)}{4\zeta^2\left(f_a/f_n\right)^2 + \left(U^*/U_c^*\right)^4}\right\}\frac{2\zeta\dfrac{f_a}{f_n}}{\sqrt{a_1^2 + a_2^2}}\frac{1}{U_r} \qquad \text{(E.22)}$$

Appendix F: Vortex-induced vibrations of a cylinder with weak coupling between streamwise and transverse vibrations

Vortex-induced vibrations of a circular cylinder mounted as a pendulum were investigated. The structure was designed in order to provide weak coupling between the streamwise and transverse vibrations. Free vibration tests were performed to obtain the structural characteristics of the cylinder. The values of the governing parameters are provided in Table F.1.

Table F.1 Governing non-dimensional parameters.

Parameter	**Value**
Re	2100
I^*	10
m^*	2.5
AR	63
U^*	8.81
ζ	0.022
U_c^*	285.5

Figures F.1a and b show the spectra of streamwise and transverse vibrations, respectively. The results indicate that the dominant frequency of streamwise vibrations is the first harmonic of the natural frequency (i.e., $f_x = 2f_n$) and the dominant frequency of transverse vibrations is the natural frequency of the structure (i.e., $f_y = f_n$). This is in agreement with the results presented in Flemming & Williamson (2005) and Leong & Wei (2008) for VIV of a pivoted circular cylinder.

Figure F.2a shows the cylinder tip trajectory for one hundred cycles of oscillations. Figure F.2b shows phase average of the trajectories presented in Fig. F.2a. The results indicate that

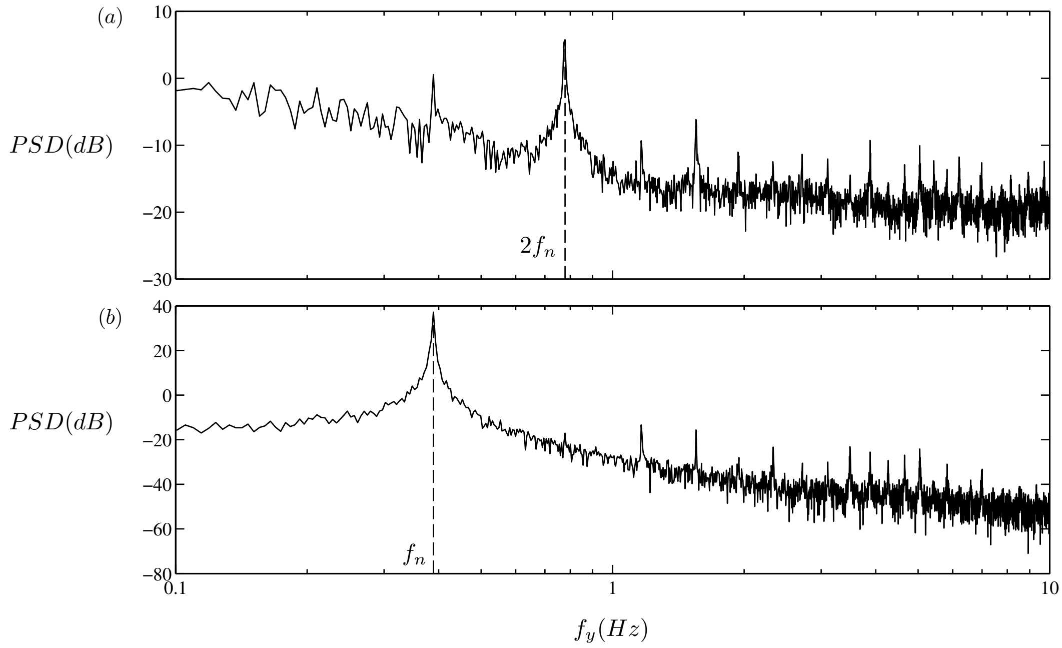

Figure F.1 (a) spectrum of streamwise vibrations and (b) spectrum of transverse vibrations.

the cylinder traces figure-8 type trajectories similar to the results presented in Flemming & Williamson (2005) and Leong & Wei (2008).

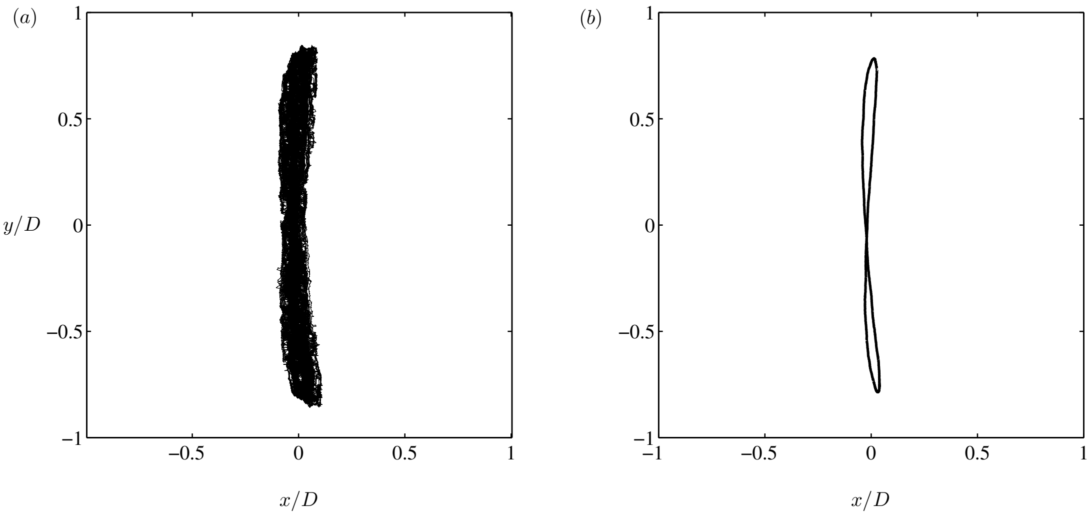

Figure F.2 (a) cylinder tip trajectories for one hundred cycles of oscillations and (b) phase averaged trajectory for one hundred cycles of oscillations.

Using an analytical model similar to the model introduced in Chapter 4, it can be shown that the occurrence of the figure-8 type trajectory is linked to weak coupling between the streamwise and transverse vibrations of the structure. Equations of motion of the cylinder are as following:

$$I\frac{d^2}{dt^2}(x/L)+Cb^2\frac{d}{dt}(x/L)+(mg\,L/2-m_d g\,L_0/2)(x/L)+K_c b^2(y/L)=M_x(t) \qquad \text{(F.1)}$$

$$I\frac{d^2}{dt^2}(y/L)+Cb^2\frac{d}{dt}(y/L)+(mg\,L/2-m_d g\,L_0/2)(y/L)+K_c b^2(x/L)=M_y(t) \qquad \text{(F.2)}$$

Introducing $f_n=\frac{1}{2\pi}\sqrt{(mgL/2-m_d gL_0/2)/(I+I_A)}$, $f_r=(\frac{f_a}{f_n})(\frac{I^*}{I^*+C_A})$, and $U_r=(\frac{U^*}{U_c^*})^2(\frac{I^*}{I^*+C_A})$, Eqs. F.1 and F.2 can be cast in the form of Eqs. F.3 and F.4:

$$x''/D+4\pi\zeta f_r\,x'/D+4\pi^2\,x/D+4\pi^2 U_r\,y/D=\frac{2}{\pi}C_D\frac{L}{L_0}\frac{U^{*2}}{(I^*+C_A)}\sin(4\pi t^{**}+\psi) \qquad \text{(F.3)}$$

$$y''/D+4\pi\zeta f_r\,y'/D+4\pi^2\,y/D+4\pi^2 U_r\,x/D=\frac{2}{\pi}C_L\frac{L}{L_0}\frac{U^{*2}}{(I^*+C_A)}\sin(2\pi t^{**}) \qquad \text{(F.4)}$$

where $()'$ denotes the differentiation with respect to t^{**} ($t^{**}=tf_n$). Note that Eqs. F.3 and F.4 are the same as Eqs. 4.3 and 4.4, previously obtained in Chapter 4. It was shown that the solution Eqs. 4.3 and 4.4, for $f_c/f_n<1$ and $\zeta^2<<1$, involves the natural frequency of the structure (f_n) and its first harmonic ($2f_n$). To determine the dominant frequency in each direction, the ratio of the amplitude associated with f_n and that associated with $2f_n$ was evaluated for the streamwise and transverse vibrations. These ratios, R_x and R_y, were analytically obtained and shown to depend on U^*, U_c^*, ζ, C_L/C_D, f_a/f_n, and I^*. Figure F.3 shows the variation of R_x with U_c^* and ζ for the experimental conditions investigated. Two distinct regions can be identified in the figure: (i) a region corresponding to $R_x>1$ and (ii) a region corresponding to $R_x<1$. The region corresponding to $R_x>1$ represents structures with relatively strong coupling characteristic. As discussed in Chapter 4, these structures are expected to trace elliptic type trajectories. The region corresponding to $R_x < 1$ represents structures with weak coupling characteristic, which should trace figure-8 type trajectories. The data point corresponding to the results presented in Figs. F.1 and F.2 is shown in Fig. F.3 (by the square symbol). The figure indicates that the value of R_x corresponding to the data point shown in the figure is lower than unity. Thus, the experimental results confirm that structures with weak coupling should trace figure-8 type trajectories (Fig F.2) and as a result the cylinder should trace figure-8 type trajectories.

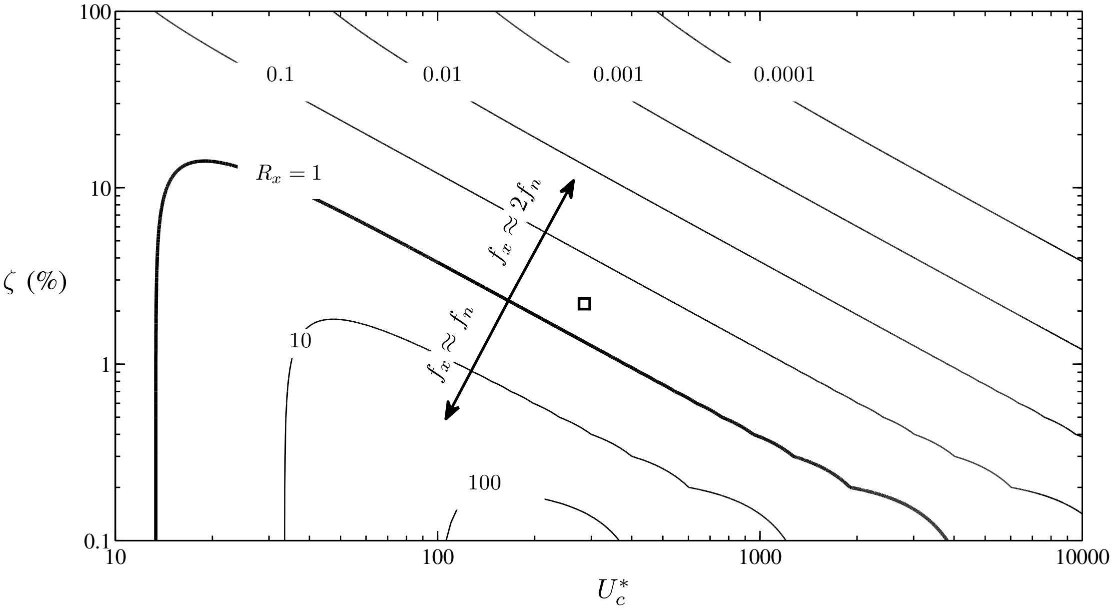

Figure F.3 R_x contours, for $U^* = 8.8$, $C_L/C_D = 0.25$, $f_a/f_n = 1$, and $I^* = 10$. The symbol (□) corresponds to the experimental condition.